

Frank Freikamp

**Towards Multi-Cycle Simulation
of In-Cylinder Flow and Combustion**



Cuvillier Verlag Göttingen
Internationaler wissenschaftlicher Fachverlag

Towards Multi-Cycle Simulation of In-Cylinder Flow and Combustion

Von der Fakultät für Maschinenwesen der
Rheinisch-Westfälischen Technischen Hochschule Aachen
zur Erlangung des akademischen Grades eines Doktors der
Ingenieurwissenschaften genehmigte Dissertation

vorgelegt von

Frank Freikamp

aus

Dinslaken

Berichter: Univ.-Prof. Dr.-Ing. Dr. h.c. Dr.-Ing. E.h. N. Peters
Univ.-Prof. Dr.-Ing. W. Schröder

Tag der mündlichen Prüfung: 21. November 2008

Bibliografische Information der Deutschen Nationalbibliothek

Die Deutsche Nationalbibliothek verzeichnet diese Publikation in der Deutschen Nationalbibliografie; detaillierte bibliografische Daten sind im Internet über <http://dnb.ddb.de> abrufbar.

1. Aufl. - Göttingen : Cuvillier, 2008

Zugl.: D 82 (Diss. RWTH Aachen University, 2008)

978-3-86727-817-1

© CUVILLIER VERLAG, Göttingen 2008

Nonnenstieg 8, 37075 Göttingen

Telefon: 0551-54724-0

Telefax: 0551-54724-21

www.cuvillier.de

Alle Rechte vorbehalten. Ohne ausdrückliche Genehmigung des Verlages ist es nicht gestattet, das Buch oder Teile daraus auf fotomechanischem Weg (Fotokopie, Mikrokopie) zu vervielfältigen.

1. Auflage, 2008

Gedruckt auf säurefreiem Papier

978-3-86727-817-1

Vorwort

Die vorliegende Arbeit entstand während meiner Tätigkeit als wissenschaftlicher Mitarbeiter am Institut für Technische Mechanik an der Rheinisch-Westfälischen Technischen Hochschule Aachen.

Vor allem danke ich Herrn Professor Dr.-Ing. Dr. h. c. Dr.-Ing. E. h. N. Peters für seine Unterstützung, seine kritischen Anmerkungen, seine zahlreichen Ideen und die mir gewährte Freiheiten. Herrn Professor Dr.-Ing. W. Schröder danke ich für sein Interesse an meiner Arbeit und für die Übernahme des Koreferates und Herr Professor Dr. M. Behr für die Übernahme des Vorsitzes der Prüfungskommission.

Weiterhin möchte ich allen jetzigen und ehemaligen Mitarbeitern des Instituts für Technische Verbrennung für die kollegiale und hilfsbereite Zusammenarbeit danken, die zum Gelingen dieser Arbeit beigetragen haben. Im Besonderen gilt mein Dank Günter Paczko, Stefan Vogel, Jens Ewald, Rainer Dahms, Olaf Röhl, Lars-Uve Schrader, Dirk Linse und Andreas Fiolitakis.

Ein herzlicher Dank gilt meinen Eltern und meinem Bruder für die stete Unterstützung und Ermutigung.

Ein besonderer Dank gilt meiner Familie und vor allem meiner Frau Anja für ihre Geduld, Rückhalt und Unterstützung, auf die ich mich stets verlassen konnte.

Zusammenfassung

Zur Erfüllung zukünftiger Anforderungen hinsichtlich Kraftstoffverbrauch und Emissionen werden direkteinspritzende Ottomotoren (DISI - Direct Injection Spark Ignition) in Kombination mit Turboaufladung als vielversprechendes Motorenkonzept gesehen. Zyklische Schwankungen stellen eine entscheidende Herausforderung bei diesem Brennverfahren dar und spielen eine Schlüsselrolle bei der Optimierung der Verbrennungsprozesses.

Die Modellierung der Strömungs- und Verbrennungsvorgänge mittels numerischer Strömungssimulation in Kombination mit statistischer Turbulenzmodellierung (RANS – Reynolds Averaged Navier-Stokes) stellt ein leistungsfähiges und zuverlässiges Werkzeug in der Rahmen der Motorenentwicklung dar. Basierend auf gemittelten Größen kann dieser Ansatz per Definition instationäre Phänomene wie zyklische Schwankungen nicht beschreiben. Die Grobstruktursimulation oder Large Eddy Simulation (LES) bietet die Möglichkeit, turbulente Strukturen und zeitliche Schwankungen auflösen, und somit zyklische Schwankungen in der Simulation abzubilden. Aufgrund der hohen Anforderungen an die Numerik, Diskretisierung, Gitterauflösung und Zeitschrittgröße ist der Berechnungsaufwand und Zeitbedarf bei dieser Methodik deutlich erhöht. Die Kombination beider Modellierungsansätze führt zu hybriden RANS/LES-Modellen.

Gegenstand der Arbeit ist die Entwicklung eines hybriden Zwei-Skalen-Turbulenzmodells zur Beschreibung zyklischer Schwankungen sowie die Demonstration der Realisierbarkeit der Kopplung des Modelles an das G -Gleichungsmodell zur Beschreibung der vorgemischten Verbrennung. Im Kapitel 2 werden die Grundgleichungen turbulenter Strömungen vorgestellt. Kapitel 3 diskutiert die verschiedenen Ansätze zur Turbulenzmodellierung sowie das Zwei-Skalen-Modell. In Kapitel 4 wird ein Überblick über die Modellierung der vorgemischten Verbrennung für RANS und LES gegeben. Die Numerik des verwendeten Strömungslösers AC-FLUX wird in Kapitel 5 vorgestellt. Die entwickelten Modelle und Methoden werden in Kapitel 6 anhand von elementaren Testfällen analysiert und auf die Simulation von zwei Modellmotorkonfigurationen angewandt; abschließend wird die Kopplung des hybriden Turbulenzmodelles mit der G -Gleichung analysiert und bewertet.

Contents

| | | |
|----------|--|-----------|
| 1 | Introduction | 1 |
| 2 | Physics of fluids | 4 |
| 2.1 | Fundamental equations of fluid mechanics | 4 |
| 2.2 | Non-dimensional form | 6 |
| 3 | Description and modelling of turbulent flows | 8 |
| 3.1 | Turbulence fundamentals | 8 |
| 3.2 | Statistical modelling | 13 |
| 3.2.1 | The statistical description of turbulent flows | 14 |
| 3.2.2 | Correlations and turbulent spectra | 16 |
| 3.2.3 | Average transport equations | 19 |
| 3.3 | RANS turbulence models | 21 |
| 3.3.1 | Linear eddy-viscosity models | 22 |
| 3.3.2 | Extensions | 26 |
| 3.3.3 | Closing remarks | 28 |
| 3.4 | Large Eddy Simulation | 28 |
| 3.4.1 | Filtering | 31 |
| 3.4.2 | Filtered transport equations | 35 |
| 3.4.3 | Sub-Filter Scale Models | 37 |
| 3.5 | Hybrid modelling | 41 |
| 3.5.1 | Overview of hybrid modelling approaches | 41 |
| 3.5.2 | Two-level modelling | 43 |
| 3.5.3 | Closing remarks | 45 |
| 3.6 | Artificial turbulence | 46 |
| 3.6.1 | Fourier transform approach | 47 |
| 3.6.2 | Diffusion process | 48 |
| 3.6.3 | Synthesized turbulence | 49 |
| 4 | Premixed combustion | 52 |
| 4.1 | Laminar premixed combustion | 52 |
| 4.1.1 | Structure of premixed flames | 52 |
| 4.1.2 | The level-set approach for laminar flame propagation | 55 |
| 4.2 | Physics of turbulent flame propagation | 57 |
| 4.2.1 | Regimes in premixed combustion | 57 |
| 4.2.2 | The turbulent burning velocity | 60 |
| 4.3 | Progress variable approach | 61 |

| | | |
|----------|--|------------|
| 4.4 | The level-set approach for turbulent flames | 62 |
| 4.4.1 | Transport equations for the mean flame front position and flame brush thickness | 62 |
| 4.4.2 | Modelling closures for \tilde{G} and \tilde{G}''^2 | 63 |
| 4.4.3 | Modelling closure for the turbulent burning velocity | 65 |
| 4.5 | LES combustion modelling | 66 |
| 4.5.1 | Regime diagram for LES | 66 |
| 4.5.2 | Thickened flame model | 68 |
| 4.5.3 | Progress variable approaches | 69 |
| 4.5.4 | Level-set formulation for LES | 69 |
| 4.6 | VLES/G-equation coupling | 71 |
| 5 | Numerics | 73 |
| 5.1 | Discretisation of the conservation equations | 73 |
| 5.1.1 | Development for a single pde | 74 |
| 5.1.2 | General form of the discretised equations | 76 |
| 5.2 | Computation of the pressure field | 77 |
| 5.2.1 | Pressure/velocity coupling | 78 |
| 5.3 | Solution of the G -model equations | 78 |
| 6 | Application | 81 |
| 6.1 | Homogeneous isotropic turbulence | 81 |
| 6.1.1 | Comparison of initialisation strategies | 81 |
| 6.1.2 | Numerical studies | 87 |
| 6.2 | Square piston engine | 94 |
| 6.2.1 | Flow characterisation | 94 |
| 6.2.2 | Results | 96 |
| 6.3 | Multi-cycle engine simulations | 101 |
| 6.4 | Cylindrical disk | 106 |
| 7 | Summary and conclusion | 115 |
| | Bibliography | 117 |

1 Introduction

For the conversion of chemical energy to thermal energy to mechanical energy, combustion represents up to now the most important process with fossil fuels being the most important source of energy. The internal combustion (IC) engine has been developed in the late 19th century, and regarding fuel efficiency, economy, and emissions the device has been significantly improved since. Although many alternative concepts like electrical or hybrid power trains or fuel cells are investigated and developed, the dominant device in the near and intermediate future is expected to be the IC-engine.

Over the past decades, one of the major drivers for the improvement and optimisation of the IC engine has been the enforcement of stricter emission regulations in the US as well as in Europe and in Japan. To be able to achieve the legislative restrictions new technologies and especially new combustion concepts have been developed. On the aftertreatment side the development of catalyst systems and particle filters have significantly reduced the output of emissions. However the improvement lead to a decrease in fuel efficiency and actually does not address the cause of the emissions. For the fulfillment of future requirements concerning fuel consumption and emission standards, two combustion concepts are considered as being the most promising approach: turbo-charged diesel and stratified spark ignition (SI) engines with high pressure direct injection (DI) systems.

While DISI-engine are supposed to have a much higher potential in terms of fuel consumption economy compared to the classical homogeneous combustion concepts, combustion stability and emission are the major topics of concern. Cyclic variability represents a critical issue in DISI-engines, as cycle-to-cycle variations are substantial to the combustibility of the air/fuel mixture at the time of the discharge of the spark plug leading to partial burning or even misfire. These incomplete combustion cycles lead to a significant increase in emissions, especially unburned hydrocarbon emissions, and a significant reduction in terms of fuel efficiency, therefore rendering it highly undesirable. Thus the cycle-to-cycle variations of the gas motion have been identified as playing a key role for the further optimisation of combustion process and thus the complete device. While the impact onto the combustion process is immediately visible, the cause for the cyclic variability is not yet fully understood, although generally attributed to turbulence effects.

Computational fluid dynamics (CFD) in combination with Reynolds averaged Navier-Stokes (RANS) turbulence modeling closures has been established as a very efficient and reliable tool for the description and analysis of the flow and combustion processes inside IC engine. Additionally, the application of CFD allows insights into various physical processes which are difficult to study experimentally. Even further, in the design and development process in an industrial context, CFD is applied for instance in the optimization of intake and engine geometries, leading to a significant reduction of development

cost as well as turnaround time. Based on common Reynolds averaged Navier-Stokes (RANS) turbulence modeling, this approach is by definition limited to the description of (statistical) mean values. In case highly transient and unsteady features such as cycle-to-cycle variations are investigated, this approach is not capable to capture this kind of phenomenon.

The ability to predict cyclic variations is given by the alternative turbulence modelling approach, namely large eddy simulation (LES)¹. In contrast to the statistical approach of RANS, the LES approach describes the filtered turbulent flow field, i.e. a significant amount of the turbulent spectrum is resolved and a smaller range of turbulent length scales needs to be modeled. The numerical cost however, caused by resolving smaller temporal and spatial scales, requires higher-order numerical schemes, smaller time steps and higher resolutions of the computational grids, lead to a significant increase of CPU-time and memory consumption compared to RANS.

An alternative modelling approach is the combination of both models in a hybrid RANS/LES approach, obtaining the attractive features of both methods. These methods provide the opportunity to use LES in regions, where its performance is known to be essentially superior to RANS. In other regions, where the accuracy and the averaged information on turbulent properties is sufficient, RANS can be used in order to save CPU-time. In contrast to pure RANS temporal fluctuations can be resolved in the LES regions in hybrid methods giving these approaches the potential to predict cycle-to-cycle variations or other turbulent flows of highly unsteady nature.

The structure of the work is as follows. A summary of the governing equations for chemically reacting flows is given in chapter 2. Chapter 3 presents an introduction to turbulence and turbulence modelling. The statistical approach based on Reynolds averaging is introduced in 3.2, where also an overview of RANS models and model hierarchy is given. The LES technique based on a filtering approach as well as popular LES models are discussed in section 3.4, followed by the motivation for hybrid approaches combining elements of both RANS and LES and a discussion of hybrid models in section 3.5. In section 3.5.2 a new hybrid two-scale VLES model is presented. The chapter closes with a discussion of methods for the generation of turbulent initial and boundary conditions (artificial turbulence), section 3.6. Chapter 4 gives an overview of premixed laminar and turbulent combustion in sections 4.1 and 4.2. Additionally modelling approaches for turbulent premixed combustion in the RANS context based on the progress variable 4.3 and on a level set approach (G -equation) 4.4 are discussed as well as combustion modelling in the LES context with an overview of LES-based combustion models for pre-mixed turbulent combustion. The adaptation of the G -equation to the hybrid two-scale VLES approach finalises the chapter. The numerics of the CFD solver employed in this work are presented in section 5. The application, evaluation and discussion of the developed techniques and modelling approaches is done in chapter 6, starting with an analysis of

¹The application of direct numerical simulation (DNS) is not considered as an option in terms of industrial applicability.

initialisation methods and influence of numerical schemes on the turbulent spectra in homogeneous, isotropic turbulence 6.1. The results of the simulation of a simplified engine configuration and multi-cycle simulation of a 4-valve model engine are discussed in sections 6.2 and 6.3 respectively. In order to demonstrate the feasibility to describe the effects of turbulence onto the flame propagation, the chapter closes with the numerical study of flame propagation in cylindrical vessel under high swirl condition 6.4. Summary and conclusions are given in chapter 7.

2 Physics of fluids

2.1 Fundamental equations of fluid mechanics

The description of fluid flow is based on equations describing the conservation of mass, momentum and energy. Considering the fluid as a continuum leads to the fundamental transport equation of fluid mechanics, the Navier-Stokes equation¹.

For compressible fluids in Cartesian coordinates the continuity equation, i.e. the conservation of mass, reads

$$\frac{\partial \rho}{\partial t} + \frac{\partial}{\partial x_i} (\rho U_i) = 0, \quad (2.1)$$

where ρ denotes the fluid density and U_i the x_i -velocity component. The conservation of momentum is described by

$$\frac{\partial \rho U_i}{\partial t} + \frac{\partial}{\partial x_j} (\rho U_i U_j) = -\frac{\partial p}{\partial x_i} + \frac{\partial \sigma_{ij}}{\partial x_j} + \rho g_i \quad (2.2)$$

with the viscous shear stress tensor σ_{ij} described by the Stokes relation

$$\sigma_{ij} = \underbrace{\mu \left(\frac{\partial U_i}{\partial x_j} + \frac{\partial U_j}{\partial x_i} \right)}_{2S_{ij}} - \frac{2}{3} \mu \frac{\partial U_k}{\partial x_k} \delta_{ij} \quad (2.3)$$

p denotes the pressure and g_i represents external body forces per unit mass, as for instance gravitational acceleration. The rate of strain tensor S_{ij} is defined as

$$S_{ij} = \frac{1}{2} \left(\frac{\partial U_i}{\partial x_j} + \frac{\partial U_j}{\partial x_i} \right) \quad (2.4)$$

A modified definition is usually employed for compressible flows in which the trace of the tensor is zero:

$$S_{ij}^* = \frac{1}{2} \left(\frac{\partial U_i}{\partial x_j} + \frac{\partial U_j}{\partial x_i} \right) - \frac{1}{3} \delta_{ij} \frac{\partial U_k}{\partial x_k}. \quad (2.5)$$

Using equation (2.5) the viscous shear stress tensor σ_{ij} can also be written in compact form as $\sigma_{ij} = 2\mu S_{ij}^*$. The transport equation for the total enthalpy h and species mass fraction Y_α read

$$\frac{\partial \rho h}{\partial t} + \frac{\partial \rho U_i h}{\partial x_i} = \frac{\partial p}{\partial t} + U_j \frac{\partial p}{\partial x_j} + \frac{\partial}{\partial x_j} \left(\frac{\lambda}{c_p} \frac{\partial h}{\partial x_j} \right) + \sigma_{ij} \frac{\partial U_i}{\partial x_j} \quad (2.6)$$

$$\frac{\partial \rho Y_\alpha}{\partial t} + \frac{\partial \rho U_i Y_\alpha}{\partial x_i} = \frac{\partial}{\partial x_i} \left(\frac{\mu}{Sc_\alpha} \frac{\partial Y_i}{\partial x_i} \right) + \dot{\omega}_\alpha \quad (2.7)$$

¹C.L.M.H. Navier was the first to derive these equations in 1823 despite his lack of understanding the full physics; in 1845 G.G. Stokes was the first to obtain a rigorous derivation of the Navier-Stokes equations.

where the diffusive transport in both equations is modelled using a gradient approach, namely Fourier's law for the enthalpy equation and Fick's law for the species mass fraction

$$J_i^\alpha = -\frac{\mu}{Sc_\alpha} \frac{\partial Y_\alpha}{\partial x_i}. \quad (2.8)$$

Sc_α denotes the Schmidt number, relating the diffusive transport of mass fractions to the dynamic viscosity. Note that equation (2.6) does not contain any source terms due to chemical reaction, since the total enthalpy h includes the chemical heat of formation.

The only terms which needs closure in equation (2.7) are the chemical reaction rates $\dot{\omega}_\alpha$. Each reaction rate contains the rates of progress τ_r of any elementary reaction r multiplied by the stoichiometric coefficient ν of species α in that reaction:

$$\dot{\omega}_\alpha = \sum_r \nu_{\alpha r} \tau_r = \sum_r (\nu_{\alpha r}^b - \nu_{\alpha r}^f) \tau_r. \quad (2.9)$$

The rate of progress is given by the forward (f) and backward (b) rate constants K_r and the product of the molar concentrations $[X]_\beta$ of the educt species:

$$\tau_r = K_r^f \prod_\beta [X]_\beta^{\nu_{\alpha\beta}^f} - K_r^b \prod_\beta [X]_\beta^{\nu_{\alpha\beta}^b}. \quad (2.10)$$

where the forward rate constants are usually modelled by a generalised Arrhenius approach

$$K_r^f = A_r T^{n_r} \exp\left(-\frac{E_r}{R_m T}\right), \quad (2.11)$$

while in most cases the backward reaction is linked to K_r^f by the equilibrium constant $K_{c,r}$ via

$$K_{c,r} = \frac{K_r^f}{K_r^b}. \quad (2.12)$$

Further details can be found in the standard literature, for example [36]. The link between pressure, temperature, species distribution and density is done by means of the ideal gas law

$$\frac{p}{\rho} = \sum_\alpha \frac{Y_\alpha}{W_\alpha} \mathcal{R} T, \quad (2.13)$$

where \mathcal{R} is the ideal gas constant and W_α the molecular weight of species α . Using the mean molecular weight W defined as

$$W = \left(\sum_\alpha \frac{Y_\alpha}{W_\alpha} \right)^{-1}, \quad (2.14)$$

equation (2.13) reduces to

$$p = \frac{\rho}{W} \mathcal{R} T, \quad (2.15)$$

2.2 Non-dimensional form

While for practical applications the dimensional form of the governing equation as given in the previous section is employed, the dimensionless variant is of importance for theoretical and fundamental studies. The non-dimensional variables are obtained by normalisation of the independent and dependent variables by reference values (indicated by the index R)

$$x_i^* = \frac{x_i}{l_R}, t^* = \frac{t \cdot U_R}{l_R};$$

$$\rho^* = \frac{\rho}{\rho_R}, U_i^* = \frac{U_i}{U_R}, p^* = \frac{p}{\rho_R U_R^2}, T^* = \frac{T}{T_R};$$

here, l_R , U_R , ρ_R and T_R represent a reference length, velocity, density and temperature respectively. Additional reference quantities required for the normalisation of the governing equations are the reference speed of sound c_R , the reference specific heat capacity at constant pressure c_{pR} , the reference dynamic viscosity μ_R , and finally the reference heat conductivity λ_R . Introducing the normalised variables into the governing equations (2.1), (2.2) and (2.6), and dropping the superscripts the following set of equations is obtained²:

$$\frac{\partial \rho}{\partial t} + \frac{\partial}{\partial x_i} (\rho U_i) = 0, \quad (2.16)$$

$$\frac{\partial \rho U_i}{\partial t} + \frac{\partial}{\partial x_j} (\rho U_i U_j) = -\frac{\partial p}{\partial x_i} + \frac{1}{Re} \frac{\partial \sigma_{ij}}{\partial x_j}, \quad (2.17)$$

$$\begin{aligned} \frac{\partial \rho h}{\partial t} + \frac{\partial \rho U_i h}{\partial x_i} &= Ma^2 \frac{\partial p}{\partial t} + Ma^2 U_j \frac{\partial p}{\partial x_j} \\ &+ \frac{1}{Pr Re} \frac{\partial}{\partial x_j} \left(\frac{\lambda}{c_p} \frac{\partial h}{\partial x_j} \right) + \frac{Ma^2}{Re} \sigma_{ij} \frac{\partial U_i}{\partial x_j}. \end{aligned} \quad (2.18)$$

In the non-dimensional form of the conservations equation three characteristic numbers appear, namely the Reynolds number Re , the Mach number Ma , and the Prandtl number Pr , which are defined as

$$Re = \frac{\rho l u}{\mu} = \frac{l u}{\nu}, \quad Ma = \frac{u}{c}, \quad Pr = \frac{c_p \mu}{\lambda}, \quad (2.19)$$

where the index R indicating reference quantities has been omitted for brevity. These non-dimensional numbers allow to characterise and to classify the state of flow.

The Mach number Ma , defined as the ratio of the fluid velocity u to the (local) speed of sound c , see equation (2.19), is a measure for the compressibility of the flow. For small

²Here, the external body forces have been omitted for brevity.

| | | |
|----------------------------|--------------------------------------|------------------------------|
| model air plane | $l = 1 \text{ m}, u = 1 \text{ m/s}$ | $Re = 7 \cdot 10^4$ |
| cars | $u = 3 \text{ m/s}$ | $Re = 6 \cdot 10^5$ |
| air planes | $u = 30 \text{ m/s}$ | $Re = 2 \cdot 10^7$ |
| atmospheric flows | | $Re \approx 7 \cdot 10^{20}$ |
| internal combustion engine | | $Re = 6 \cdot 10^4$ |

Table 2.1: Sample of characteristic Reynolds numbers.

Ma -numbers ($Ma < 0.3$), the flow can be considered as incompressible, which implies that the enthalpy equation is decoupled from the momentum and continuity equations. This effect can be seen in the enthalpy equation (2.18), considering the limit $Ma \rightarrow 0$, as in this limit, the enthalpy becomes independent of pressure.

The Reynolds number Re represents the ratio of inertia to viscous forces and is the most important dimensionless number in fluid dynamics. By means of the Reynolds number a criterion for determining the state of a fluid flow (laminar/turbulent) can be derived. Qualitatively speaking laminar flow occurs at low Reynolds numbers where viscous forces are dominant, while turbulent flow occurs at high Reynolds numbers, at which the inertia forces dominate the fluid motion. In table 2.1 typical values of the Re number for some aerodynamic flows are given.

For gaseous fluids the Prandtl-number Pr is of the order of unity.

3 Description and modelling of turbulent flows

In engineering applications almost all flows can be characterised as being turbulent. The accurate description of these flows, however, is by no means easy, a fact which is already apparent when a definition for *turbulence* is sought after. Usually the phenomenon is described by listing its characteristic features:

- turbulent flows are irregular; therefore a purely deterministic approach to turbulence becomes impractical, as it appears not to be feasible to describe the turbulent motion in all details as a function of space and time coordinate; however, the determination of *average* values is regarded as possible;
- turbulent flows are diffusive, thus causing rapid mixing and increased rates of momentum, heat and mass transfer;
- turbulent flows are rotational, thus turbulence is associated with vorticity;
- turbulent flows occur at *high Reynolds numbers*; with increasing Reynolds number the complexity and the range of existing scales increase; from a numerical point of view the wide separation between the largest and the smallest scales of turbulence is the source for severe problems;
- turbulent flows are dissipative, removing (kinetic) energy from the mean flow via the energy cascade, see page 10;
- turbulence is a continuum phenomenon and thus can be treated by means of continuum mechanics, see page 11;
- turbulence is a feature of fluid flows, and not of fluids; this implies that the main characteristics of turbulent flows are not controlled by the molecular properties of the particular fluid;
- turbulence is inherently three dimensional and transient.

3.1 Turbulence fundamentals

The motion of fluids is governed by the Navier-Stokes equations, cf. equations (2.1)–(2.2), for both laminar and turbulent flow. Supplemented by appropriate initial and boundary conditions these equations form a *deterministic* set of equations based on the principles classical mechanics. As pointed out by Pope [94] in any physical flow there are perturbations and uncertainties in the initial and boundary conditions to which the turbulent flow field displays an acute sensitivity. However this sensitivity occurs at

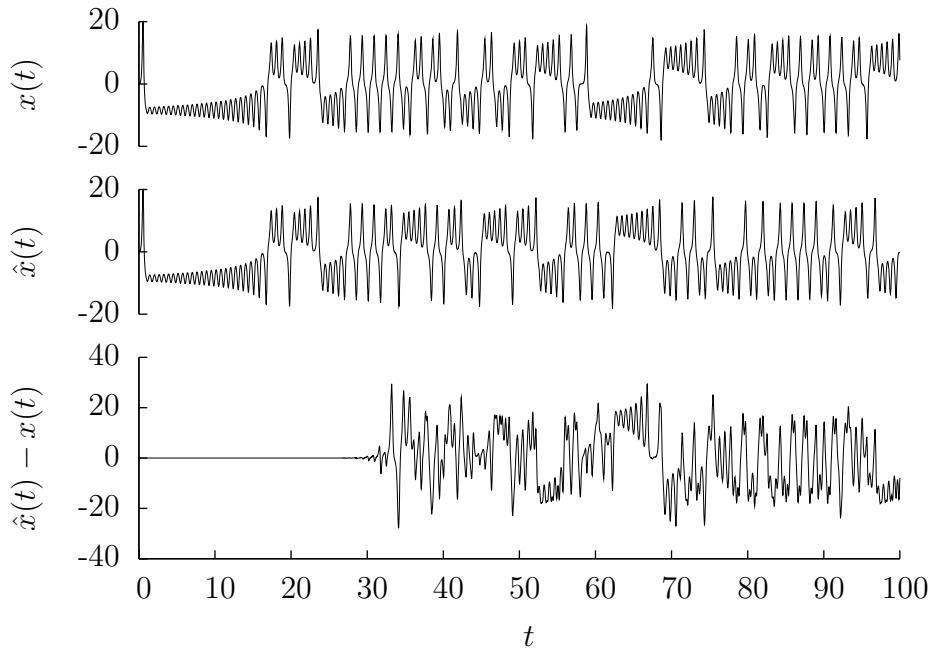


Figure 3.1: Time histories from the Lorenz equations (3.1)–(3.3).

high Re -numbers as demonstrated by the classical pipe flow experiment conducted by O. Reynolds [97] in the late 19th century. Considering the dimensionless momentum equations (2.17), the Re -number dependency indicates that the non-linear term, i.e. for incompressible flows $\frac{1}{Re} \frac{\partial^2 U_i}{\partial x_j^2}$, is responsible for the observed behaviour. This behaviour is well known for coupled ordinary differential equations as well as in the context of dynamical systems [39].

A classical example of the sensitivity to disturbances in the initial conditions for a coupled system of non-linear differential equations is the Lorenz system [66], described by:

$$\dot{x} = \sigma \cdot (y - x) \quad (3.1)$$

$$\dot{y} = \rho \cdot x - y - x \cdot z \quad (3.2)$$

$$\dot{z} = -\beta \cdot z + x \cdot y \quad (3.3)$$

with parameters σ , β , and ρ , and where the dot denotes the temporal derivative. This system has been employed for modelling the motion of particles subject to atmospheric forces. The time histories for $x(t)$ obtained by numerical integration for two slightly different initial conditions x_0 and \hat{x}_0 with $\Delta x = \hat{x}_0 - x_0 = 10^{-6}$ are given in figure 3.1 along with the difference Δx . Initially both solutions are indistinguishable, but starting around $t = 30$ a discrepancy becomes clearly visible, and at around $t = 35$ both signals become fully uncorrelated. In the example the initial condition has been disturbed by

10^{-6} which is well below the accuracy available experimentally in practical applications as well as within the numerical accuracy due to accumulated round-off errors. Still this small deflection is sufficient to lead to an unpredictable behaviour of the system.

Similar to the Navier-Stokes equations, which have a stable (laminar) solution at sufficiently low Re -number and a chaotic turbulent solution at high Re -number, the coefficients of the Lorenz system determine the qualitative behaviour of the system. For values of $\rho > 24.74$ with fixed values for σ and β , the system reaches a stable steady state while for larger values the previously discussed behaviour arises. This implies that even if a direct numerical simulation¹ was feasible, a major hurdle would be defining precise initial and boundary conditions. As demonstrated at high(er) Re number the flow is unstable as even small perturbations may excite the already existing small scales, leading to quasi unpredictable results.

While the behaviour of the system in physical space is characterised by its random nature, an analysis of the system in phase space reveals a more deterministic structure. Here an important attractor can be observed which determines the long-term properties of the system. While the temporal evolution of the individual solutions components exhibits the previously discussed erratical behaviour, the motion in phase space displays a strict pattern, which resembles a butterfly object with two wings, known as the Lorenz attractor. This observation loosely corresponds to the structure of velocity correlations, section 3.2.2.

The scales of turbulent motion. Turbulent fluid motion is characterised by a wide range of scales which descriptively can be thought of as eddies of different sizes. The time and length scale associated with these turbulent eddies are represented by frequencies and wavelengths which are obtained by a Fourier analysis of the turbulent flow history. The size of the eddies is limited by the characteristic size of the flow on the upper side, for instance the diameter for pipe flows, while the size of the smallest eddies is determined by effects of viscous dissipation. Richardson [100] introduced the idea of the energy cascade by assuming that the large turbulent eddies are unstable and break up transferring their energy to smaller and smaller eddies, until the molecular viscosity is effective in dissipating the kinetic energy. Thus energy is added at the largest scales while being dissipated at the smallest. During the break-up process, all directional information is lost, the smallest (turbulent) scales can therefore assumed to be isotropic. This assumption is known as *Kolmogorov's hypothesis of local isotropy*. The rate at which the small scales receive energy from the larger scales is equivalent to the dissipation rate ε . The statistics of the small scale motion is therefore uniquely determined by the viscosity ν and the dissipation rate ε . Based on these two parameter unique length, time and velocity scales can be formed being characteristic for the small scale motion.

¹DNS - a simulation where the complete spectrum of turbulent fluctuations is simulated without any turbulence model.

These scales are called the Kolmogorov length, velocity, and time scales:

$$\text{length scale: } \eta_k = (\nu^3/\varepsilon)^{1/4} \quad (3.4)$$

$$\text{time scale: } \tau_k = (\nu/\varepsilon)^{1/2} \quad (3.5)$$

$$\text{velocity scale: } v_k = (\nu\varepsilon)^{1/4} \quad (3.6)$$

The Reynolds number associated with the Kolmogorov scales is unity

$$Re_k = \frac{\eta_k v_k}{\nu} = 1,$$

which indicates that the viscous dissipation is important solely on the small scale turbulence. For large scale turbulence with characteristic velocity and length scales u' and ℓ_t , the viscous effects are negligible². The energy transfer therefore depends only on u' and ℓ_t , leading by means of dimensional analysis to following scaling for the turbulent rate of dissipation:

$$\varepsilon \sim \frac{u'^3}{\ell_t}. \quad (3.7)$$

Introducing the turbulent Reynolds number Re_t as $Re_t = \frac{u' \ell_t}{\nu}$, the following correlation between the Kolmogorov micro-scales and the integral scale can be derived:

$$\frac{\eta_k}{\ell_t} = (Re_t)^{-3/4}, \quad \frac{\tau_k}{t} = (Re_t)^{-1/2}, \quad \frac{v_k}{u'} = (Re_t)^{-1/4},$$

where $t = \ell_t/u'$ denotes the time scale for the large scale turbulence.

Validity of the Navier-Stokes equation for turbulent flows. As postulated above, turbulence is a continuum phenomenon and therefore the Navier-Stokes equations are valid. This validity can be shown by an estimation of the ratio of the mean free path length λ on a molecular basis and the smallest turbulent scale, the Kolmogorov length scale η_k . Based on kinetic theory of gases the viscosity of a fluid can be determined as $\mu = \rho c \lambda$ with $c = \sqrt{\gamma \mathcal{R}T}$ being the speed of sound. The ratio λ/η_k then becomes

$$\frac{\lambda}{\eta_k} = \frac{\nu/c}{(\nu^3/\varepsilon)^{1/4}} = \frac{(\nu\varepsilon)^{1/4}}{c} = \frac{v_k}{c},$$

where the Kolmogorov velocity scale $v_k = (\nu\varepsilon)^{1/4}$, eqn. (3.6) has been introduced. Extending the previous equation with u' and using the previously discussed relations between the integral and Kolmogorov scales, the ratio can be expressed in terms of the turbulent Reynolds number Re_t , the integral velocity scale u' and the speed of sound c as

$$\frac{\lambda}{\eta_k} = \frac{u'}{c} Re_t^{-1/4} = Ma_t Re_t^{-1/4}.$$

²The thorough definition and discussion of the integral length scale ℓ_t will be done in section 3.2.2

The turbulent Mach number $Ma_t = u'/c$ is usually, i.e. in technical application, smaller than unity, $Ma_t \leq 1$. The Reynolds number and correspondingly also the turbulent Reynolds number is much greater than unity, $Re \gg 1$, which leads to $\lambda/\eta_k \ll 1$. This implies that the smallest turbulent scales η_k are significantly larger than the molecular length scale λ . The estimation therefore demonstrates that turbulence is indeed continuum phenomenon and that the Navier-Stokes equations are valid for describing turbulence flows.

Resolution requirements for Direct Numerical Simulation. In order to illustrate numerical problems associated with the simulation of turbulent flows the mesh resolution can be estimated. The smallest turbulent scale are of order $\mathcal{O}(Re^{-3/4})$ which implies that the mesh spacing h is of the same order, $h \approx Re^{-3/4}$. Consequently in three dimensions $1/h^3$ mesh points are needed, i.e. $N \approx Re^{9/4}$ mesh points per time step. For atmospheric flows with a Reynolds number of around 10^{20} , see table 2.1, this leads to $N \approx 10^{45}$ nodes – a value well beyond the capability of any computer system in the foreseeable future. The consequence, already from the plain numerical point of view, is that not all scales can be resolved, i.e. a reduction of the complexity, the range of scales, and the degrees of freedom of the problem is required.

Averaging. As discussed in the previous sections the boundary conditions of the Navier-Stokes equations are of an uncontrollable and unpredictable nature which allows to characterise them as *random forcing*. Consequently in a stochastic sense the random disturbances produce random responses. In such settings the calculation of average quantities makes more sense than the determination of instantaneous point values. Furthermore from an engineering point-of-view the focus lies usually not in the local time-history of fluctuating quantities but in mean values.

In turbulent-flow experiments and simulations several kinds of averaging techniques are employed to define mean quantities. For statistically stationary flows the time average (over a sufficiently large time interval T) is defined by

$$\langle U(t) \rangle_T := \frac{1}{T} \int_t^{t+T} U(t') dt'. \quad (3.8)$$

The averaging interval T must be *sufficiently large* compared to the typical time scale of the fluctuations [34]. On the other hand, in case equation (3.8) should be used for unsteady flows T must be sufficiently small enough to capture the mean flow fluctuations; obviously this definition is not suitable for highly transient phenomena; however it is well suited for a descriptive understanding. For flows that can be repeated or replicated, the ensemble average is defined by

$$\langle U(t) \rangle_N := \frac{1}{N} \sum_N U^{(n)}(t) \quad (3.9)$$

where U^n is the measurement of the n^{th} realisation, and N is the total number of realisations. N must be large enough to eliminate the effects of the fluctuations. The ensemble can be considered as a virtual set of flows in which all controllable variables are identical. Both definitions resemble experimental techniques and represent the classical approach employed in standard text-books. For in the limits of $T, N \rightarrow \infty$, i.e. for large averaging intervals and large number of ensemble members/realisations, the ergodicity theorem [103] shows that both definitions are equivalent.

Considering the random nature of the turbulent quantities the flow field can be treated by means of statistical tools. In particular a random variable U is completely characterised by its *probability density function* (pdf), denoted by $f(U)$. The mean or expectation of the random variable U is then defined as the first moment by

$$\langle U \rangle := \int_{-\infty}^{\infty} V f(V) dV, \quad (3.10)$$

which represents the probability-weighted average of all possible values of U . This statistical approach, also referred to as Reynolds averaging, is discussed in detail in section 3.2.

In flows in which the central features of turbulence are inherently dynamic, the previous averaging operations erase the features sought after. These features can be retained by using a *local, spatial* average of the flow variables. Interestingly, in a pioneering paper [98], O. Reynolds used a spatial average over a mesh cell (for example a box about $\mathbf{x} = (x_1, x_2, x_3)$ with equal sides of length *delta*) of the form

$$\bar{\mathbf{u}}(\mathbf{x}, t) = \frac{1}{\delta^3} \int_{x_1-\delta/2}^{x_1+\delta/2} \int_{x_2-\delta/2}^{x_2+\delta/2} \int_{x_3-\delta/2}^{x_3+\delta/2} \mathbf{u}(y_1, y_2, y_3, t) dy_1 dy_2 dy_3. \quad (3.11)$$

Generalising the previous equation leads to the (spatial) filtering approach, formally defined by the convolution integral

$$\bar{\mathbf{u}}(\mathbf{x}, t) = \int G(\mathbf{x} - \mathbf{x}') \mathbf{u}(\mathbf{x}', t) d\mathbf{x}', \quad (3.12)$$

where G denotes a (spatial) filter kernel. This approach has been formally introduced by Leonard [61] and forms the basis for Large Eddy Simulation (LES) approach, discussed in section 3.4.

3.2 Statistical modelling

For engineering applications the focus of interest usually lies on just a few quantitative properties of a turbulent flow, such as average forces on a surface (drag/lift coefficient) or the degree of mixing between two incoming streams of fluids. Details of the flow

structure, especially of small scale turbulent structures, are of minor interest in comparison to average or mean values. This motivates to express all quantities as a sum of a mean and fluctuation part. In honour of the pioneering work on the statistical approach to turbulence modelling, this approach is referred to as Reynolds averaging or Reynolds decomposition. Characterising the fluctuating part as random quantities leads to a statistical description of the flow, which will be briefly discussed in the following. A thorough introduction of the statistical approach can be found in the classical textbooks on turbulence, for instance [94, 103].

3.2.1 The statistical description of turbulent flows

An instantaneous realisation of a velocity component $U(\mathbf{x}, t)$ at a specific point in space and time in a turbulent flow field can be considered as be a random variable. The independent scalar variable V is referred to as the *sample-space* variable corresponding to U . The probability p that U is smaller than a given V defines the cumulative distribution function (CDF)

$$F_u(V) \equiv p\{U < V\}. \quad (3.13)$$

The probability density function (*pdf*) of U being equal to V is defined as the derivative of the CDF,

$$f_U(V) \equiv \frac{dF_u(V)}{dV}, \quad (3.14)$$

satisfying the normalisation condition

$$\int_{-\infty}^{\infty} f_U(V) dV = 1. \quad (3.15)$$

The probability of finding U in a particular interval $[V_a, V_b]$ is given by the integral of the pdf over that interval

$$p\{V_a \leq U \leq V_b\} = \int_{V_a}^{V_b} f_U(V) dV. \quad (3.16)$$

The mean or expectation of the random variable U is defined by

$$\langle U \rangle \equiv \int_{-\infty}^{\infty} V f_U(V) dV, \quad (3.17)$$

which can also be referred to as the first moment of U . The fluctuation of U , denoted as u is defined as the deviation from the mean,

$$u \equiv U - \langle U \rangle. \quad (3.18)$$

Note that by definition the mean of the fluctuation is zero, i.e. $\langle u \rangle = 0$. The second moment of U , or the variance of U , is given by the mean square fluctuation,

$$\langle u^2 \rangle = \int_{-\infty}^{\infty} (V - \langle U \rangle)^2 f(V) dV, \quad (3.19)$$

The square root of the variance, $\sqrt{\langle u^2 \rangle}$, defines the standard deviation, and is also referred to as the root mean square or *r.m.s.* of U , denoted as u' or u_{rms} .

The extension of the previous definitions to random fields is straight forward. Denoting the one-point, one-time joint pdf³ of the field \mathbf{V} , for instance the turbulent velocity field, by $f(\mathbf{V}; \mathbf{x}, t)$, the expectation and fluctuation are defined analogous to the scalar case, (3.16) and (3.18), as

$$\langle \mathbf{U}(\mathbf{x}, t) \rangle = \iiint_{-\infty}^{+\infty} \mathbf{V} f(\mathbf{V}; \mathbf{x}, t) d\mathbf{V}; \quad (3.20)$$

$$\mathbf{u}(\mathbf{x}, t) = \mathbf{U}(\mathbf{x}, t) - \langle \mathbf{U}(\mathbf{x}, t) \rangle. \quad (3.21)$$

In operator notation the averaging process can also be written as

$$\langle \mathbf{U} \rangle = \mathcal{R}\{\mathbf{U}\}, \quad u = \mathbf{U} - \mathcal{R}\{\mathbf{U}\} \quad (3.22)$$

where \mathcal{R} denotes the Reynolds operator.

Favre-averaging. The previous approach, referred to as *Reynolds decomposition* in the field of fluid dynamics, is used for incompressible flows. Introducing the Reynolds averaged variables into the conservation equation for incompressible flows leads to the Reynolds average Navier-Stokes (RANS) equations, see section 3.2.3. For the motion of compressible media the introduction of the Reynolds averaged quantities leads to additional correlation in the equations for the average quantities. Instead a density weighted averaging, called *Favre averaging*, is employed [33]

$$\tilde{\mathbf{U}} = \frac{\langle \rho \mathbf{U} \rangle}{\langle \rho \rangle}. \quad (3.23)$$

The corresponding *Favre decomposition* is given by

$$\mathbf{U}(\mathbf{x}, t) = \tilde{\mathbf{U}}(\mathbf{x}, t) + \mathbf{u}''(\mathbf{x}, t), \quad (3.24)$$

where the tilde denotes Favre averaging, and the Favre fluctuations are indicated by double primes. Note that *Favre averaging eliminates the fluctuations from the averaged*

³The semicolon in $f(\mathbf{V}; \mathbf{x}, t)$ indicates that f is a density with respect to the sample space variable on the left of the semicolon, while f is a function with respect to the variables on the right side.

equations and does not remove the effects of the density fluctuations on turbulence and is therefore a mathematical simplification, not a physical one [127]. Introducing the Favre operator \mathcal{F} the Favre averaging can analogous to the Reynolds averaging, eqn. (3.22), be written as

$$\tilde{\mathbf{U}} = \mathcal{F}\{\mathbf{U}\}, \quad \mathbf{u}'' = \mathbf{U} - \mathcal{F}\{\mathbf{U}\}. \quad (3.25)$$

The properties of the Favre operator \mathcal{F} are analogue to those of the Reynolds operator \mathcal{R} and are summarised in [3, 127].

3.2.2 Correlations and turbulent spectra

In order to describe the temporal evolution of a fluctuating function $u(t)$ information about the relation of values of u at different time is required. The correlation $\langle u(t)u(t + \tau) \rangle$ between two values of u at different times is referred to as the autocorrelation function. Normalisation of the autocorrelation by $\langle u(t)^2 \rangle$ defines the autocorrelation coefficient $\rho(\tau)$

$$\rho(\tau) \equiv \frac{\langle u(t)u(t + \tau) \rangle}{\langle u(t)^2 \rangle} = \rho(-\tau). \quad (3.26)$$

For processes arising in turbulent flows the autocorrelation $\rho(\tau)$ can be expected to diminish as time difference τ increases. Usually $\rho(\tau)$ decreases sufficiently fast enough for the integral

$$\mathcal{T} \equiv \int_0^{\infty} \rho(\tau) d\tau \quad (3.27)$$

to converge. The value of \mathcal{T} is then a rough measure of the interval over which $u'(t)$ is correlated with itself; therefore \mathcal{T} is referred to as the *integral time scale*.

The two-point, one time auto-covariance is the most simple statistic containing information about the spatial structure of a turbulent field. Usually referred to as the *two-point correlation* it is defined as

$$R_{ij}(\mathbf{r}, \mathbf{x}, t) \equiv \langle u_i(\mathbf{x}, t)u_j(\mathbf{x} + \mathbf{r}, t) \rangle, \quad (3.28)$$

where \mathbf{r} denotes the distance vector. Considering homogeneous turbulence the two-point correlation $R_{ij}(\mathbf{r}, \mathbf{t})$ is independent of the spatial coordinate and depends solely on the distance between two spatial positions. As a consequence of isotropy, R_{ij} can be expressed in terms of two scalar functions $f(r, t)$ and $g(r, t)$ as

$$\frac{R_{ij}}{\langle u'^2 \rangle} = g(r, t)\delta_{ij} + [f(r, t) - g(r, t)] \frac{r_i r_j}{r^2} \quad (3.29)$$

where $f(r, t)$ denotes the longitudinal, and $g(r, t)$ the transversal autocorrelation function. Due to continuity there is a dependency between the two functions given by

$$g(r, t) = f(r, t) + \frac{1}{2}r \frac{\partial}{\partial r} f(r, t). \quad (3.30)$$

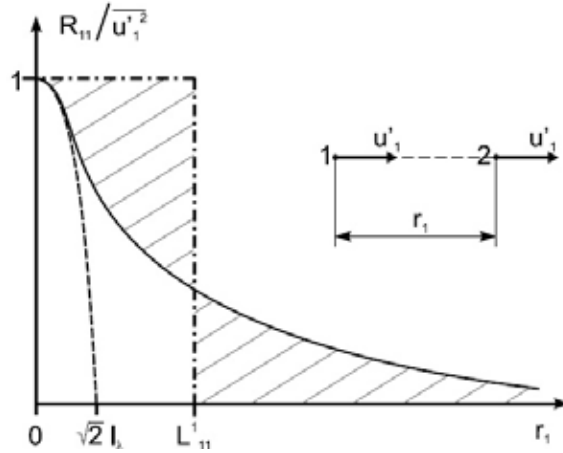


Figure 3.2: Geometric interpretation of the longitudinal integral and Taylor length scale [103].

This implies that in isotropic turbulence the longitudinal autocorrelation function completely determines the two-point correlation R_{ij} . Note that for $r = 0$ both f and g are equal to unity and tend asymptotically to zero for increasing r . Based on the autocorrelation functions two distinct length scale can be defined. The first length scale is the (longitudinal) integral length scale

$$L_{11}(t) = \ell_t = \int_0^{\infty} f(r, t) dr. \quad (3.31)$$

L_{11} is characteristic of the larger eddies. The second scale is the (transversal) Taylor micro-scale λ_g defined by

$$\frac{1}{\lambda_g^2} = \frac{1}{2} g''(0, t). \quad (3.32)$$

where the double-prime indicates the second temporal derivative. It is always smaller than the integral length scale ($\lambda_g < L_{11}$) and their relation is determined by the Reynolds number. Figure 3.2 shows the geometric interpretation of the length scales.

While the meaning of the integral length scale has already been discussed in section 3.1, the physical interpretation of the Taylor micro-scale is still subject to discussion. For high Reynolds numbers it can be shown the λ_g is intermediate in size between the integral length scale ℓ_t and the Kolmogorov scale η_K . Recently two studies [67, 125] independently indicated the Taylor length scale is a measure for the eddy size difference at which the turbulent eddies are able to interact.

As R_{ij} is independent of the spatial coordinate the information of the correlation can be expressed in wave number space. The Fourier transform of $R_{ij}(\mathbf{r}, t)$ defines the

velocity spectrum tensor $\Phi_{ij}(\boldsymbol{\kappa}, t, \boldsymbol{\kappa})$ [123] as given by

$$\Phi_{ij}(\boldsymbol{\kappa}, t) = \frac{1}{(2\pi)^3} \iiint_{-\infty}^{+\infty} e^{-i\boldsymbol{\kappa}\cdot\mathbf{r}} R_{ij}(\mathbf{r}, t) \, d\mathbf{r}, \quad (3.33)$$

and the inverse transform is

$$R_{ij}(\mathbf{r}, t) = \iiint_{-\infty}^{+\infty} e^{i\boldsymbol{\kappa}\cdot\mathbf{r}} \Phi_{ij}(\boldsymbol{\kappa}, t) \, d\boldsymbol{\kappa}. \quad (3.34)$$

The significance of the velocity spectrum becomes visible when considering the special case of $\mathbf{r} = 0$ in equation (3.34), which yields

$$R_{ij}(0, t) = \langle u_i u_j \rangle = \iiint_{-\infty}^{+\infty} \Phi_{ij}(\boldsymbol{\kappa}, t) \, d\boldsymbol{\kappa}. \quad (3.35)$$

Thus $\Phi_{ij}(\boldsymbol{\kappa}, t)$ is the contribution of velocity modes with wave number $\boldsymbol{\kappa}$ to the covariance $\langle u_i u_j \rangle$. By removing all directional information of the velocity spectrum tensor, the *energy spectrum function* is obtained

$$E(\kappa, t) \equiv \iiint_{-\infty}^{+\infty} \Phi_{ij}(\boldsymbol{\kappa}, t) \delta(|\boldsymbol{\kappa}| - \kappa) \, d\boldsymbol{\kappa} \quad (3.36)$$

$$= \oint \frac{1}{2} \Phi_{ij}(\boldsymbol{\kappa}, t) \, d\mathcal{S}(\kappa), \quad (3.37)$$

where $\mathcal{S}(\kappa)$ denotes a sphere with radius κ in wave number space whose centre lies at the origin, and δ denotes the Dirac delta function⁴. The meaning of the energy spectrum function becomes clearer after the integration of (3.36) over all wave numbers κ , leading to

$$\int_0^{\infty} E(\kappa, t) \, d\kappa = \frac{1}{2} R_{ii}(0, t) = \frac{1}{2} \langle u_i u_i \rangle. \quad (3.38)$$

$k = \frac{1}{2} \langle u_i u_i \rangle$ represents the kinetic energy of the fluctuations. $E(\kappa, t) \, d\kappa$ therefore represents the contribution from the modes in the interval $\kappa \leq |\boldsymbol{\kappa}| \leq \kappa + \Delta\kappa$ to the turbulent kinetic energy. Thus $E(\kappa)$ is the density of (turbulent) kinetic energy per unit wave number κ .

⁴The Dirac delta function is defined as $\delta(x) = \begin{cases} 0, & \text{for } x \neq 0, \\ \infty, & \text{for } x = 0. \end{cases}$ A detailed discussion of the properties of the Dirac delta function can be found for example in Appendix C of [94].

Based on dimensional analysis, the Kolmogorov local isotropy and the scale similarity hypothesis, the form of the Kolmogorov spectra can be determined. Rather than to present a formal derivation, a less rigorous approach is employed in the following. Assuming that the wave number κ can be related to the inverse of a eddy size ℓ_n as

$$\kappa = \ell_n^{-1}, \quad \eta_K \leq \ell_n \leq \ell,$$

the turbulent kinetic energy at that scale ℓ_n can be estimated via equation (3.7) by

$$v_n^2 \sim (\varepsilon \ell_n)^{2/3} = \varepsilon^{2/3} \kappa^{-2/3}.$$

The density in wave number space is given by the derivative with respect to κ^5 , leading to the well know $-5/3$ law for the energy spectrum in the inertial subrange.

$$E(\kappa) = \frac{dv_n^2}{d\kappa} \sim \varepsilon^{2/3} \kappa^{-5/3}$$

The same results can be obtained by dimensional analysis on basis of the energy cascade. For high Reynolds numbers, a wide separation of scales can be assumed. The cascade process is therefore independent of the statistics of the energy containing eddies as well as of viscosity effects. This implies that a range of wave numbers exists where $E(\kappa)$ depends solely on ε and κ . On dimensional grounds the energy spectra then has the form

$$E(\kappa) = C_K \varepsilon^{2/3} \kappa^{-5/3}, \quad (3.39)$$

where C_K is the Kolmogorov constant. In this range of wave numbers the transfer of energy is dominated by inertia. The existence of this inertial subrange has been verified by numerous experimental and numerical studies. Interestingly, nowadays a direct numerical simulation is only then considered as trustworthy in case it is able to reproduce the Kolmogorov spectra, eq. (3.39).

Generalisation of the Kolmogorov spectrum for wave number outside the inertial range can be achieved by the following model spectrum,

$$E(\kappa) = C \varepsilon^{2/3} \kappa^{-5/3} f_L(\kappa \ell) f_\eta(\kappa \eta), \quad (3.40)$$

where f_L and f_η are two non-dimensional functions accounting for the shape of the energy-containing and the dissipation range respectively. In the inertial range, both f_L and f_η are essentially unity, so that the Kolmogorov spectrum is recovered.

3.2.3 Average transport equations

Instead of solving the instantaneous transport equations, transport equations for the averaged flow properties are required. Consider the most general form of an evolution equation for a time dependent variable ϕ which is given by

$$\frac{\partial \phi}{\partial t} = F(\phi, \mathbf{x}, t, \dots),$$

⁵This is based in the assumption of the locality of the energy cascade.

where F is an arbitrary complex right hand side. Introducing the Reynolds averaged value $\langle \phi \rangle = \mathcal{R}(\phi)$ and taking the temporal derivative leads to

$$\frac{\partial \langle \phi \rangle}{\partial t} = \frac{\partial}{\partial t} \mathcal{R}(\phi) = \mathcal{R} \left(\frac{\partial \phi}{\partial t} \right) = \mathcal{R} (F(\phi, \mathbf{x}, t, \dots)) ,$$

where the properties of the Reynolds operation, eqn. (3.22), have been employed. Therefore, to obtain a transport equation for the averaged quantities it is sufficient to apply the Reynolds operator onto the governing equations. This leads for the continuity (2.1) and the momentum equations (2.2) to

$$\frac{\partial \langle \rho \rangle}{\partial t} + \frac{\partial \langle \rho \rangle \tilde{u}_j}{\partial x_j} = 0 , \quad (3.41)$$

$$\frac{\partial \langle \rho \rangle \tilde{u}_i}{\partial t} + \frac{\partial \langle \rho \rangle \tilde{u}_i \tilde{u}_j}{\partial x_j} = \frac{\partial \langle p \rangle}{\partial x_i} + \frac{\partial}{\partial x_j} \left(\tilde{\sigma}_{ij} - \langle \rho \rangle \widetilde{u_i'' u_j''} \right) . \quad (3.42)$$

In the momentum equation a new term arises,

$$\tau_{ij} = - \langle \rho \rangle \widetilde{u_i'' u_j''} , \quad (3.43)$$

which is called the (Favre averaged) *Reynolds stress tensor*. These products of fluctuating velocities stem from the non-linear convective part of the left hand side of the momentum equations. Evidently these correlations play a crucial role in the equations for the mean velocity field as a comparison with the instantaneous equation reveals: without the Reynolds stresses both equations would be identical (as is the case for the instantaneous and averaged continuity equation). This leads directly to the closure problem of turbulence, as the Reynolds tensor τ_{ij} cannot be readily expressed in terms of mean quantities, for instance \tilde{U}_i , $\langle \rho \rangle$, $\langle p \rangle$. Therefore the Reynolds averaged Navier-Stokes equations are *unclosed*, which means that there exist more unknown quantities to solve for than equations available. To close the Reynolds averaged Navier-Stokes equations (3.41)–(3.42), a set of transport equations for the Reynolds stresses τ_{ij} can be derived by multiplying the Navier-Stokes equations by the fluctuating velocity and then time average the product. Unfortunately, these Reynolds stress equations, given below for the simplified transient, incompressible case (3.44), contain amongst others triple correlation of the velocity fluctuations.

$$\begin{aligned} \frac{\partial \langle u_i' u_j' \rangle}{\partial t} + \langle u \rangle_k \frac{\partial \langle u_i' u_j' \rangle}{\partial x_k} &= - \langle u_i' u_k' \rangle \frac{\partial \langle u \rangle_j}{\partial x_k} - \langle u_j' u_k' \rangle \frac{\partial \langle u \rangle_i}{\partial x_k} + \left\langle \frac{p'}{\rho} \left(\frac{u_i'}{\partial x_j} + \frac{u_j'}{\partial x_i} \right) \right\rangle \\ &\quad - \frac{\partial}{\partial x_k} \left[\langle u_i' u_j' u_k' \rangle + \frac{\langle p' u_j \rangle}{\rho} \delta_{ij} + \frac{\langle p' u_i \rangle}{\rho} \delta_{ij} - \nu \frac{\partial \langle u_i' u_j' \rangle}{\partial x_k} \right] \\ &\quad - 2\nu \left\langle \frac{\partial u_i'}{\partial x_k} \frac{\partial u_i'}{\partial x_k} \right\rangle \end{aligned} \quad (3.44)$$

This demonstrates the closure problem of turbulence. Due to the non-linearity of the convective term in the Navier-Stokes equations additional, higher order correlations are generated when higher moments are taken. This is not surprising, as the operations are strictly of mathematical nature and no additional physical principles are introduced. Therefore this procedure cannot lead to a closed system where the number of available equations balances the number of unknowns. In order to close the equations, it is required to express the Reynolds stresses in term of *known quantities*. The term “known quantities” refers to flow properties for which a model expression or transport equation is available; considering equations (3.41)– (3.42) this implies that an expression for $\widetilde{u_i''u_j''}$ in terms of mean quantities \widetilde{u}_i is sought after. The procedure of deriving the corresponding relations is termed *turbulence modelling*.

3.3 RANS turbulence models

As a consequence of the averaging procedure the Reynolds averaged transport equations contain unknown correlations due to the non-linearity of the convective term. To close the equations additional algebraic or differential equations are required, i.e. a turbulence model needs to be provided.

The following discussion will focus on constant-density flows, i.e. flows in which ρ is independent of \mathbf{x} and t , for the sake of brevity⁶. For incompressible flow the continuity and momentum equations are given by

$$\begin{aligned} \frac{\partial U_j}{\partial x_j} &= 0, \\ \rho \frac{\partial U_i}{\partial t} + \rho \frac{\partial}{\partial x_j} (U_j U_i) &= \frac{\partial p}{\partial x_i} + \frac{\partial \sigma_{ij}}{\partial x_j}. \end{aligned}$$

with $\sigma_{ij} = 2\mu S_{ij}$, and the strain-rate tensor is $S_{ij} = 1/2(\partial U_i/\partial x_j + \partial U_j/\partial x_i)$. The corresponding Reynolds averaged equations of motion in conservative form read

$$\frac{\partial \langle U_j \rangle}{\partial x_j} = 0, \quad (3.45)$$

$$\rho \frac{\partial \langle U_i \rangle}{\partial t} + \rho \frac{\partial}{\partial x_j} (\langle U_j \rangle \langle U_i \rangle) = \frac{\partial \langle p \rangle}{\partial x_i} + \frac{\partial}{\partial x_j} (2\mu \langle S \rangle_{ij} - \rho \langle u_i u_j \rangle), \quad (3.46)$$

with mean rate of strain given by $\langle S \rangle_{ij} = 1/2(\partial \langle U_i \rangle/\partial x_j + \partial \langle U_j \rangle/\partial x_i)$. In order to close the system of transport equations, an expression or model for the Reynolds stress tensor $-\rho \langle u_i u_j \rangle$ is required.

The *closure level* is defined by the type (algebraic or differential) and the number of auxiliary equations required to close the previous equations [127]. The most simple

⁶The extension to the compressible case will be briefly presented at the end of the section for case of the standard k - ε model.

approach is to approximate the unknown Reynolds stress by algebraic relations based on the flow field variable in combination with prescribed functional expressions. Consequently, these approaches are referred to as *algebraic* or *zero-equation models*, with mixing length hypothesis based models being the most prominent. To improve the prediction of turbulent flow properties and to account for history effects of the flow structures, the concept of *one-equation models* has been developed, where a transport equation for a characteristic turbulent property is solved. This approach dates back to Prandtl [96], who developed a model based on the kinetic energy of the turbulent fluctuation. While the addition of a transport equation leads to a more physical description of the turbulent flow, Prandtl's approach still required the *ad-hoc* specification of a turbulent length scale (see below), i.e. the model still was incomplete. By introducing transport equation for a second turbulence parameter ω which serves as a reciprocal time scale, Kolmogorov [56] introduced the first complete model of turbulence. Although not instantly successful due to the limited computational power, this approach laid the basis for the following alternative *two-equation models*. Here a transport equation for the turbulent kinetic energy and a second turbulent property is solved. Instead of modelling the τ_{ij} indirectly via characteristic turbulent quantities, Rotta [102] succeeded in deriving a plausible model equation for the Reynolds stress tensor. As the Reynolds stresses are directly modelled, models based on this approach are called *stress-transport models*. The modelling approach is usually termed *second-order closure* or *second-moment closures*. In the following a model hierarchy based on number of additional pdes is presented and the individual closure levels are discussed.

3.3.1 Linear eddy-viscosity models

The primary class of turbulence models is based on the linear eddy viscosity assumption or eddy viscosity approximation introduced by Boussinesq [13]. The fundamental assumption is that the turbulent stress tensor can be expressed in terms of the mean rate of strain analogue to the viscous stresses for Newtonian fluids $\sigma_{ij} = 2\mu S_{ij}$, except that the molecular viscosity is replaced by the eddy viscosity μ_T , i.e.

$$\tau_{ij} = -\rho \langle u_i u_j \rangle = 2\mu_T \langle S \rangle_{ij} - \frac{2}{3} \rho k \delta_{ij} \quad (3.47)$$

where k denotes the turbulent kinetic energy defined by the trace of the Reynolds stress tensor

$$k = \frac{1}{2} \langle u_i u_i \rangle. \quad (3.48)$$

The final term in equation (3.47) ensures the validity of the approximation for $i = j$. By means of the introduction of the eddy viscosity concept, the problem of turbulence modelling has been moved from determining the six tensor components τ_{ij} to finding an approximation for the scalar quantity $\mu_T = \rho\nu_T$. Introducing (3.47) into incompressible

RANS equations (3.45)– (3.46) leads to

$$\frac{D \langle u \rangle_i}{Dt} = \frac{\partial}{\partial x_i} \underbrace{\left(\frac{\langle p \rangle}{\rho} + \frac{2}{3} k \right)}_{\text{effective pressure}} + \frac{\partial}{\partial x_j} \left(2 \underbrace{(\nu + \nu_T)}_{\text{effective viscosity}} \langle S \rangle_{ij} \right). \quad (3.49)$$

The introduction of the Boussinesq approximation therefore leads to modelled equations which have essentially the same structure as *normal*, i.e. laminar, equations. This form is favourable from a practical point of view as the averaged equations thus reduce to a form which is easily manageable and integrable into numerical codes for laminar flows.

However, the fundamental assumption that there exists a proportionality between turbulent stresses and rate of strain, which is equivalent to the assumption that both are aligned, does not hold in general, see for instance [94]. While for simple shear flows the turbulent-viscosity hypothesis is reasonable, there are several classes of flows in which the hypothesis is known to fail; an extension of the linear approach of (3.47) is discussed at the end of this section.

Algebraic models

The most simple of all turbulence models are given by algebraic models, i.e. no additional partial differential equation needs to be solved. Based on the Boussinesq approximation, the Reynolds stress tensor is determined as the product of an eddy viscosity and the mean rate-of-strain tensor. For a simple shear flow, in which the mean velocity only depends on y coordinate, the Boussinesq approximation is given by

$$-\langle uv \rangle = \nu_T \frac{d \langle U \rangle}{dy}. \quad (3.50)$$

Based on dimensional analysis the eddy viscosity can be expressed as the product of a velocity scale v_m and a length scale ℓ_m :

$$\nu_T = v_m \ell_m. \quad (3.51)$$

Prandtl [95] introduced the term *mixing length* for ℓ_m , thus this modeling approach is referred to as the Prandtl-mixing length model. The velocity scale v_m is supposed to be given by

$$v_m = C \cdot \ell_m \left| \frac{d \langle U \rangle}{dy} \right|,$$

thus the kinematic eddy viscosity is given by

$$\nu_T = \ell_m^2 \left| \frac{d \langle U \rangle}{dy} \right|, \quad (3.52)$$

where the constant C is adsorbed in the specification or model for the mixing length ℓ_m . The formulation remains incomplete as the mixing length is different for each flow and

must be specified or known in advance to obtain a solution. For a number of fundamental flows it is possible to approximate the mixing length based on empirical relations, for instance boundary layer flows ($\ell_m \sim y$, where y is the wall distance) or free shear flows ($\ell_m \sim \delta$, with δ being the mixing layer width).

One-equation model

Based on the instantaneous and the Reynolds averaged Navier-Stokes equation, a transport equation for the Reynolds stresses τ_{ij} can be derived. A corresponding equation for the turbulent kinetic energy k is the obtained by taking the trace of the Reynolds stress equation, see equation (3.48).

$$\frac{\partial k}{\partial t} + \langle U_j \rangle \frac{\partial k}{\partial x_j} = \tau_{ij} \frac{\partial U_i}{\partial x_j} - \varepsilon + \frac{\partial}{\partial x_j} \left[\nu \frac{\partial k}{\partial x_j} - \frac{1}{2} \langle u'_i u'_i u'_j \rangle - \frac{1}{\rho} \langle p' u'_j \rangle \right] \quad (3.53)$$

The quantity ε is the dissipation, here defined as

$$\varepsilon = \nu \left\langle \frac{\partial u'_i}{\partial x_k} \frac{\partial u'_i}{\partial x_k} \right\rangle ; \quad (3.54)$$

differs from the classical definition used in the previous section; however the difference between these two is small and can be ignored [127].

The standard approximation to represent the turbulent transport of scalar quantities in a turbulent field is, in analogy to molecular transport processes, that of gradient diffusion. Modelling the pressure diffusion term and the turbulent transport term together, assuming a behaviour of gradient-transport process, leads to

$$\frac{1}{2} \langle u_i u_i u_j \rangle + \frac{1}{\rho} \langle p u_j \rangle = - \frac{\nu_T}{\sigma_k} \frac{\partial k}{\partial x_j}, \quad (3.55)$$

where σ_k is a closure coefficient. Based on dimensional reasoning, the dissipation rate can be modeled as

$$\varepsilon = C_D k^{3/2} / \ell, \quad (3.56)$$

which leads to the following expression for the kinematic eddy viscosity:

$$\nu_T = k^{1/2} \ell = C_D k^2 / \varepsilon. \quad (3.57)$$

The final modelled equation is given by

$$\frac{\partial k}{\partial t} + \langle U_j \rangle \frac{\partial k}{\partial x_j} = \mathcal{P} - \varepsilon - \frac{\partial}{\partial x_j} \left[\left(\nu + \frac{\nu_T}{\sigma_k} \right) \frac{\partial k}{\partial x_j} \right] \quad (3.58)$$

where \mathcal{P} denotes the turbulent production defined as

$$\mathcal{P} = \tau_{ij} \frac{\partial \langle u_i \rangle}{\partial x_j}. \quad (3.59)$$

This model approach has been derived independently by Kolmogorov [56] in 1942 and Prandtl [96] in 1945, and is therefore referred to as the Prandtl-Kolomgorov k -equation model.

Two-equation models

The previously discussed one-equation model still requires the *ad-hoc* specification of the distribution of the turbulent length scale ℓ . An alternative to the *ad-hoc* specification is to obtain the length scale from a *scale-providing* transport equation. The obtained models are referred to as two equation models which are closed in the sense that they do not require any additional input of field quantities (i.e. length scales) except for initial and boundary conditions [2].

A natural choice would be the application of a model equation for the length scale ℓ itself as proposed by Rotta [102]. However the actual choice for the scale-providing variable is rather arbitrary. The very first documented two-equation approach by Kolmogorov [56] employed the inverse of the turbulent time scale⁷, i.e. a turbulent frequency $\omega = 1/\tau_T = (k/\varepsilon)^{-1}$. Rotta [101] employed a model equation for the product $k\ell$ as closure approach.

The most widely used two-equation turbulence model, particularly for industrial applications, is based on the turbulent dissipation rate ε as the scale-providing variable. The fundamental relations leading to the derivation a model equation for ε have been originally been derived by Rotta [103]. However, the standard k - ε model is usually accounted to work of Launder and Spalding [58,59]. Based on the turbulent kinetic energy k and the turbulent dissipation rate ε the eddy viscosity can be expressed as

$$\nu_t = C_\mu \frac{k^{3/2}}{\varepsilon}, \quad (3.60)$$

where C_μ is a proportionality constant. In the characteristic velocity and time scales of equation 3.60 are given by $u' = \sqrt{k}$ and $\ell = k/\varepsilon$ respectively.

The exact transport equation for the turbulent dissipation rate ε is given by [127]:

$$\begin{aligned} \frac{\partial \varepsilon}{\partial t} + \langle U_j \rangle \frac{\partial \varepsilon}{\partial x_j} = & -2 \left[\left\langle \frac{\partial u_i}{\partial x_k} \frac{\partial u_j}{\partial x_k} \right\rangle \left\langle \frac{\partial u_k}{\partial x_i} \frac{\partial u_k}{\partial x_j} \right\rangle \right] \frac{\partial \langle U \rangle_i}{\partial x_j} - 2\nu \left\langle u_k \frac{\partial u_i}{\partial x_j} \right\rangle \frac{\partial^2 \langle U \rangle_i}{\partial x_k \partial x_j} \\ & - 2\nu \left\langle \frac{\partial u_i}{\partial x_k} \frac{\partial u_i}{\partial x_m} \frac{\partial u_k}{\partial x_m} \right\rangle - 2\nu^2 \left\langle \frac{\partial u_i}{\partial x_k \partial x_m} \frac{\partial u_i}{\partial x_m \partial x_k} \right\rangle \quad (3.61) \\ & + \frac{\partial}{\partial x_j} \left[\nu \frac{\partial \varepsilon}{\partial x_j} - \nu \left\langle u_j \frac{\partial u_i}{\partial x_m} \frac{\partial u_i}{\partial x_m} \right\rangle - 2\nu\rho \left\langle \frac{\partial p'}{\partial x_m} \frac{\partial u_j}{\partial x_m} \right\rangle \right]. \end{aligned}$$

In comparison to the exact equation for the turbulent kinetic energy the structure of eq. (3.61) is far more complicated involving double and triple correlation. Furthermore considering ε primarily as the energy-flow rate in the energy cascade, it is determined by the large scale structures, while eq. (3.61) represents processes in the dissipation range, i.e. the dissipation eddies [94,127]. Thus the transport equation for the dissipation rate is commonly considered as an empirical model equation which is only loosely coupled to the exact equation.

⁷Kolmogorov referred to ω as *specific dissipation rate*.

The modelled transport equation for the turbulent dissipation rate ε in the standard formulation [59] reads

$$\frac{\partial \varepsilon}{\partial t} + \langle u_j \rangle \frac{\partial \varepsilon}{\partial x_j} = \frac{\partial}{\partial x_j} \left[\left(\mu + \frac{\mu_T}{\sigma_\varepsilon} \right) \frac{\partial \varepsilon}{\partial x_j} \right] + C_{\varepsilon 1} \mathcal{P} \frac{\varepsilon}{k} - C_{\varepsilon 2} \frac{\varepsilon^2}{k} \quad (3.62)$$

with the constants given in table 3.1.

On basis of the Renormalisation Group Method (RNG) the k - ε equations have been derived from the Navier-Stokes equations [130]. In the RNG k - ε model an additional term in the ε equation appears which does not stem from the RNG analysis but represents an *ad hoc* modelling approach. However, except for that term the ε equations in the two models are identical, indicating that there is significant physical reasoning in the postulated transport equation for the turbulent dissipation rate.

The second most popular choice for the scale providing quantities is the aforementioned ω , primarily for aerodynamical applications. While the interpretation of ω is not unique, the most simple approach is to regard it as the ratio of ε to k [127], indicating a close relation to the k - ε approach. A combined k - ε and k - ω was proposed by Menter [77] employing the ω equation in the near wall region, and transforming it into the ε equation away from the wall.

3.3.2 Extensions

Reynolds stress and related models

Differential second moment closures or Reynolds stress models (RSM) are based on a direct modelling of Reynolds stresses, i.e. the transport equations for the Reynolds stresses $\langle u_i u_j \rangle$ are closed and solved. Thus the eddy-viscosity approximation, one of the major defects of the previously discussed modelling approach, is not needed. Although conceptually advantageous, the RSM have not yet gained widespread popularity, which can be accredited to modelling difficulties, numerical costs and instabilities, and only modest improvement compared to more simple approaches.

The $v'^2 - f$ model represents a simplified variant of the Reynolds stress modelling approach which allows for the consideration of non-local effects caused by anisotropy of the Reynolds stress tensor. The base version of the model has been developed by Durbin [30], which has subsequently been improved by the author and co-workers. Besides the evolution equation for k and ε , an additional transport equation for the scalar quantity v'^2 and for the elliptic operator f are solved. Physically the scalar v'^2 can be interpreted as wall normal Reynolds stress in the near wall region. That way the near wall anisotropy is being accounted for in the modelling approach, while f captures non-local effects. Based on Boussinesq approximation the turbulent viscosity is modelled via

$$\nu_T = C_\nu v'^2 \frac{k}{\varepsilon},$$

where $\sqrt{v'^2}$ represents the velocity scale. The transport equations for v'^2 reads

$$\frac{\partial v'^2}{\partial t} + \langle u_j \rangle \frac{\partial v'^2}{\partial x_j} + v'^2 \frac{\varepsilon}{k} = kf - \frac{\partial}{\partial x_j} \left[\left(\nu + \frac{\nu_T}{\sigma_\kappa} \right) \frac{\partial v'^2}{\partial x_j} \right],$$

and is based on the homogenous IP-model. The elliptic relaxation approach for the evolution equation for f is given by

$$\frac{k^3}{\varepsilon^2} \frac{\partial^2 f}{\partial x_j^2} - f = \frac{k}{\varepsilon} (C_1 - 1) \left(\frac{v'^2}{k} - \frac{2}{3} \right) - D_2 \frac{P_k}{k}$$

with $C_1 = 1.4$ and $D_2 = 0.3$. The model has some popularity in turbomachinery applications, especially in combination with transitional effects [110].

Non-linear eddy viscosity models

The idea of non-linear eddy viscosity model are related to the algebraic stress modelling (ASM) approach. The Boussinesq approximation can be considered as the leading terms in a Taylor series expansion of the Reynolds stresses in terms of the rate of strain S_{ij} and rotation tensors Ω_{ij} , the latter two given by

$$S_{ij} = \frac{1}{2} \left(\frac{\partial \tilde{u}_i}{\partial x_j} + \frac{\partial \tilde{u}_j}{\partial x_i} \right) \quad \text{and} \quad \Omega_{ij} = \frac{1}{2} \left(\frac{\partial \tilde{u}_i}{\partial x_j} - \frac{\partial \tilde{u}_j}{\partial x_i} \right).$$

The general form of the non-linear eddy viscosity models is given by

$$\tau_{ij} = \mathcal{F}(S_{ij}, \Omega_{ij}) = \sum_{n=1}^{10} G^{(n)} \mathcal{T}_{ij}^{(n)},$$

where the tensors $\mathcal{T}_{ij}^{(n)}$ are combinations of S_{ij} and Ω_{ij} , and the coefficients $G^{(n)}$ depend on the invariants S_{ii}^2 , Ω_{ii}^2 , S_{ii}^3 , $\Omega_{ij}^2 S_{ji}$, and $\Omega_{ij}^2 S_{ji}^2$ [93, 94]. Most popular for engineering applications so far have been cubic models, for example [23]. In the field on IC engine simulation however, a major advantage could not be established [64], but increased numerical efforts and stability problems have been reported.

Standard k - ε model for compressible flows

The previous section has been restricted to constant density flows. Based on a low- Ma number asymptotic analysis of the exact turbulent transport equations and an order of magnitude estimation for the individual terms El Tahry [31] derived a compressible formulation of the standard k - ε model. The corresponding transport equations read:

$$\frac{\partial \langle \rho \rangle k}{\partial t} + \frac{\partial \langle \rho \rangle k \tilde{u}_j}{\partial x_j} = \frac{\partial}{\partial x_j} \left(\left[\mu + \frac{\mu_T}{\sigma_k} \right] \frac{\partial k}{\partial x_j} \right) + \tau_{T,ij} \frac{\partial \tilde{u}_j}{\partial x_i} - \langle \rho \rangle \varepsilon, \quad (3.63)$$

| $C_{\varepsilon 1}$ | $C_{\varepsilon 2}$ | $C_{\varepsilon 3}$ | C_{μ} | σ_k | σ_{ε} |
|---------------------|---------------------|---------------------|-----------|------------|------------------------|
| 1.44 | 1.92 | -0.33 | 0.09 | 1.0 | 1.3 |

Table 3.1: Constants of the standard k - ε model.

$$\frac{\partial \langle \rho \rangle \varepsilon}{\partial t} + \frac{\partial \langle \rho \rangle \varepsilon \tilde{u}_j}{\partial x_j} = \frac{\partial}{\partial x_j} \left(\left[\mu + \frac{\mu_T}{\sigma_{\varepsilon}} \right] \frac{\partial \varepsilon}{\partial x_j} \right) + C_{\varepsilon 1} \mathcal{P} \frac{\varepsilon}{k} - C_{\varepsilon 2} \langle \rho \rangle \frac{\varepsilon^2}{k} + C_{\varepsilon 3} \langle \rho \rangle \varepsilon \frac{\partial \tilde{u}_j}{\partial x_j}. \quad (3.64)$$

The additional term $C_{\varepsilon 3} \langle \rho \rangle \varepsilon \frac{\partial \tilde{u}_j}{\partial x_j}$, which appears in the transport equation for the Favre-averaged turbulent dissipation rate 3.64, take the fluid compression into account. This term is effective only in compressible flows and has originally been introduced to account for effects of piston compression in reciprocating engines.

3.3.3 Closing remarks

Besides the continuity and momentum equations, for general compressible flows the transport equations for species and enthalpy, see 2.1, have to be considered. Applying the averaging procedure, section 3.2.3, leads to unclosed terms in the corresponding equations similar to the Reynolds stresses in the momentum equations, which describe the turbulent transport of the quantity considered. Usually these turbulent fluxes of the general form $\langle \rho \rangle \widetilde{u\phi}$ are analogously to the Boussinesq approximation for the Reynolds stresses modelled by means of a gradient flux approximation:

$$\langle \rho \rangle \widetilde{u\phi} = \Gamma_T \frac{\partial \phi}{\partial x},$$

where Γ_T denotes the turbulent diffusivity of the quantity ϕ . By introducing the turbulent Prandtl number $Pr_t = \nu_T / \Gamma_t$ the turbulent diffusivity is related to the turbulent viscosity ν_T in analogy to the laminar Pr number. It is usually assumed the the turbulent Pr -number is of order unity, i.e. $\mathcal{O}(Pr_t) \approx 1$.

3.4 Large Eddy Simulation

In order to understand the basic concepts of the large-eddy simulation technique recall the characteristic properties of turbulent flow as discussed in section 3.1:

- turbulent flows are always transient and three-dimensional;
- measurement signals from turbulent flows seem random and chaotic; nevertheless coherent structures occur;
- turbulent flows exhibit a non-linear, non-local, diffusive and dissipative character.

Based on the fundamental studies by Kolmogorov [54, 55], the energy cascade concept can be established. Here a turbulent flow field is considered as an ensemble of turbulent eddies of different sizes. The largest eddies have a size of the order of the flow geometry while the smallest eddies are limited by the Kolmogorov length scale η_k . Energy is added to the largest scales by means of velocity gradients. This energy is transferred to eddies of smaller and smaller sizes in a cascading process. This process describes barely the net-energy balance, as the inverse transfer from smaller to larger elements, i.e. *backscatter effects*, can locally occur. The energy is eventually dissipated by viscous effects by eddies of size of the Kolmogorov length scale.

While large scale structures are directly affected by the (flow) geometry, the turbulence on the small scale is due to the cascading process and the related non-linear effects virtually universal. Furthermore, the small scale turbulence can approximately be considered as being locally isotropic, which implies that their statistical properties are independent of a transformation of the frame of reference and, even more important, independent of the large scale structures. Experimental studies of high Reynolds number flows support this theory, see for instance the collection provided in [104]. Note however that the concise picture of the energy cascade refers to the *net energy transfer only*, and especially the interaction between large and small scale structures is neglected.

| large scale structures | small scale structures |
|--|---|
| <ul style="list-style-type: none"> • created by mean flow • depend on boundary and specific geometrical conditions of the flow problem • display coherent structures • non-homogeneous and anisotropic • long-lasting, energy-containing • diffusive | <ul style="list-style-type: none"> • stem from large scale structures • universal • random, stochastic • (almost) homogeneous, isotropic • short-lived, energy-depleted • dissipative |
| → difficult to model | → more simple to model |
| → universal model <i>not</i> possible | → universal model more likely |

Table 3.2: Comparison of the characteristic properties of large and small scale structures in a turbulent flows [15].

Table 3.2 summarises the characteristic properties of turbulent flows with respect to large and small scale motions. Using a RANS modelling approach all scales of a turbulent flow field must be modelled by an appropriate (statistical) turbulence model. Due to the characteristics of the large scales, and here especially their dependence on the flow problem under consideration, it is doubtful whether a general model is feasible. On the other hand, a direct numerical simulation, i.e. a direct solution of all turbulent scales without the need for modelling, is restricted by the Reynolds number limit, see section 3.1.

Based on the assumption of isotropy of the small scales, the Large Eddy Simulation approach can be summarised as follows:

- directly simulate the motion of the large scales (the *large eddies*)
- while the small scale structures are modelled.

The advantage of the LES approach is based on the assumption of the isotropy of the small scales. As the large scale are directly computed only a part of the turbulent spectrum requires modelling. Due to the characteristic properties of the smallest scale the modelling process can be expected to be much easier. This is reflected by the fact that LES models employed today are simple viscosity models⁸. In comparison to DNS, the LES approach avoids the vast computational cost of explicitly representing the small-scale motions; therefore the computational restriction to low-Reynolds number flows is eased.

The realisation of the LES approach is based on a decomposition of the turbulent flow field into large and small scales. Formally, this scale separation is performed by means of a filtering operation [61]. Ideally the scale separation takes place in the inertial range of the turbulent spectra, thus allowing a clear-cut partition between energy-containing and dissipative scales. Note however that the existence of a distinct inertial range is only guaranteed at sufficiently high Reynolds numbers

Conceptually in LES there are four distinct steps which will be discussed in the following sections:

1. a filtering operation to decompose the turbulent field into a resolved and a residual component; the resolved velocity field – which is three-dimensional and time-dependent – represents the motion of the large eddies;
2. the equation for the evolution of the filtered quantities are derived from the instantaneous conservation equations; these filtered equations have/are of the same form as the standard equations but, similar to the RANS equation, contain an additional term arising from the residual motion;
3. the filtered equation are closed by modelling the residual stress tensor (in case of the momentum equations);
4. supplied by appropriate initial and boundary conditions the model filtered equations are solved numerically, leading to an approximation to the large-scale motions in a single realisation of the turbulent flow.

⁸*Simple* refers here to the fundamental form of the modelling approach with additional transport equation being considered as more complex.

3.4.1 Filtering

Formally similar to the RANS averaging procedure, each instantaneous flow variable $\phi(\mathbf{x}, t)$ is decomposed into a resolved, large scale part $\overline{\phi(\mathbf{x}, t)}$ and a non-resolved, small scale part $\phi'(\mathbf{x}, t)$. In contrast to a statistical approach, in LES a spatial (in physical space) or low-pass (in spectral space) filtering operation is performed. This filtering is mathematically represented in physical space as a convolution product.

The resolved part of filter-scale part $\overline{\phi(\mathbf{x}, t)}$ of a space-time variable $\phi(\mathbf{x}, t)$ is defined formally by the the convolution product

$$\overline{\phi(\mathbf{x}, t)} = \int_{-\infty}^{+\infty} \int \phi(\xi, t') G(\mathbf{x} - \xi, t - t') dt' d^3\xi, \quad (3.65)$$

in which the convolution kernel G is characteristic of the filter used, which is associated with the cutoff scales in space and time, $\overline{\Delta}$ and $\overline{\tau}_c$, respectively. This relation is denoted symbolically by

$$\overline{\phi} = G \star \phi. \quad (3.66)$$

The corresponding definition in the Fourier or spectral space is given by

$$\widehat{\overline{\phi}}(\mathbf{k}, \omega) = \widehat{\phi}(\mathbf{k}, \omega) \widehat{G}(\mathbf{k}, \omega), \quad (3.67)$$

where \mathbf{k} and ω are the spatial wave number vector and time frequency respectively. The function \widehat{G} is the transfer function associated with the kernel G . The spatial cutoff length $\overline{\Delta}$ is associated with the cutoff wave number k_c via $k_c = \pi/\overline{\Delta}$, and the time $\overline{\tau}_c$ with the cutoff frequency ω_c . The unresolved part of $\phi(\mathbf{x}, t)$, denoted by $\phi'(\mathbf{x}, t)$ is defined operationally by

$$\phi'(\mathbf{x}, t) = \phi(\mathbf{x}, t) - \overline{\phi(\mathbf{x}, t)} \quad (3.68)$$

$$= \phi(\mathbf{x}, t) - \int_{-\infty}^{+\infty} \int \phi(\xi, t') G(\mathbf{x} - \xi, t - t') dt' d^3\xi, \quad (3.69)$$

or equivalently in compact symbolic notation

$$\phi'(\mathbf{x}, t) = (1 - G) \star \phi; \quad (3.70)$$

the corresponding form in spectral space is given by

$$\widehat{\phi}'(\mathbf{k}, \omega) = \widehat{\phi}(\mathbf{k}, \omega) - \widehat{\overline{\phi}}(\mathbf{k}, \omega) \quad (3.71)$$

$$= \left(1 - \widehat{G}(\mathbf{k}, \omega)\right) \widehat{\phi}(\mathbf{k}, \omega). \quad (3.72)$$

In the LES literature it is common to refer to ϕ' as *sub-grid* quantity, which indicates the close coupling of the filter operation to the numerical grid. Instead of this misleading term, in the following the more exact term *sub-filter* quantity is employed, as ϕ represents the part of ϕ being removed by the filter operation.

The filter function G in the definition of the resolved part $\bar{\phi}$, (3.65), has yet not been specified. In order to be able to manipulate the Navier-Stokes equations after applying a filter to obtain transport equations for the resolved part of the flow field, the filter has to verify the following properties [105]:

1. Conservation of constants, which is equivalent to the requirement, that the filter kernel is normalised:

$$\bar{a} = a \quad \Leftrightarrow \quad G \star 1 = 1 \quad (3.73)$$

the property is of fundamental importance, as only for a normalised filter kernel the conservation properties of the governing, unfiltered equations are retained;

2. linearity, which is automatically satisfied by filters of convolution type, as products of convolution verifies this condition independently of the filter kernel G :

$$\overline{\phi + \psi} = \bar{\phi} + \bar{\psi} \quad (3.74)$$

3. commutation with derivation

$$\frac{\partial \bar{\phi}}{\partial s} = \bar{\frac{\partial \phi}{\partial s}} \quad s = \mathbf{x}, t. \quad (3.75)$$

The filters that verify these properties are not, in the general case, Reynolds operators (see section 3.2), i.e.

$$\bar{\bar{\phi}} = G \star G \star \phi = G^2 \star \phi \neq \bar{\phi} = G \star \phi, \quad (3.76)$$

$$\bar{\phi'} = G \star (1 - G) \star \phi \neq 0, \quad (3.77)$$

A final important property of the filter kernel G is given in the limit of vanishing filter width $\bar{\Delta} \rightarrow 0$. In this situation the filtered variable $\bar{\phi}$ has to tend towards the un-filtered value ϕ .

$$\lim_{\Delta \rightarrow 0} \bar{\phi}(\mathbf{x}, t) = \phi(\mathbf{x}, t) \quad (3.78)$$

This property implies that for $\Delta \rightarrow 0$ also the sub-filter variable ϕ' tends towards zero, see (3.68), and the un-filtered variable is reobtained.

The classical convolution filters which are usually employed in LES for performing the spatial scale separation with their corresponding transfer functions in spectral space are given in table 3.3. Namely, these are the box or top-hat filter, the Gaussian filter⁹, and the spectral or sharp cut-off filter. A graphical representation of convolution kernels G and the transfer function \hat{G} is given in figure 3.3. The most common filter is the box

| | filter function $G(r)$ | transfer function $\widehat{G}(k)$ |
|----------------------------------|---|--|
| box or top-hat filter | $\frac{1}{\Delta} H(\frac{1}{2}\bar{\Delta} - \mathbf{r})$ | $\frac{\sin(k\bar{\Delta}/2)}{k\bar{\Delta}/2}$ |
| Gaussian filter | $\left(\frac{\gamma}{\pi\bar{\Delta}^2}\right)^{1/2} \exp\left(\frac{-\gamma \mathbf{r} ^2}{\bar{\Delta}^2}\right)$ | $\exp\left(\frac{-\bar{\Delta}^2 k^2}{4\gamma}\right)$ |
| spectral or sharp cut-off filter | $\frac{\sin(k_c \mathbf{r})}{k_c \mathbf{r}}$, with $k_c = \frac{\pi}{\Delta}$ | $H(k - k_c)$ |

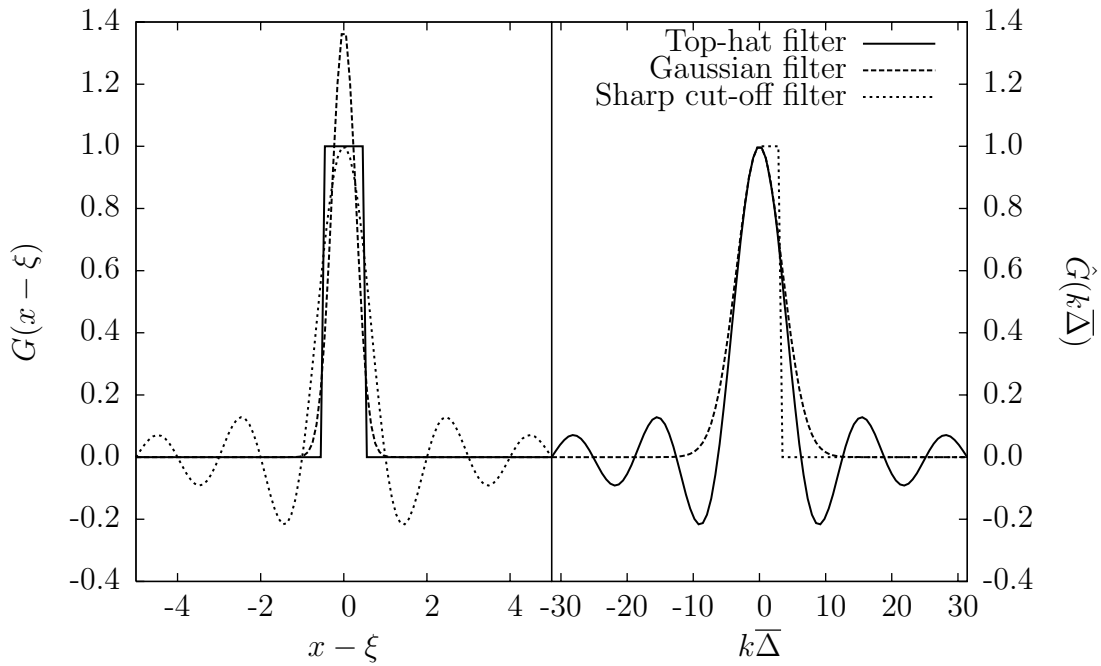
Table 3.3: Classical filter and transfer functions; $\mathbf{r} = \mathbf{x} - \xi$.

Figure 3.3: Filter and transfer function for the three classical LES filter.

filter which represents a local, spatial averaging. This filter is implicitly used in (low order) finite volume discretisation, where an integration over a computational cell leads to a filtered representation of the field variables. The spectral cut-off filter eliminates all Fourier coefficients belonging to wave numbers above a cut-off, thus performing a strict separation of resolved and unresolved scales.

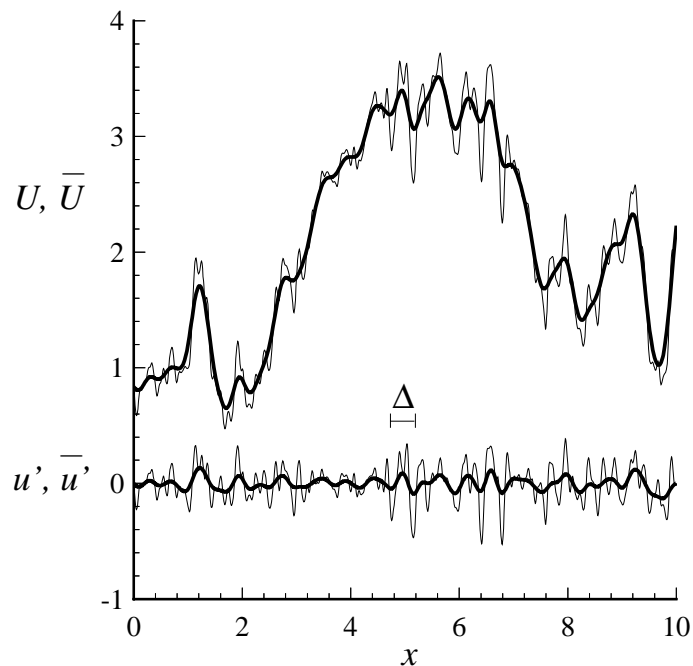


Figure 3.4: Sample of the velocity field $U(x)$ and the corresponding filtered field $\bar{U}(x)$ (bold line), using a Gaussian filter with $\Delta \approx 0.35$; additionally shown is the residual field $u'(x)$ and the filtered residual field $\bar{u}'(x)$ (bold line) at the bottom; taken from [94].

Apart from integral filters previously discussed, it is possible to apply other techniques in order to smooth the solution; amongst these are for example differential filter or higher order filter. Details can be found in [39], [105].

In the previous discussion it was implicitly assumed that the filter is homogenous and isotropic. For practical applications these assumptions are too restrictive. Furthermore the variation of the filter cut-off length (filter width) is desirable with respect to the ability to adopt the filtering operation to the (local) structure of the solution. Employing non-uniform filters, it cannot be assured that filtering and derivation commute, i.e.

$$\frac{\partial \bar{\phi}}{\partial s} \neq \bar{\frac{\partial \phi}{\partial s}}.$$

⁹Usually, γ is generally taken to be equal to 6.

The application of non-uniform filters to the conservation equation gives rise to a number of additional closure terms which are referred to in literature as *commutation errors*. By employing a modified formulation of the filter, Ghosal and Moin [40] demonstrated that the commutation error is of second order, $\mathcal{O}(\overline{\Delta}^2)$. Considering the case that the solution of the filtered transport equation is done by means of numerical schemes of second order, which is the case for most engineering applications, the commutation error and the numerical discretisation error are of same order and can therefore be neglected.

In numerical simulations the filter length $\overline{\Delta}$ is assumed to be proportional to the grid spacing Δ_x :

$$\overline{\Delta} = \beta \cdot \Delta_x. \quad (3.79)$$

The mesh length scale Δ_x is usually based on the volume of a mesh cell [39]:

$$\Delta_x = (\Delta V)^{1/3} \quad (3.80)$$

For the simulation of turbulent channel flow, Bardina *et al* [6] suggested the following expression:

$$\Delta_x = (\Delta x^2 + \Delta y^2 + \Delta z^2)^{1/2} \quad (3.81)$$

Finally, a more conservative approach is to use the maximum length scale of the computational cell:

$$\Delta_x = \max(\Delta x, \Delta y, \Delta z) \quad (3.82)$$

The latter options are practical only for Cartesian meshes, or for curvilinear grid employing appropriate transformations of the grid spacings. In general, considering practical applications demanding unstructured meshes, equation (3.80) presents the only feasible solution.

By linking the filter width and the grid spacing, grid dependency is implied by definition. As the mesh length scale and correspondingly the filter width are local quantities the structures which can be resolved are directly linked to the mesh properties of a certain region. For uniform meshes the smallest resolvable structures are of the order to two cell sizes which gives a lower limit for the constant β of equation (3.79); a more thorough analysis [20] shows that generally the proportionality constant β is of order $\mathcal{O}(\beta) = 2 \dots 4$. However if due to low order numerical schemes the amount of numerical dissipation introduced is significant, the value of β needs to be increased to compensate these effects.

3.4.2 Filtered transport equations

In analogy to the derivation of the Reynolds averaged Navier-Stokes equations, section 3.2.3, a filter is applied to the general conservation equations for obtaining a transport equation for the filtered quantities. Considering the generalized form $\frac{\partial \phi}{\partial t} = F(\phi, \mathbf{x}, t)$ with F representing convection, diffusion, and source terms, the filtering operation is

motivated via the symbolic filtering notation, cf. (3.66), and the application of the differential operator, leading to

$$\bar{\phi} = G \star \phi \quad \Rightarrow \quad \frac{\partial \bar{\phi}}{\partial t} = \frac{\partial G \star \phi}{\partial t} = G \star \frac{\partial \phi}{\partial t} = G \star F(\phi, \mathbf{x}, t),$$

where it is assumed that differentiation and filtering commute.

Applying the filter G to the momentum equations and assuming commutation with the derivative, leads to the transport equation for the filtered velocity \bar{u}_i . As in the statistical approach, the filtering of the non-linear convective term leads to the appearance of an unclosed term, namely $\overline{u_i u_j}$. Recall that in contrast to the RANS averaging approach $\overline{\phi'} \neq 0$ and $\overline{\bar{\phi}} \neq \bar{\phi}$. Employing the Leonard or triple decomposition of the filtered non-linear term allows the definition of the sub-filter stress $\bar{\tau}_{ij}$

$$\overline{u_i u_j} = \overline{(\bar{u}_i + u'_i)(\bar{u}_j + u'_j)} \quad (3.83)$$

$$= \overline{\bar{u}_i \bar{u}_j} + \underbrace{\overline{\bar{u}_i u'_j} + \overline{\bar{u}_j u'_i}}_{\mathcal{C}_{ij}} + \underbrace{\overline{u'_i u'_j}}_{\mathcal{R}_{ij}} \quad (3.84)$$

$$= \overline{\bar{u}_i \bar{u}_j} + \underbrace{\overline{\bar{u}_i \bar{u}_j} - \overline{\bar{u}_i \bar{u}_j}}_{\mathcal{L}_{ij}} + \underbrace{\overline{\bar{u}_i u'_j} + \overline{\bar{u}_j u'_i}}_{\mathcal{C}_{ij}} + \underbrace{\overline{u'_i u'_j}}_{\mathcal{R}_{ij}}, \quad (3.85)$$

$\underbrace{\hspace{10em}}_{\bar{\tau}_{ij}}$

where \mathcal{L}_{ij} denotes the Leonard tensor, \mathcal{C}_{ij} the cross stress tensor, and \mathcal{R}_{ij} the Reynolds sub-filter stress tensor. The Leonard stresses describe the interaction between large scale motions (eddies) generating small scale turbulence. The interaction between large and small scales is represented by the cross stress tensor \mathcal{C}_{ij} . This term is responsible for energy transfer between the scales in both directions, i.e. from large to small scale (energy cascade) but also vice versa from small to large scale, usually referred to as (*backscatter*), with a mean transfer towards the smaller structures. The last term \mathcal{R}_{ij} , the sub-filter Reynolds stress tensor, reflects the interactions between the small scale motions, generating large scale turbulence. Just as the cross stress tensor, \mathcal{R}_{ij} is involved in backscatter effects.

For compressible flows, a *mass-weighted* or Favre filter is introduced for analogue reasons as in the RANS context, see equation (3.23):

$$\tilde{\phi} = \frac{\overline{\rho \phi}}{\bar{\rho}} = \frac{G \star (\rho \phi)}{G \star \rho} = G_\rho \star \phi, \quad (3.86)$$

where G_ρ denotes the Favre filter operator corresponding to the filter G ; for simplicity the same notations as in the RANS case are employed here, but in the present section, the $\tilde{\cdot}$ denotes Favre *filtering* instead of (statistical) averaging. The turbulent residual or sub-filter stress tensor thus reads [78]

$$\bar{\rho} \tilde{\tau}_{ij} = \bar{\rho} \widetilde{u_i u_j} - \bar{\rho} \tilde{u}_i \tilde{u}_j = \bar{\rho} (\mathcal{L}_{ij} + \mathcal{C}_{ij} + \mathcal{R}_{ij}) \quad (3.87)$$

The final filtered equation have the same form as the statistically averaged RANS equation with the averaging operator $\langle \cdot \rangle$ replaced by the filter operator $\bar{\cdot}$; therefore they are omitted here for brevity.

3.4.3 Sub-Filter Scale Models

Analogous to the Reynolds stresses the sub-filter stresses τ_{ij} require modelling. In LES a length scale is already given by the filter width. Sub-filter turbulence can be assumed to be rather isotropic therefore the models can be much simpler. Usually the solution of an additional pde is avoided, and algebraic relations based on mean field quantities are more popular. Thus a model hierarchy based on additional pde's as in the RANS case does not exist for the LES modelling approach.

Similar to the discussion of RANS turbulence models in section 3.3, the following will focus on incompressible flows; the extension to compressible flows is straight forward. Additionally mainly eddy viscosity approaches are considered representing the majority of sub-filter models, which is reasonable due to the fundamental modelling assumption of local isotropy. Thus the sub-filter stress tensor is modelled analogous to the Boussinesq assumption as

$$\tau_{ij} = -2\mu_t \bar{S}_{ij}, \quad (3.88)$$

where \bar{S}_{ij} is the filtered rate-of-strain tensor $\bar{S}_{ij} = 1/2(\partial \bar{u}_i / \partial x_j + \partial \bar{u}_j / \partial x_i)$.

Smagorinsky model and variants

The earliest published LES model dates back to the work of Smagorinsky [111] in the early 1960s. Due to its simplicity it is still the most widely used LES model and forms the basis for a large class of modelling approaches. The classical or constant coefficient Smagorinsky model employs a mixing-length approach similar to the mixing-length model by Prandtl [95] for the description of the sub-filter scale viscosity, i.e.

$$\mu_t = \bar{\rho} l_s u_s, \quad (3.89)$$

where l_s is the Smagorinsky length scale and u_s the corresponding velocity scale. The length scale correlates to filter width which separates the large and the small scale structures, thus

$$l_s = C_s \bar{\Delta}, \quad (3.90)$$

where C_s is the Smagorinsky coefficient. The velocity scale is related to the filtered rate-of-strain via

$$u_s = l_s \bar{S} = C_s \bar{\Delta} (2 S_{ij} S_{ij})^{1/2}. \quad (3.91)$$

Combining the previous equations finally leads to

$$\mu_t = \bar{\rho} (C_s \bar{\Delta})^2 \bar{S} \quad (3.92)$$

The Smagorinsky coefficient C_s is a free parameter which needs to be adjusted to the flow configuration under consideration. For simple geometries values between 0.1 (turbulent mixing layer) and 0.25 (turbulent channel flow) are commonly used. For homogeneous, isotropic turbulence Lilly [65] derived an approximation for C_s based on the Kolomogorov energy spectrum as

$$C_s = \frac{1}{\pi} \left(\frac{2}{3\alpha_k} \right)^{3/4} \approx 0.165,$$

where a value of Kolomogorov constant $\alpha_k = 1.6$ has been used.

Besides the necessity to adjust the Smagorinsky coefficient, the correlation of the turbulent stresses as modelled by the Smagorinsky model to DNS data is usually poor. Additionally, the model is not capable of describing backscatter effects. Nevertheless it still represents the most popular LES model, which can be accounted to its simplicity, ease of implementation, and numerical stability.

In order to overcome the problem of tuning the Smagorinsky coefficient, Germano *et al* [37] proposed a dynamic procedure for determining the value of the model parameter. The basic idea of the procedure is to estimate the sub-filter quantities on basis of the smallest resolved scales. By applying an additional test filter \tilde{G} , being wider than the grid-scale filter G , an explicit relation between the sub-test-filter stresses, which can be computed from the resolved field, and the sub-filter stress can be derived; this relation is usually referred to as the *Germano identity*. This relation then allows to derive an equation for determining a local value of the Smagorinsky parameter. While the dynamic procedure has first been applied to the Smagorinsky model, the general algorithm is applicable for any type of model. The dynamic Smagorinsky model, i.e. the Smagorinsky model with a dynamic determination of the model parameter, can currently be regarded as the standard model in most LES applications of moderate complexity.

Structure-function model

Chollet and Lesieur [19] developed an eddy-viscosity model in spectral space based on theoretical studies on three-dimensional, isotropic turbulence. Here the eddy-viscosity is expressed in terms of the energy spectra in the region of the cut-off wave length. The transfer of this model to physical space is based on the second order structure function as defined by

$$F_2 = \langle ||\bar{u}_i(x_i, t) - \bar{u}_i(x_i - r_i, t)||^2 \rangle_{||r_i||=\bar{\Delta}}. \quad (3.93)$$

Here $||\cdot||$ denotes the norm of the vector, $\langle \cdot \rangle$ spacial averaging, $\bar{\Delta}$ the distance between two grid points, and r_i the distance vector. The final relation for the sub-filter eddy viscosity then reads

$$\nu_t = C_{SF} \alpha_K \bar{\Delta} F_2^{1/2}, \quad (3.94)$$

with $C_{SF} = 0.105$, and α_K being the Kolmogorov constant. A number of enhancements of the model have been developed in order to improve the behaviour in the near wall region and during transition processes. In the selective structure function (SSF) model

[63] the eddy-viscosity is deactivated in regions, where the flow is not three-dimensional enough, based on the angle between the vorticity vector at a node and the average value over the neighbouring nodes of the computational mesh. The filtered structure function (FSF) model [29, 63] applies a high-pass filter to the resolved field before the structure function is evaluated.

Bardina similarity model

The fundamental task of the sub-filter scale model is to establish a relationship between the large and the small scales. Bardina *et al* [6] assumed that the structures of the small and the large scales near the spectral cut-off, i.e. the smallest resolved and the largest non-resolved structures, are similar. The smallest resolved structures can be recovered by means of an additional filtering operation, allowing to approximate the sub-filter stress tensor as

$$\tau_{ij} = C_b(\overline{u_i u_j} - \overline{\overline{u_i} \overline{u_j}}). \quad (3.95)$$

The correlation of the modelled sub-filter stresses to DNS data showed an excellent agreement. Additionally, the model approach naturally accounts for backscatter effects. Unfortunately the model shows only a very weak energy dissipation, making it numerically unstable. Therefore it is commonly combined with a more-dissipative, for example the Smagorinsky model. These *mixed models* have the form

$$\tau_{ij} = \underbrace{C_b(\overline{u_i u_j} - \overline{\overline{u_i} \overline{u_j}})}_{\text{Bardina}} - \underbrace{2(C_s \Delta)^2 \overline{S} \overline{S}_{ij}}_{\text{Smagorinsky}}. \quad (3.96)$$

Approximate inverse modelling

The so-called inverse modelling approach [38] or approximate deconvolution method [120] is based on the inversion of the filter operation. Thus the turbulent stress tensor can be directly approximated using the filtered field. Usually, the filter cannot be directly inverted, thus an approximation of the inverse filter is required. Different approaches exist for the formal inversion of the filter G , see [39] for an more detailed overview of the topic.

The main drawback of the approach lies in the demands on the numerical schemes as high-order schemes are required, which makes the realisation of the approach difficult for practical applications. Furthermore the inversion of the convolution filter operation (*deconvolution*) is badly conditioned [15], so that Speziale [118] questions the realisability of the inverse filtering approach for complex turbulent flows.

One equation eddy viscosity model

Most modelling approaches for LES focus an algebraic relations or functional expressions for the determination of the sub-filter stress tensor. The focus of present reasearch ac-

tivities focuses much more on dynamic and scale-similarity modelling which is motivated by the local character of the filtering operation.

Employing an eddy-viscosity type approach for the approximation of the sub-filter stress tensor, a length and a velocity scale is required, see equation (3.89). While the length scale is given by the filter length, (3.90), the definition of the velocity scale is not unique. The approach followed by the Smagorinsky model, in which the velocity scale is obtained on basis of $\bar{\Delta}$ and the resolved strain-rate \bar{S}_{ij} , (3.91), is strictly valid only in the limit that production and dissipation of energy in the sub-filter scale are in equilibrium [74]. The implication of this requirement is that the filter cut-off is situated in the dissipation scale of the turbulent spectrum, which poses severe restrictions on the required mesh resolution and makes it actually impractical for flows at higher *Re*-numbers. Alternatively the velocity scale can in analogy to RANS modelling be determined on basis of the sub-filter kinetic energy, as suggested by Schumann [108].

A model that uses a transport equation for the kinetic energy of the sub-filter mode given by

$$k_r = q_{sgs}^2 = \frac{1}{2} \overline{u'_i u'_i} \quad (3.97)$$

has been developed independently by a number of authors. Following the formulation by [131], the modelled evolution equation for k_r reads

$$\frac{\partial k_r}{\partial t} + \frac{\partial}{\partial x_j} (\bar{u}_j k_r) = \frac{\partial}{\partial x_j} \left[(\nu + \nu_t) \frac{\partial k_r}{\partial x_j} \right] + \mathcal{P}_r - C_\varepsilon \frac{k_r^{3/2}}{\bar{\Delta}} \quad (3.98)$$

with

$$\nu_t = C_k \bar{\Delta} k_r^{1/2}, \quad \mathcal{P}_r = 2\nu_t \bar{S}_{ij} \bar{S}_{ij}.$$

The model coefficients C_k and C_ε have been determined as $C_k = 0.1$ and $C_\varepsilon = 1.0$. Instead of prescribing the values of the model coefficient, a localized dynamic approach can be applied [75].

The derivation of the k_r -equation is similar to its RANS counterpart, the Prandtl-Kolmogorov k -equation. Note that in the dissipation term, the integral length scale is replaced by the filter width, which leads to a simple algebraic expression for the sub-filter dissipation:

$$\varepsilon_r = C_\varepsilon \frac{k_r^{3/2}}{\bar{\Delta}}.$$

While most of the LES models explicitly avoid to introduce an additional transport equation due to the filtering operation being local in space, the employment of the k_r -equation might have a number of practical advantages from an IC engine simulation point-of-view. The modelling approach eases the mesh requirement as the filter cut-off, which is here assumed to be directly connected to the mesh spacing, can be allowed to be inside the inertial range, but not necessarily inside the dissipation range. Based on the local value of k_r , the sub-filter turbulence intensity needed for sub-filter mixing

and combustion modelling can easily be obtained. The transport of an additional sub-filter quantity might have advantages for grid movement where interpolation is necessary during the course of the simulation. In this case the sub-filter information is transported via an additional scalar quantity and not extracted from the resolved velocity field, which is difficult to be transferred undisturbed from one mesh to another [113].

3.5 Hybrid modelling

The grid resolution requirements for an LES, especially for the LES of wall bounded flows, are significantly higher than those for a RANS simulation of the same flow configuration as considerably smaller length scales and flow structures are resolved. Additionally the numerical requirements are rather restrictive considering practical applications, leading to uncertainties in the interpretation of the numerical result; thus the question arises whether the observed *turbulence* is physical or just a result of numerical instabilities. On the other hand, the mesh resolution in wall distant regions is usually sufficient for resolving a significant amount of the turbulent spectrum.

In order to reduce the cost a feasible solution is to combine LES with another technique which provides the relevant low-frequency solution at low costs. A natural choice is to use a hybrid combination of a RANS approach, for example in attached boundary layer regions, coupled to an LES model. This hybrid approach, first introduced by Spalart *et al* for the simulation of airfoils [115], has become more and more popular in recent years allowing the simulation of high-*Re* number flows and in complex geometries, which are (yet) not feasible with pure LES. The potential of the approach can be seen by an analysis on Hanjalic *et al* [46], who studied the usage of a hybrid model for a channel flow simulation; here the hybrid model required only 1% of the cells which are needed for a corresponding LES. An earlier estimation by Spalart *et al* [115] for the simulation of an airliner wing lead to the conclusion that an LES might be feasible in four decades while the hybrid approach employable today.

For LES the near wall region requires a significantly higher mesh resolution, almost similar to DNS, in order to capture the anisotropy of the turbulent flow structures. Hybrid modelling usually employs the RANS submode in this region, allowing the usage of standard wall function approaches. For wall bounded flows the problem of wall modelling is avoided, which actually is still one of the major topics of LES modelling today.

3.5.1 Overview of hybrid modelling approaches

Two main modelling approaches can be distinguished [46, 105] for combining RANS and LES, namely the zonal decomposition and the universal modelling.

The zonal decomposition divides the computational domain into pre-defined sub-domains and applies the corresponding model to the particular zone. The grid resolution in the domains can be adjusted to the model, even the suppression of one or two spatial dimensions in RANS sub-domains is feasible. While the decomposition allows for an

explicit specification of the model in each domain, this also requires pre-knowledge of the flow structures. Additionally, in [46] a great sensitivity of the results to the location of the interfaces is reported. For complex or changing geometries, this behaviour makes the application very difficult.

In the case of universal modelling, a generalised turbulence model defined as a combination of a RANS and a typical sub-filter model is employed. The combination of the two models is expected to introduce more physics into the sub-filter model in regions where the filter cut-off is located in the low frequency part of the spectrum, outside or at the beginning of the inertial range, i.e. in regions where the modellings assumptions of LES are not valid. The mode of the model (RANS, LES, blended) is determined via predefined, model-specific local criteria like mesh resolution or wall distance.

Detached eddy simulation

The most successful hybrid model so far has been proposed by Spalart *et al* [115], termed *Detached Eddy Simulation* or *DES*. The original version started from the Spalart-Allmaras RANS one-equation model [114] as sub-filter model with a slight modification of the destruction term, incorporating the filter size as an additional parameter. The fundamental idea is to employ the RANS based model in attached boundary layers, while in detached regions transient effects are resolved via an LES approach¹⁰. An extension of the approach has been performed by Strelets [121] starting from the two-equation model by Menter [76]; a more detailed discussion of the two model approaches can be found in [113].

Willems two-scale method

Willems [128] proposed in 1996 an approach which is based on the so-called two-scale approach. The transport equations for all flow quantities are solved at the filter scale $\overline{\Delta}$, while the equation for the turbulent kinetic energy and turbulent dissipation rate are solved at the integral scales ℓ_t , and then down-scaled to the filter scale. As the ε is scale invariant, the dissipation rate at the integral length scale is equal to the dissipation at the filter level. Based on isotropic scaling relations the turbulent kinetic energy at the filter level k_f reads:

$$k_f = k_t \left(\frac{\overline{\Delta}}{\ell_t} \right)^{2/3} \quad (3.99)$$

with k_t being the solution on the integral scales. Note that equation (3.99) is only valid for $\frac{\overline{\Delta}}{\ell_t} < 1$, i.e. if the filter width is smaller than the integral length scale. As the filter width and the mesh spacing are tightly coupled, see equation (3.90), this implies that the scaling can only be performed if the mesh is fine enough to resolve structures of

¹⁰Note: the RANS model has been developed specifically for the simulation of airfoils.

the size of the integral length scale. On coarser meshes the pure RANS formulation is retained, leading to the following formulation for the turbulent eddy viscosity:

$$\nu_t = \nu_T(1 - f(\bar{\Delta}, \ell_t))^2 \quad \text{with} \quad f(\bar{\Delta}, \ell_t) = \min \left[0.0, 1.0 - \left(\frac{\bar{\Delta}}{\ell_t} \right)^{2/3} \right]. \quad (3.100)$$

where ν_T refers to the RANS based viscosity, $\nu_T = c_\nu k^2/\varepsilon$. Independently Magnient [69] arrived in 2001 independently at the same model; also LNS (Limited Numerical Scales) approach shows strong similarities to the Willems model. The modelling approach by Willems has two interesting limits. For very small filter sizes, $\bar{\Delta} \rightarrow 0$, the sub-filter viscosity tends to zero and the solution corresponds to a DNS. In the opposite limit of large filter width, the model leads to the RANS solution with $\nu_t = \nu_T$.

Speciale's rescaling and the LNS methods

Similar to the approach followed by Willems, Speziale [118, 119] proposed a general rescaling function for the turbulent stresses of the form

$$\bar{\tau}_{ij} = \mathcal{F} \cdot \tau_{ij},$$

where the scaling function \mathcal{F} depends on the ratio of the filter width and the Kolmogorov length scale. The turbulent stress τ_{ij} stems from the solution of an arbitrary RANS model, which should be able to deal with anisotropy and disequilibrium, such as Reynolds stress models. The scaling function suggested by Speziale is given by

$$\mathcal{F} = [1.0 - \exp(-\beta\bar{\Delta}/\eta_\kappa)]^n.$$

where the proposed model constants are given by $\beta = 0.001$ and $n = 1$; however it is expected that the model is very sensitive to these parameter.

The rescaling approach has been extended by Batten *et al* [7] in the framework of the *Limited-Numerical-Scales method*. The method can be applied to any combination of RANS and LES models which allow the specification of a length and velocity scale. In the LNS case the scaling function reads

$$\mathcal{F} = \frac{\min[l_s u_s, \ell_t u']}{\ell_t u'},$$

where l_s, u_s and ℓ_t, u' denote the characteristic length and velocity scales of the LES and RANS sub-models respectively.

3.5.2 Two-level modelling

For the simulation of internal combustion engines the previously discussed models show a limited practicability. The DES approach has been developed for aeronautical application; the criteria for switching between the RANS and LES mode is determined

solely on basis of the wall distance and thus restricts the RANS regions per se to wall regions. Spziale recommends the usage of higher order RANS models, i.e. Reynolds stress model, for the rescaling approach, which have been shown to be numerically problematic. Additionally the model formulation is based on the Kolmogorov length scale η_k , which defines the lower limit of the energy spectrum and thus cannot be well approximated by a RANS model.

Combing elements of the previously introduced approaches leads to a reformulation of the two-scale approach and will be discussed in the following. The fundamental approach follows the ideas proposed by Willems [128], and is based on the previous mentioned observation that in practical applications the mesh resolution locally allows to resolve a significant part of the turbulent spectrum beyond the integral length scale. This implies that not all of the available information about the local, transient turbulent flow structures are deployed. Thus, speaking in term of spectral space, the Willems model starts from the integral length scale and tries to capture the effect of smaller scales depending on the local mesh resolution.

The new, extended approach is based on the structural analogy of the evolution equations for the (RANS) turbulent kinetic energy, eq. (3.53), and the (LES) sub-filter kinetic energy, eq. (3.98). Similar to the approach followed by Willems [128], for a filter width $\bar{\Delta}$ of the order of the integral length scale the filtered field is assumed to tend towards the statistical average. On the other hand for decreasing filter widths the solution approaches the limit of a DNS. This behaviour can be realised via an adequate expression for the sub-filter dissipation rate ε_r . In contrast to the two-equation approach by Willems [128], the new hybrid model employs three transport equations: two equations on the integral level corresponding to a RANS model approach, namely the transport equations for k and ε , and one equation for the sub-filter kinetic energy on the filter scale are solved.

On the integral level, the standard k - ε equations for the integral turbulent kinetic energy k and the dissipation rate ε based on the formulation by El Tahry [31] are solved, which read

$$\begin{aligned} \frac{\partial \langle \rho \rangle k}{\partial t} + \frac{\partial \langle \rho \rangle \tilde{u}_j k}{\partial x_j} &= \frac{\partial}{\partial x_j} \left(\left[\mu + \frac{\mu_T}{\sigma_k} \right] \frac{\partial k}{\partial x_j} \right) + \mathcal{P} - \rho \varepsilon, \\ \frac{\partial \langle \rho \rangle \varepsilon}{\partial t} + \frac{\partial \langle \rho \rangle \tilde{u}_j \varepsilon}{\partial x_j} &= \frac{\partial}{\partial x_j} \left(\left[\mu + \frac{\mu_T}{\sigma_\varepsilon} \right] \frac{\varepsilon}{\partial x_j} \right) + C_1 \mathcal{P} \frac{\varepsilon}{k} - C_2 \langle \rho \rangle \frac{\varepsilon^2}{k} + C_3 \langle \rho \rangle \varepsilon \frac{\partial \tilde{u}_j}{\partial x_j}, \end{aligned}$$

where the turbulent eddy viscosity μ_T is given by $\mu_T = C_\mu \langle \rho \rangle \frac{k^2}{\varepsilon}$ and the turbulent production $\mathcal{P} = \tau_{ij} \frac{\partial u_j}{\partial x_i}$. For the sub-filter kinetic energy k_r , the one-equation model by Yoshizawa *et al.* [131] is used, which is given by

$$\frac{\partial \bar{\rho} k_r}{\partial t} + \frac{\partial \bar{\rho} \tilde{u}_j k_r}{\partial x_j} = \frac{\partial}{\partial x_j} \left[\left(\mu + \mu_t \right) \frac{\partial k_r}{\partial x_j} \right] + \mathcal{P}_r - \bar{\rho} \varepsilon_r.$$

Here the sub-filter dissipation ε_r and the sub-filter viscosity μ_t are given by

$$\varepsilon_r = c_\varepsilon \frac{k_r^{3/2}}{\bar{\Delta}} \quad \text{and} \quad \mu_t = C_k \bar{\rho} \sqrt{k_r} \bar{\Delta}$$

The model equations are solved in the whole domain. Using the integral value of the turbulent kinetic energy and the dissipation rate, the integral length scale ℓ_t can be estimated via

$$\ell_t = \frac{k^{3/2}}{\varepsilon}.$$

By comparing the integral length scale to the filter width, which is coupled to the mesh spacing via (3.79), a measure for the mesh resolution is obtained. For $\bar{\Delta} < \ell_t$ the mesh is fine enough to resolve part of the turbulent spectrum beyond the integral length scale, while in the opposite case for $\bar{\Delta} > \ell_t$ the largest turbulent structures are below the filter cut-off and cannot be represented on the current grid. In the latter case the evolution equation for the sub-filter kinetic energy k_r migrates towards the equation for the integral turbulent kinetic energy k by setting $\varepsilon_r = \varepsilon$. Thus two cases can be discerned:

$$\begin{aligned} \bar{\Delta} < \ell_t : \quad \varepsilon_r &= c_\varepsilon \frac{k_r^{3/2}}{\bar{\Delta}} & \mu_t &= C_k \rho \sqrt{k_r} \bar{\Delta} \\ \bar{\Delta} \geq \ell_t : \quad \varepsilon_r &= \varepsilon & \mu_t &= \mu_T \end{aligned}$$

This way the model mode, i.e. whether the LES or the RANS model is used in determining the turbulent eddy viscosity which is actually the only *turbulent* input parameter into the momentum equations, is identified by the ratio $\bar{\Delta}/\ell_t$. For $\bar{\Delta}/\ell_t < 1$ the mesh is fine enough to fully resolve the integral length scale thus the LES mode of the model is used, while for values larger than 1 the RANS mode is active.

The ε equation is solved in the whole domain, but in the LES region the algebraic relation for the sub-grid dissipation ε_r is employed. The standard model constants for the k - ε equations are used, while the constants for the LES model are chosen such, that the turbulent eddy viscosity changes continuously between the two regimes. This implies that for $\bar{\Delta} = \ell_t$ the sub-filter kinetic energy and the integral turbulent kinetic energy as well as the modelled turbulent viscosities are equal, i.e. $k_r = k$ and $\mu_t = \mu_T$ respectively. Therefore, in order to ensure that compatibility, the model parameters of the one-equation model are set to $C_k = 0.09$ and $C_\varepsilon = 1.0$.

3.5.3 Closing remarks

The hybrid RANS/LES models show good results for many applications in literature. However there is a fundamental problem associated with the approach, which can be referred to as the hybrid modelling defect. The transition region from RANS to LES, which is often referred to as a grey area, plays a crucial role in many flow configurations. The flow coming from the RANS domain and entering the LES region lacks information about turbulent scales which are supposed to be resolved on the fine mesh of the LES domain, i.e. the velocity fluctuations are (initially) underestimated. A similar effect occurs in case of mesh and topology changes in the course of a simulation with changing geometry, where the solution has to be interpolated between meshes of different resolutions; that situation is considered in detail in section 6.1. Here the energy spectra has a

hole at the mesh cut-off of the coarser grid, which has to be closed by the development of transient turbulent structures. In case that the development of these turbulent structures is too slow after the RANS/LES interface, the (modelled) turbulence level in the LES region is reduced and the turbulent stresses might be underpredicted. A potential workaround is the introduction of turbulent fluctuations by means of interface forcing, either from DNS [27, 28] or via synthesized fluctuations [8, 26]. The base techniques for the generation of the fluctuations are similar to those for the generation of turbulent initial conditions, which are discussed in the following section.

Being based on the hybridization of the classical Reynolds averaging and the filtering approach, the hybrid modelling approaches escape the usual theoretical frame work presented in sections 3.2 and 3.4. Employing a hybrid model, the resulting flow fields can neither be interpreted in terms of statistical averages nor as a filtered solution. The consistent physical interpretation of results especially in the interface region is non-trivial.

3.6 Artificial turbulence

The (filtered) Navier-Stokes equations supplemented by the enthalpy and species transport equations (2.1)–(2.2) form a coupled, non-linear system of partial differential equations which is valid for arbitrary flows. A unique solution of this system is only possible by the specification of initial and boundary conditions characterising particular flow configuration. Mathematically speaking the system represents an initial-boundary value problem.

In the case of laminar flow the specification of initial and boundary conditions by prescribing for instance constant values for the velocity, pressure and enthalpy fields is usually possible at low or moderate cost. Also temporally constant values are usually sufficient for RANS simulations of turbulent flows. A simple example is the case of inflow conditions for a plane mixing layer. For a RANS simulation the specification of the mean inflow velocity profiles, for instance via the $1/7^{th}$ distribution, and constant values for the turbulent quantities $\langle k \rangle$ and $\langle \varepsilon \rangle$ for each stream is sufficient.

The situation is fundamentally more complex for direct numerical simulations as well as for large-eddy simulations. Here the spectrum of the turbulent length scale is directly, for LES at least partially, computed. This leads to the requirement of a realistic description of the flow field both at the initial simulation time (initial solution) as well inflow conditions (boundary conditions). While for *open* systems, as for instance mixing and boundary layers, the question of inflow conditions is most critical, the focus for system whose temporal evolution is of interest, with the most simple and prominent case being decaying homogeneous turbulence, the initial conditions play inevitably a decisive role [34]. Therefore physical sensible, and in the case of inflow conditions unsteady, data subject to characteristic correlations of the velocity components are required.

The distinction between turbulent initial and boundary or inflow conditions can be

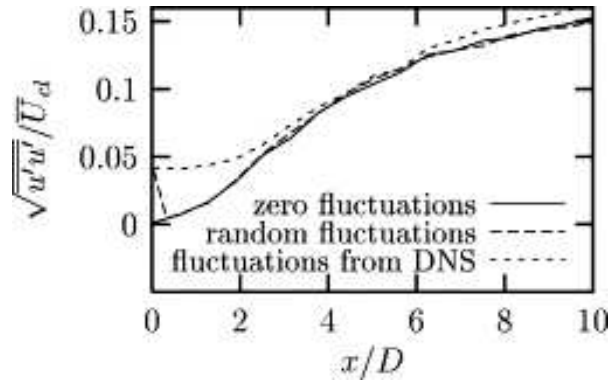


Figure 3.5: Influence of conventional inflow boundary conditions on the simulation of a plane jet. Comparison between inflow with zero fluctuations, random fluctuations and fluctuations from an external channel flow DNS; from [53].

overcome by means of the Taylor hypothesis [122] or the frozen-turbulence approximation [94, 123]. This hypothesis allows the approximation of spatial correlations by temporal correlations and vice versa. For the problem of creating turbulent inflow conditions the following approach based of the Taylor hypothesis can be used (see also [51, 53, 107]): in a first step a turbulent field with the desired turbulent characteristics is created, then slices from the field are extracted and used as inflow data. The problem of generating turbulent inflow data can thus be traced back to the creation of the corresponding single realisation of a turbulent field; therefore the following sections will focus on the creating of turbulent initial conditions.

The common approach to generate pseudo-turbulent velocity fields superimposes a field of random fluctuations u'_i to the mean velocity field $\langle u_i \rangle$. The most simple way is to apply random noise, i.e. the signal on each node (computational cell) is just determined as a random number. Investigations by Klein et al [53] using this data as inflow conditions for a plane mixing layer revealed that the turbulence generated by this method is immediately damped to zero right after the inflow plane. The velocity fluctuations on the centreline of the jet are given in figure 3.5. Results obtained for the noise inflow-condition are compared to data for a steady laminar conditions and for pre-computed turbulence: the noise conditions yields a proper fluctuation level on the inflow, but is then dissipated immediately. This effect is explained by the lack of energy in the low-wave number range of the random-number turbulence since random noise possesses an energy spectrum of the form $E(\kappa) = const.$

3.6.1 Fourier transform approach

To overcome the problem associated with the employment of pure white noise, namely the lack of energy on the small and too much energy on the high wave numbers, Lee et al [60] applied an inverse Fourier transformation using an energy spectrum of real turbu-

lence. For illustration purpose a one dimensional example will be used in the following; a more thorough discussion and numerical details are given in [12, 16].

The Fourier transformation of a signal u_k in physical space to a signal \hat{u}_n in wave number space can be approximated by the discrete Fourier transformation

$$u_k = \frac{1}{N} \sum_{n=0}^{N-1} \hat{u}_n \exp\left(\frac{2\pi}{N} jkn\right), \quad (3.101)$$

where N is the number of Fourier modes used in the approximation, $\hat{u}_n = |\hat{u}_n| \exp(j\Phi_n)$ are the complex Fourier coefficient for mode n , where Φ_n denotes the phase angle. The energy of the transformed signal \hat{u}_n is given by

$$\sum_{n=0}^{N-1} E(n) := \frac{1}{N} \sum_{n=0}^{N-1} |U_n|^2 = \sum_{n=0}^{N-1} |u_i|^2 \quad (3.102)$$

yielding a connection between the absolute value of \hat{u}_n and the energy spectrum $E(n) \sim |\hat{u}_n|^2$. With a random phase angle Φ_n the inverse Fourier transform leads to a signal featuring the prescribed spectrum $E(n)$.

As this method is based on Fourier transformation the implementation is complex and involved. For efficiency reasons fast Fourier transform (FFT) needs to be applied which places a severe restriction to the number of grid points and topology; equidistant, Cartesian grids are required, thus the application is limited to simple, rectangular geometries. For complex geometries the initialisation on a regular mesh followed by an interpolation onto the actual grid offers a possible workaround; however due to the employed interpolation the initialised spectrum will be disturbed.

3.6.2 Diffusion process

To overcome some of the difficulties associated with the Fourier transform approach, Klein et al [53] developed a method based on digital filters to generate pseudo-turbulent velocity data. Although this method has been developed having applicability and simplicity in mind, an equidistant mesh-spacing is still required. Keeping the fundamental idea of filtering, a new approach has been developed in [51], where instead of an explicit digital filter a diffusion process is applied for converting white noise into a signal featuring the required length-scales.

The starting point is a three-dimensional random (velocity) field which is normalised to fulfil $\langle u_i \rangle = 0$ and $\langle u_i u_i \rangle = 1$, and scaled by the root of the local cell volume. The resulting field has a typical length scale of half a cell width and does not feature any sensible autocorrelation. In the next step a diffusion operator, eq. (3.103), is applied to the field removing the small structures of the order of the mesh size while leaving the larger structures unaffected.

$$\frac{\partial u_i}{\partial t} = \frac{\partial}{\partial x_j} \left(\nu \frac{\partial u_i}{\partial x_j} \right) \quad (3.103)$$

The removal of the small scale structures by diffusion is due to the steep velocity gradient in the random field as the diffusion of momentum is proportional to the rate of strain: $\tau_{ij} = 2\mu S_{ij}$. It is interesting to note that the application of the diffusion operator is equivalent to the convolution with a Gaussian filter, thus the process yields an auto-correlation function of Gaussian shape. The (integral) length scale ℓ_t of the velocity field increases with the diffusion time and can be estimated as

$$\ell_t = \sqrt{2\pi\nu t_{\text{diff}}}, \quad (3.104)$$

where t_{diff} denotes the time of diffusion application [51, 107]. The fluctuating field obtained by this procedure can finally be scaled to yield the desired integral turbulent kinetic energy. The spectrum of the pseudo-turbulence corresponds to the case of homogeneous isotropic turbulence. In case an anisotropic field is sought after, performing a transformation as proposed by Lund et al [68] yields the desired Reynolds stresses.

As this method works completely in physical space it can be applied to arbitrary geometries and on arbitrary meshes. The implementation and integration into existing CFD codes is straightforward.

3.6.3 Synthesized turbulence

A time-space turbulent velocity field can be simulated using random Fourier modes [57]. Billson [10] applied this technique to generate synthesized turbulence in the framework of the Stochastic Noise Generation and Radiation (SNGR) method [4, 5, 9].

A turbulent velocity field can be constructed as a sum of Fourier modes

$$\mathbf{u}_s(\mathbf{x}) = 2 \sum_{n=1}^N \hat{u}_n \cos(\boldsymbol{\kappa}_n \cdot \mathbf{x} + \psi_n) \boldsymbol{\sigma}_n \quad (3.105)$$

where \hat{u}_n , ψ_n and $\boldsymbol{\sigma}_n$ are the amplitude, phase and direction of the n^{th} Fourier mode. The direction $\boldsymbol{\sigma}_n$ obeys the normalisation condition and has the length $|\boldsymbol{\sigma}_n| = 1$.

The orientation of the wave number vector $\boldsymbol{\kappa}_n$ is chosen randomly on a sphere with radius $\kappa_n = |\boldsymbol{\kappa}_n|$ to ensure the isotropy of the generated velocity field. Assuming incompressibility the continuity equation gives the following relation

$$\boldsymbol{\kappa}_n \cdot \boldsymbol{\sigma}_n \equiv 0 \quad \text{for all } n; \quad (3.106)$$

this implies that the wave number vector $\boldsymbol{\kappa}_n$ and the spatial direction $\boldsymbol{\sigma}_n$ of the n^{th} mode are perpendicular.

The space angles ϕ_n , α_n , ϕ_n and the phase ψ_n are chosen randomly with probability functions given in table 3.4. The probability function of θ , $p(\theta) = 1/2 \sin(\theta)$ is chosen such that the distribution of the direction $\boldsymbol{\kappa}_n$ is uniform on the surface of a sphere, i.e. the probability of a randomly selected direction is the same for all surface elements dA .

| | |
|------------------------------------|-----------------------------|
| $p(\phi_n) = 1/(2\pi)$ | $0 \leq \phi_n \leq 2\pi$ |
| $p(\psi_n) = 1/(2\pi)$ | $0 \leq \psi_n \leq 2\pi$ |
| $p(\theta_n) = (1/2) \sin(\theta)$ | $0 \leq \theta_n \leq \pi$ |
| $p(\alpha_n) = 1/(2\pi)$ | $0 \leq \alpha_n \leq 2\pi$ |

Table 3.4: Probability distributions of random variables.

The amplitude \hat{u}_n of each mode in equation (3.105) is determined on basis of the energy spectra via

$$\hat{u}_n = \sqrt{E(\kappa_n) \Delta\kappa_n}, \quad (3.107)$$

where $\Delta\kappa_n$ is a small interval in the spectrum located at κ_n . A model spectrum $E(\kappa_n)$ is required to simulate the shape of the energy spectrum for isotropic turbulence. Following [10] a modified von Kármán-Pao spectrum is chosen in the present work which is given by

$$E(\kappa) = \alpha \frac{u'^2}{\kappa_e} \frac{(\kappa/\kappa_e)^4}{[1 + (\kappa/\kappa_e)^2]^{17/6}} \exp[-2(\kappa/\kappa_e)^2]; \quad (3.108)$$

here κ is the wave number, $\kappa_\eta = 2\pi/\eta_k$ is the wave number corresponding to the Kolmogorov length scale (Kolmogorov wave number), ν is the kinematic molecular viscosity and ε is the turbulent dissipation rate. u'^2 is the r.m.s. value of the velocity fluctuations corresponding to the turbulent kinetic energy, i.e. $u'^2 = 2/3 \langle k \rangle$. κ_e corresponds to the wave number containing the most energy containing eddies at the peak of the spectrum and is related to the integral length scale ℓ_t via $\kappa_e = 2\pi/\ell_t$. The numerical constant α determines the kinetic energy of the spectrum. The integral of the energy spectrum, equation (3.108), over all wave numbers must be equal to the total turbulent kinetic energy

$$\langle k \rangle = \int_0^\infty E(\kappa) d\kappa, \quad (3.109)$$

which can be used to determine the constant α . The algorithm has been implemented as follows which slightly diverges from the one proposed in [25]:

1. for each mode n create a set of random angles ϕ_n , α_n , and θ_n , and a random phase ψ_n ;
2. create a set of randomly oriented unit vectors $\mathbf{e}_{\kappa,n}$ for each Fourier mode; these vectors correspond to normalised wavenumber vectors $\mathbf{e}_{\kappa,n} = \kappa_n/|\kappa_n|$;
3. determine the spatial direction vectors σ_N by means of the orthogonality constrained imposed by the spectral continuity equation (3.106);
4. define the spectra by determining the characteristic wave numbers κ_e and κ_η ;

5. define the highest (resolved) wave number based on the mesh resolution $\kappa_{max} = \kappa_c = \pi/\Delta$; the smallest wave number κ_{min} is set to zero; [25] suggests to define the smallest wave number $\kappa_1 = \kappa_c/p$ with $p > 1$.
6. determine the numerical constant α of the modified von Kármán-Pao spectrum (3.108) by means of (3.109), where the upper limit of the integration is taken to be the Kolmogorov wave number κ_η ;
7. divide the wavenumber space $\kappa_{max} - \kappa_{min}$ into N equally spaced modes of size $\Delta\kappa$;
8. the amplitude \hat{u}_n of each mode is obtained from (3.107)
9. calculate the velocity fluctuations by summing up the contributions from each wave number using (3.105).

4 Premixed combustion

Technical processes in gaseous combustion can be subdivided in terms of mixing, i.e. premixed, non-premixed or partially premixed combustion. Two classical examples for premixed and non-premixed combustion are given by spark-ignition and Diesel engines respectively. In spark-ignition engines, fuel and oxidiser are mixed by turbulence for a sufficiently long period until the electric spark ignites the mixture. On the other side in Diesel engines liquid fuel is injected into compressed hot air; the fuel evaporates and partially mixes with the air before auto-ignition occurs. For partial pre-mixing combustion an example is given by the modern spark ignition direct injection (SIDI) engine.

4.1 Laminar premixed combustion

Analogue to the situation encountered in fluid flow, that laminar flow conditions are rarely met in practical applications, most flames of practical interest are characterised by an significant level of turbulence. In the case of premixed combustion, turbulence enhances the transport of unburnt mixture towards the flame. Therefore the structure of turbulent flames cannot be expected to be the same as for laminar flames. However, a turbulent flame is generally considered to consist of an ensemble of *flamelets*, i.e. of elementary laminar flames transported and stretched/deformed by the flow structures.

In many combustion devices the turbulent scales of the flow are significantly larger than the chemical time and length scales. Due to that scale separation effect, the combustion process can, as a first order approximation, be regarded as being decoupled from and thus not being influenced by the turbulence. When the largest scales of the premixed flame and the smallest scales of the turbulence begin to interfere, turbulent straining effects start to interact with the chemistry. Up to a certain magnitude and by introducing asymptotic second-order expansion taking curvature effects on the laminar flame structure into account, the flame can still be attributed to the flamelet regime.

4.1.1 Structure of premixed flames

The simplest flame configuration is a planer premixed flame propagating in one direction. Neglecting wall effects a flame in a duct can be taken as an idealised example. For this flame only one-dimensional equations normal to the flame front are employed and the continuity equation reduces to a constant expression for the mass flow rate through the flame front:

$$\rho u = \text{const.} = (\rho s_L^0) = \rho_u s_{L,u}^0. \quad (4.1)$$

Here, the index u indicates the unburnt state and the laminar burning velocity $s_{L,u}^0$ denotes the velocity of the flame relative to the unburnt mixture. The expression (ρs_L^0) is also referred to as the *mass burning rate*.

The first theoretical analysis of the structure of premixed flames have been performed by *Zeldowitsch* and *Frank-Kamenetzki* [132] in 1938. Even though their assumption of a global one step kinetics is simplifying, conclusions of fundamental importance can be drawn and used for combustion modelling. A global one step reaction assumes the conversion of fuel and oxidiser are directly into products; therefore the chemical reaction can symbolically be written as



where F , O_x and P denote the fuel, oxidiser and combustion products respectively. Intermediate species are not considered. The propagation of the premixed flame front is induced by the transport of thermal energy from the reaction zone, where the heat release occurs, into the unburnt mixture. Therefore, the head of the premixed flame front is referred to as the preheat zone. The temperature of the unburnt gas increases exponentially towards the reaction zone. The point at which the thermal energy of the mixture reaches the activation energy threshold marks the beginning of the reaction zone. Considering a stationary, planar flame front, the flame structure as depicted in figure 4.1 is obtained.

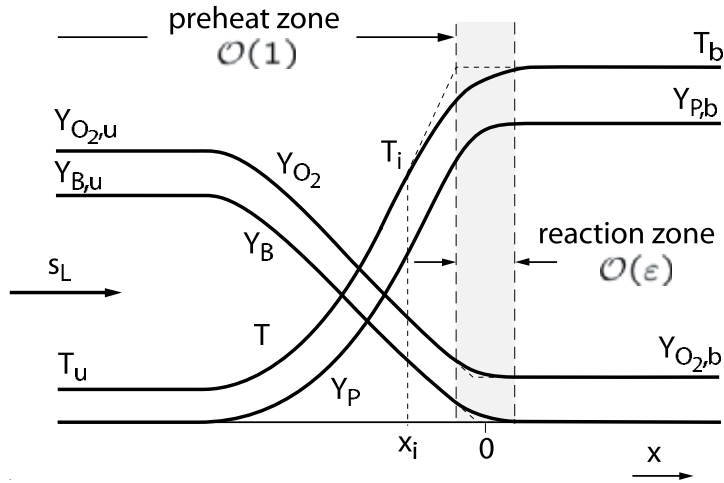


Figure 4.1: Structure of a lean premixed flame assuming a global one-step kinetics and large activation energy [86].

By means of an asymptotic analysis, Peters [83] derived an expression for the mass burning rate which primarily depends on the ratio of the thermal conductivity λ_b to the heat capacity c_p and the combustion time scale t_c :

$$(\rho_u s_L)^2 = \frac{\lambda_b \rho_u}{c_p t_c}, \quad (4.3)$$

where the combustion time scale t_c is given by

$$t_c = \frac{\rho_u c_p (T_b - T_u)^2 E^2}{2B\rho_b \mathcal{R}^2 T_b^4 A} \exp\left(\frac{E}{\mathcal{R}T_b}\right). \quad (4.4)$$

Here, E denotes the activation energy, B is the rate coefficient, and A is (approximately) constant, depending on physical properties of the fuel and oxidiser, see [83]. Equation (4.4) implies that the combustion time scale primarily depends on ratio of the burnt (T_b) and unburnt (T_u) temperatures, the rate coefficient B and the activation energy E of the reaction mechanism. Note that the chemical time scale is not influenced by diffusion effects.

Based on equation (4.3) two physical processes can be identified to be responsible for the flame propagation. The first is the chemical reaction, imposing a chemical time scale. The second process is the (diffusive) transport of thermal energy into the preheat zone. An increase of the burning velocity s_L can therefore be achieved either by decreasing the chemical time scale t_c , or by increasing λ_b/c_p .

For multi-step reaction mechanisms the main observations are still valid. An asymptotic analysis of stoichiometric methane/air flame using a four step mechanism [82, 87] leads to the subdivision of the flame structure into three regions (cf. figure 4.2):

1. the non-reacting *preheat zone* as in the one-step asymptotic;
2. the *inner layer* in which hydro-carbon fuel is completely consumed and intermediate species are formed; and
3. the *oxidation layer* in which the intermediates are oxidised.

The resulting expression for the mass burning rate has the same form as equation (4.3) with the expression for the chemical time scale being more involved than equation (4.4). The ratio λ_b/c_p has to be evaluated at temperature T_0 , which is the characteristic temperature for the inner layer. Denoting the spatial position of the inner layer by x_0 , the flame diffusivity D_0 and the laminar flame thickness ℓ_f can be defined as

$$D_0 = s_{L,u} \ell_f = \frac{1}{\rho_u} \frac{\lambda}{c_p} \Big|_{x_0}. \quad (4.5)$$

The exact position x_0 for the evaluation of the inner layer quantities is assumed to be at the location of the maximal heat release, see figure 4.2. The inner layer thickness ℓ_δ is approximately one order of magnitude smaller than the flame thickness ℓ_f .

In three dimensions the flame front can be curved and is subjected to strain by the flow field. These effects have an influence onto the flame structure and modify the laminar burning velocity s_L . It can be shown [21, 72] that for a one-step, large activation energy reaction and with the assumption of constant properties the burning velocities s_L can be approximated as

$$s_L = s_L^0 - D_{\mathcal{L}} \kappa - \mathcal{L} S. \quad (4.6)$$

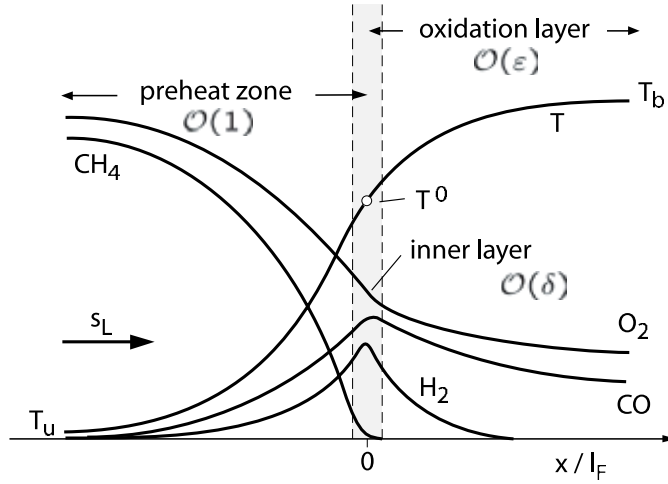


Figure 4.2: Structure of a stoichiometric methane-air, consisting of the preheat zone, the inner reaction layer and the oxidation layer [86].

where the strain of the flame \mathbf{S} is defined as

$$\mathbf{S} = -(\mathbf{n} \cdot \mathbf{u} \cdot \mathbf{n})|_{x_0}, \quad (4.7)$$

and the flame curvature is given by

$$\kappa = \nabla \cdot \mathbf{n}; \quad (4.8)$$

x_0 defines the inner layer position, s_L^0 is the burning velocity of the unstrained flame, \mathcal{L} the *Markstein length*, and

$$D_{\mathcal{L}} = s_L^0 \mathcal{L} \quad (4.9)$$

the *Markstein diffusivity*. Neglecting the effects of strain and assuming a Markstein number of unity the previous equation can be simplified to

$$s_L(\kappa) = s_L^0 - D\kappa. \quad (4.10)$$

The result of this simplification shows that for a concave flame front ($\kappa < 0$) the burning velocity increases, while s_L decreases for a convex front ($\kappa > 0$) with respect towards the unburnt gas. This implies that curvature effects tend to smooth out perturbations of the front towards a flattened flame by diffusive effects.

4.1.2 The level-set approach for laminar flame propagation

The G -equation model has been introduced by Williams [129] and is based on the flamelet modelling assumption. Here a level set method is used to describe the evolution of the flame surface as an interface between unburnt and burnt gases. The level set function G

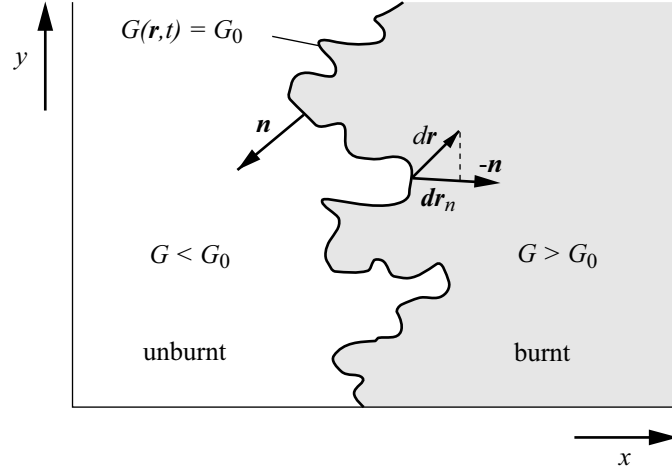


Figure 4.3: A schematic representation of the flame front as an iso-scalar surface $G(\mathbf{r}_f, t) = G_0$ [83].

is a scalar field defined such that the iso-surface $G = G_0$ defines the flame front position; $G < G_0$ indicates unburnt mixture, while $G > G_0$ lies on the burnt side, see figure 4.3. The flame front position is given by the inner layer position, i.e. $G = G_0$ where $T = T_0$.

The instantaneous and local G -equation can be derived by considering the instantaneous flame surface. The derivation is described in detail for instance in [32, 47, 85, 129], but is sketched briefly in the following. The implicit representation of a level set function G is given by

$$G(\mathbf{r}_f, t) - G_0 = 0, \quad (4.11)$$

where $\mathbf{r}_f = \mathbf{r}_f(\mathbf{x}, t)$ denotes the flame front position. Differentiating equation (4.11) leads to

$$\frac{\partial G}{\partial t} + \frac{d\mathbf{r}_f}{dt} \cdot \nabla G = 0. \quad (4.12)$$

The displacement velocity of the flame front is given by

$$\frac{d\mathbf{r}_f}{dt} = \mathbf{u} + s_L \cdot \mathbf{n}, \quad (4.13)$$

where \mathbf{u} denotes the local fluid velocity, s_L the laminar burning velocity and \mathbf{n} is the flame normal vector directed from the burnt side into the unburnt, i.e. pointing into the flame propagation direction. The flame normal vector can be expressed via the gradients of G as

$$\mathbf{n} = -\frac{\nabla G}{|\nabla G|}. \quad (4.14)$$

Combining the previous equations yields the instantaneous G -equation:

$$\frac{\partial G}{\partial t} + \mathbf{u} \cdot \nabla G = s_L |\nabla G| \quad (4.15)$$

The previous equation has been derived from equations (4.11) and (4.13); both describe the flame surface, thus equation (4.15) is also valid at the surface position only, i.e. at $G = G_0$. For $G \neq G_0$ outside the flame surface, a suitable definition needs to be given. While the interpretation of G outside the flame surface is somewhat arbitrary, it is commonly defined to be a distance function which leads to the distance constrained

$$|\nabla G| = 1. \quad (4.16)$$

Equation (4.15) does not account for effects due variable density due to combustion. Introducing the modified laminar burning velocity (4.10) into (4.15) and multiplying with the local density leads to

$$\rho \frac{\partial G}{\partial t} + \rho \mathbf{u} \cdot \nabla G = (\rho s_L^0)_u |\nabla G| - \rho D \kappa |\nabla G| \quad (4.17)$$

where $(\rho s_L^0)_u$ is the mass burning rate of an unstretched flame with respect to the unburnt.

4.2 Physics of turbulent flame propagation

Premixed turbulent combustion often occurs in thin flame fronts. The propagation of these fronts, and hence the heat release, is governed by the interaction of transport and chemistry within the front. In laminar fronts this strong coupling is reflected in the scaling of the laminar burning velocity $s_L \sim \sqrt{D/t_c}$, see equations (4.3) and (4.5). In turbulent premixed flames, the flame front strongly interacts with turbulent structures, leading to a significant increase of the mass consumption and flame thickness.

4.2.1 Regimes in premixed combustion

Figure 4.4 depicts different regimes of premixed turbulent combustion in terms of velocity and length scale ratios according to Peters [85]. For scaling purposes it is assumed that the diffusivities for all scalars are equal, the Schmidt number $Sc = \nu/D$ is unity and the flame thickness ℓ_F and the flame time t_F are given by

$$\ell_f = \frac{D}{s_L} \quad t_F = \frac{D}{s_L^2}. \quad (4.18)$$

Based on the turbulent intensity v' and the turbulent length scale ℓ , the turbulent Reynolds number Re_t and the turbulent Damköhler number Da can be defined as

$$Re = \frac{v' \ell}{s_L \ell_F} \quad \text{and} \quad Da = \frac{s_L \ell}{v' \ell_F}. \quad (4.19)$$

Additionally two turbulent Karlovitz numbers can be defined based in the Kolmogorov time length and velocity scales. The first one is defined as

$$Ka = \frac{t_F}{t_\eta} = \frac{l_F^2}{\eta^2} = \frac{v_\eta^2}{s_L^2} \quad (4.20)$$

measures the ratio of the flame and the Kolmogorov scales. As second Karlovitz number Ka_δ based on the inner layer thickness l_δ may be introduced as

$$Ka_\delta = \frac{l_\delta^2}{\eta^2} = \delta^2 Ka \quad (4.21)$$

with l_δ being the inner layer thickness, and δ denotes the ration of the inner layer thickness to the flame thickness $l_\delta = \delta l_F$.

The Damköhler number can be interpreted as the ratio of the turbulent time scales τ_t to the chemical time scale τ_c :

$$Da = \frac{\tau_t}{\tau_c}.$$

It is interesting to consider two limits of the Damköhler number. Small Damköhler numbers, $Da \ll 1$, indicate that the characteristic turbulent time scale are much smaller than those of the chemical kinetics. This implies that the turbulent structures are small compared to the flame thickness and can penetrate the flame. The turbulent mixing process becomes important even in the interior of the flame, as the determining process, the chemical reaction, are comparatively slow. That type of reaction resembles of a homogeneous reactor and is referred to as distributed combustion, as a single flame sheet cannot be established. In the opposite limit for large Damköhler number, i.e. $Da \gg 1$, the chemical reaction is infinitely fast compared to the characteristic turbulent time scales. The turbulent structures are larger than the flame thickness and cannot penetrate the flame front. Thus the flame has a laminar-like structure, and, correspondingly, this regime is called the *flamelet regime*.

Figure 4.4 shows the premixed combustion regimes for fully turbulent flames in terms of the normalised turbulence intensity v'/s_L and the normalised length scale ℓ/ℓ_F . The laminar flames regime is separated from the turbulent regimes by the $Re_t = 1$, which is equivalent to $v'/s_L = (\ell/\ell_t)^{-1}$.

In the *wrinkled flamelet regime*, where $v' < s_L$, the turn-over velocity v' of the large turbulent eddies is not large enough to compete with the advancement of the flame front with the laminar burning velocity s_L . Laminar flame propagation is dominating over flame front corrugation by turbulence.

The line $v'/s_L = 1$ separates the wrinkled flamelet regime from the *corrugated flamelet regime*. Here the largest turbulent eddies are able to interact with the advancing flame front. This regime is characterised by the inequalities $Re > 1$ and $Ka < 1$. Considering equation (4.20) the latter inequality indicates the $\ell_F < \eta_K$, i.e. the entire flame structure is embedded within eddies of the size of the Kolmogorov scale, where the flow is quasi-laminar; thus the flame structure is not perturbed by turbulence. In both the wrinkled

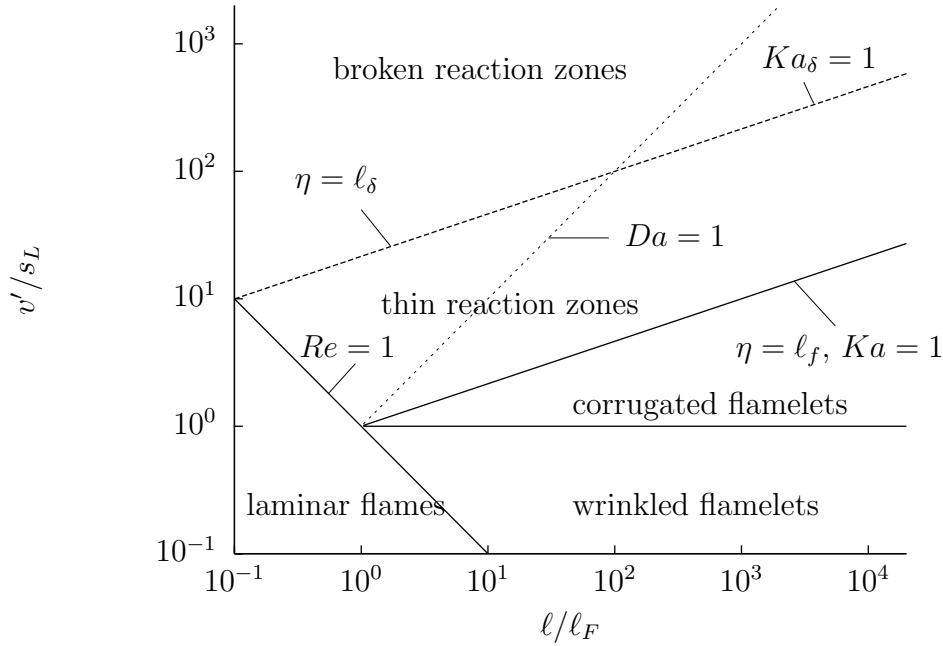


Figure 4.4: The combustion regime diagramme according to Peters [85].

flamelet and the corrugated flamelet regime the thickness of the flame can be regarded as small in comparison with the size of the characteristic turbulent eddies interacting with the flame. Therefore the flame structure in both regimes is internally not influenced by the turbulence, which implies that equation (4.17) can be employed for the description of the flame propagation. The turbulence in these two regimes is referred to as *large scale turbulence*.

In the *thin reaction zone* the smallest eddies of the Kolmogorov size η_K start to interact with the laminar flame structure. The boundary, separating this regime from the corrugated flamelets regime is determined by the turbulent Karlovitz number $Ka = 1$. The eddies are still larger than the inner layer thickness ℓ_δ and can therefore not penetrate into that layer. With the relation $\varepsilon \sim v'^3/\ell$ and the definition for the Kolmogorov length scale η_K , equation (3.4), for constant values of Ka the following relationship can be obtained:

$$\left(\frac{s_L}{v'}\right)^3 \sim \frac{\ell_F}{\ell}. \quad (4.22)$$

In this regime it is assumed that equation (4.17) is valid including curvature effects term on the right-hand side. The turbulence in this regime can be characterised as *small scale turbulence*.

Beyond the line $Ka_\delta = 1$ the turbulent eddies can perturb the reaction zone with the consequence that locally chemistry breaks down due to enhanced heat loss to the preheat zone. Consequently the turbulent flame is torn apart and partially quenched.

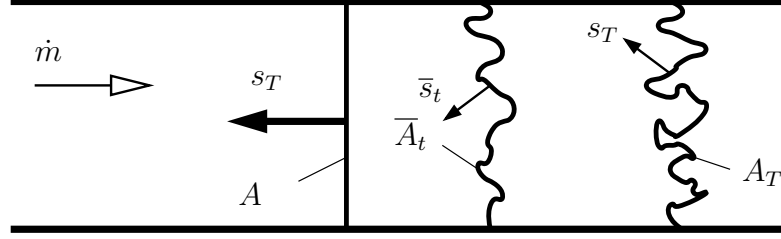


Figure 4.5: An idealised stationary turbulent premixed flame in a duct.

At such turbulence level a flamelet structure cannot exist. The regime is referred to as the *broken reaction zones*.

4.2.2 The turbulent burning velocity

The turbulent burning velocity represents the key element to capture the physics of the propagating premixed flame front.

The turbulent burning velocity s_T is the displacement speed with which the mean flame front propagates normal to itself through the turbulent flow field and represents the key element to capture the physics of the propagating premixed flame front. Consider the stationary turbulent premixed flame in a duct as depicted in figure 4.5. Due to continuity the mass flux \dot{m} through the cross section A of the duct with velocity s_T is constant. This mass flux must be equal to the mass flux through the instantaneous flame front area A_T moving with the laminar burning velocity s_L , thus

$$\dot{m} = \rho_u s_L A_T = \langle \rho \rangle_u s_T A, \quad (4.23)$$

where both s_L and s_T are evaluated with respect to the unburned gas. Assuming constant unburnt densities the burning velocity ratio is proportional to the surface area ratio

$$\frac{s_T}{s_L} = \frac{A_T}{A}. \quad (4.24)$$

The flame surface can be averaged or filtered on any intermediate scale within the inertial range resulting in a filtered flame surface area \bar{A}_t . According to equation (4.23) the mass flux through the filtered surface has to be equal to \dot{m} , thus

$$s_L A_T = s_T A = \bar{s}_t \bar{A}_t. \quad (4.25)$$

This demonstrates that the product $\bar{s}_t \bar{A}_t$ is inertial scale invariant, thus $\bar{s}_t \bar{A}_t$ can be calculated at any scale within the inertial subrange, defining $s_L A_T$ of the instantaneous flame front. Equation (4.25) therefore justifies the application of LES-type model to turbulent premixed combustion as the evaluation of $\bar{s}_t \bar{A}_t$ at the threshold length scale (filter width Δ) is equal to $s_L A_T$.

The cross section area A describes the area that can be observed from a viewpoint perpendicular to turbulent flame front. This front is perturbed, wrinkled and convoluted by turbulence to generate the enhanced flame front A_T . The ratio between the instantaneous area and the so-called mean flame front defines the flame surface area ratio σ :

$$\sigma = \frac{A_T}{A} = \sigma_t + 1. \quad (4.26)$$

The *turbulent flame surface area ratio* σ_t denotes the increase of flame surface due to turbulence effects. For a laminar flame $\sigma = 1$, and correspondingly σ_t becomes $\sigma_t = 0$. After averaging σ or σ_t respectively, the turbulent burning velocity is obtained as

$$s_T = \tilde{\sigma} s_L = (1 + \tilde{\sigma}_t) s_L. \quad (4.27)$$

4.3 Progress variable approach

The formulation of a model for turbulent flame propagation based on the progress variable approach is quite attractive as the calculation of burnt and unburnt mass fractions in flow problems can be performed easily. Additionally the source term in the transport equation for the progress variable can easily be linked to the heat release.

The progress variable c is a scalar quantity which can be viewed either as a normalised temperature or as a normalised product mass fraction of the product species Y_p and the maximum product mass fraction in the burnt gas $Y_{p,b}$:

$$c = \frac{T - T^u}{T^b - T^u} \quad \text{or} \quad c = \frac{Y_p}{Y_{p,b}}. \quad (4.28)$$

Analogous to equation (2.7), the transport equation for c can be derived as

$$\frac{\partial \rho c}{\partial t} + \frac{\partial \rho u_i c}{\partial x_i} = \frac{\partial}{\partial x_k} \left(\rho D_c \frac{\partial c}{\partial x_k} \right) + \dot{\omega}_c, \quad (4.29)$$

where $\dot{\omega}_c$ is the reaction rate of the premixed flamelet for a given c . Favre averaging leads to a transport equation for the mean progress variable \tilde{c} which reads

$$\langle \rho \rangle \frac{\partial \tilde{c}}{\partial t} + \langle \rho \rangle \tilde{u}_i \frac{\partial \tilde{c}}{\partial x_i} = \frac{\partial}{\partial x_k} \left(\frac{\mu_t}{Pr_t} \frac{\partial \tilde{c}}{\partial x_k} \right) + \langle \dot{\omega}_c \rangle, \quad (4.30)$$

where the turbulent transport term has been modelled by a gradient-diffusion, turbulent viscosity approach, and laminar diffusion has been neglected. For the mean reaction rate $\langle \dot{\omega}_c \rangle$ a closure model is required. Popular closure examples include the Eddy Break-Up model (EBU), originally developed by Spalding [116, 117], the Bray-Moss-Libby model [14], as well as closures based in the flame surface density $\Sigma = \frac{dA_T}{dV}$, for instance the Coherent Flame Model [70] (CFM); an overview of the latter approach can be found for instance in [92, 99].

4.4 The level-set approach for turbulent flames

The level set approach for laminar flames has been presented in section 4.1.2. As pointed out by Peters [85] and Oberlack *et al* [80], the straightforward extension of the laminar G -equation (4.15) to turbulent flows by applying the classical averaging methods to determine the location of the mean flame front cannot be employed. Unlike conserved quantities, the G -field has a physical meaning only at $G = G_0$, thus G is not defined in the whole flow field. Employing a classical averaging procedure requires not only an extension of the G -field to $G \neq G_0$, but would also depend of the chosen extension, i.e. different extensions would yield different mean flame front position [126]. Thus an alternative approach is required for the definition of the mean flame front for turbulent flames.

A suitable averaging procedure based on the probability density of locating the flame front at a given location has been introduced by Oberlack *et al.* [80] for incompressible fluids. A volumetric averaging is employed to determine the position of the volumetrically averaged flame front by

$$\langle\langle \mathbf{x}_f \rangle\rangle \equiv \iiint_{-\infty}^{+\infty} \mathbf{x}_f P(\mathbf{x}_f) d\mathbf{x}_f. \quad (4.31)$$

Here \mathbf{x}_f is an instantaneous realisation of the flame front, and $P(\mathbf{x}_f)$ is the probability of finding the flame front at \mathbf{x}_f . As pointed out by Ewald [32], for compressible flows, the previous definition is less accurate due to density gradients across the turbulent flame brush, which induces a movement of the mean flame front position. This movement is avoided by employing a mass weighted averaging procedure:

$$\langle \rho \rangle \tilde{\mathbf{x}}_f \equiv \langle\langle \rho \mathbf{x}_f \rangle\rangle \equiv \iiint_{-\infty}^{+\infty} \rho(\tilde{\mathbf{x}}_f | \tilde{\mathbf{x}}_f) \mathbf{x}_f P(\mathbf{x}_f) d\mathbf{x}_f. \quad (4.32)$$

4.4.1 Transport equations for the mean flame front position and flame brush thickness

In contrast to the laminar field G , for the turbulent case the scalar \tilde{G} is considered and the mean flame front position is defined analogous to the laminar case where

$$\tilde{G} = G_0, \quad (4.33)$$

i.e. where $\mathbf{x} = \tilde{\mathbf{x}}_f$. Employing a similar approach as discussed in section 4.1.2 yields the (unclosed) equation for the mean flame front position [32]:

$$\langle \rho \rangle \frac{\partial \tilde{G}}{\partial t} + \langle \rho \rangle \nabla \tilde{G} \cdot \tilde{\mathbf{u}} + \langle \rho \rangle \widetilde{\nabla g \mathbf{u}''} + \nabla \tilde{G} \cdot \langle\langle \rho (s_L(\kappa) \mathbf{n}) \rangle\rangle = 0. \quad (4.34)$$

Here g denotes the Euclidean norm of the distance vector between the instantaneous and the average flame front $\mathbf{g} = \mathbf{x}_f - \tilde{\mathbf{x}}_f$, given by $g \equiv -\text{sign}(G)|\mathbf{g}|$. In equation (4.34) two unclosed terms appear: the third term represents turbulent transport, and the last term on the l.h.s. is the turbulent flame propagation term.

The variance of \tilde{G} is a measure for the fluctuations of the instantaneous flame front about their mean position. Therefore, the turbulent flame brush thickness $l_{f,t}$ is defined as the square root of variance

$$l_{f,t} \equiv \frac{\sqrt{\widetilde{G''^2}}}{|\nabla \tilde{G}|}. \quad (4.35)$$

The averaging operator yielding the variance is valid on the mean flame front only. In analogy to (4.32) it can be defined as

$$\langle \rho \rangle \widetilde{G''^2} \equiv \langle \langle \rho g^2 \rangle \rangle \equiv \iiint_{-\infty}^{+\infty} \rho(\tilde{\mathbf{x}}_f | \tilde{\mathbf{x}}_f) g^2 P(\mathbf{x}_f) d\mathbf{x}_f. \quad (4.36)$$

An equation for the variance $\widetilde{G''^2}$ may be derived by first decomposing \mathbf{g}^2 as $\mathbf{g}^2 = \widetilde{G''^2} = g''$. Considering the substantial derivative and employing the chain rule of differentiation, after some algebra the following equation for $\widetilde{G''^2}$ is obtained:

$$\langle \rho \rangle \frac{\partial \widetilde{G''^2}}{\partial t} + \langle \rho \rangle \frac{d\mathbf{x}_f}{dt} \cdot \nabla \widetilde{G''^2} + \langle \rho \rangle \nabla \widetilde{g''} \cdot \mathbf{u}'' + \langle \langle \rho \nabla g'' \cdot (s_L \mathbf{n}) \rangle \rangle = 2 \langle \langle \rho \mathbf{g} \cdot \mathbf{u}'' \rangle \rangle + 2 \langle \langle \rho \mathbf{g} \cdot (s_L \mathbf{n}) \rangle \rangle. \quad (4.37)$$

The last two terms on the left hand side describe turbulent transport effects. The production of $\widetilde{G''^2}$ due to turbulence is described by the first term on the right hand side, while the last term describes the destruction of variance either due to kinematic restoration or due to scalar dissipation, depending on the magnitude of the local flamelet curvature. Note that the scalar $\widetilde{G''^2}$ is not advected by the mean flow velocity but by the propagation velocity of the mean flame front position as shown by the second term on the right hand side.

The transport equations for the \tilde{G} , eqn. (4.34), and $\widetilde{G''^2}$, eqn. (4.37), are both only defined at $\tilde{G} = G_0$. An extension into the whole computational domain and flow field is still required and is discussed in the next section.

4.4.2 Modelling closures for \tilde{G} and $\widetilde{G''^2}$

The closure of the equations for \tilde{G} and $\widetilde{G''^2}$ are only briefly discussed in the following; more details are given in [32, 47, 85].

The last term on the left hand side of the equation for the mean flame front position, equation (4.34), is the turbulent flame propagation term expressing the flame propagation by the turbulent burning velocity:

$$\langle \langle \rho s_L(\kappa) \mathbf{n} \rangle \rangle = (\rho s_T) \tilde{\mathbf{n}}. \quad (4.38)$$

In this context $\tilde{\mathbf{n}}$ denotes the normal of the mean flame front, defined in analogy to (4.14) as $\tilde{\mathbf{n}} = -\nabla\tilde{G}/|\nabla\tilde{G}|$. For a closure of the turbulent transport term $\widetilde{\nabla g \mathbf{u}''}$, information from outside of the mean flame front position must not be taken into account due to the level set character of the \tilde{G} field. Therefore the classical approach of gradient diffusion type approach is not feasible. Introducing the curvature of the mean flame front $\tilde{\kappa}$ as $\tilde{\kappa} = \nabla \cdot \tilde{\mathbf{n}}$ the turbulent transport is modelled as a curvature term [32, 85]

$$\widetilde{\nabla g \mathbf{u}''} = D'_t \tilde{\kappa} |\nabla\tilde{G}|. \quad (4.39)$$

Here D'_t is the effective turbulent diffusivity of the curvature term which must be approximated appropriately.

Concerning the closure of the equation for $\widetilde{G''^2}$, the two turbulent transport terms on the left hand side of eqn. (4.37) are modelled together by a mean gradient transport hypothesis approach

$$-\langle \rho \rangle \widetilde{\nabla g'' \cdot \mathbf{u}''} - \langle \langle \rho \nabla g'' \cdot (s_L \mathbf{n}) \rangle \rangle = \nabla_{||} \left(\langle \rho \rangle D_t \nabla_{||} \widetilde{G''^2} \right), \quad (4.40)$$

where the $||$ subscript indicates that only gradient in the mean flame front tangential direction are considered; this is to ensure that only information from the flame front position is taken into account. Similarly, the turbulent production term in the $\widetilde{G''^2}$ -equation is closed by a classical gradient transport assumption as

$$2 \langle \langle \rho \mathbf{g} \cdot \mathbf{u}'' \rangle \rangle = 2 \langle \rho \rangle D_t \left(\nabla\tilde{G} \right)^2, \quad (4.41)$$

where the turbulent diffusivity is related to the turbulent viscosity via the turbulent Schmidt-number Sc_t

$$D_t \equiv \frac{\mu_t}{\rho Sc_t}. \quad (4.42)$$

In principal, the destruction or flame brush reducing term of the $\widetilde{G''^2}$ -equation has to be modelled differently for the corrugated flamelet regime and the thin reaction zone. In the former this term is dominated by kinematic restoration, while in the latter the scalar dissipation rate plays the central role. Following [84], a unified approach for both regimes can be derived which reads

$$2 \langle \langle \rho \mathbf{g} \cdot (s_L \mathbf{n}) \rangle \rangle = -c_s \langle \rho \rangle \widetilde{G''^2} \frac{\varepsilon}{k}, \quad (4.43)$$

where the constant has the value $c_s = 2.0$. Compiling all model closures into (4.34) and (4.37), the transport equation for \tilde{G} and $\widetilde{G''^2}$ become

$$\langle \rho \rangle \frac{\partial \tilde{G}}{\partial t} + \langle \rho \rangle \nabla\tilde{G} \cdot \tilde{\mathbf{u}} = -\langle \rho \rangle D'_t \langle \kappa \rangle |\nabla\tilde{G}| + (\rho_{sT}) |\nabla\tilde{G}|, \quad (4.44)$$

$$\langle \rho \rangle \frac{\partial \widetilde{G''^2}}{\partial t} + \langle \rho \rangle \frac{d\mathbf{x}_f}{dt} \cdot \nabla \widetilde{G''^2} = \nabla_{||} \left(\langle \rho \rangle D_t \nabla_{||} \widetilde{G''^2} \right) + 2 \langle \rho \rangle D_t \left(\nabla\tilde{G} \right)^2 - c_s \langle \rho \rangle \widetilde{G''^2} \frac{\varepsilon}{k}. \quad (4.45)$$

4.4.3 Modelling closure for the turbulent burning velocity

In order to close the transport equation for the \tilde{G} -equation (4.44), an approximation for the turbulent burning velocity is required. According to equation (4.27) the turbulent surface area ratio $\tilde{\sigma}_t$ links the turbulent burning velocity s_T to the laminar burning velocity s_L via

$$s_T = (1 + \tilde{\sigma}_t) s_L.$$

A modelled equation for $\tilde{\sigma}_t$ has been derived by Peters [84], based on the transport equations for k , ε , and $\widetilde{G''^2}$. The resulting model equation for both the corrugated flamelets and the thin reaction zone reads

$$\begin{aligned} \langle \rho \rangle \frac{\partial \tilde{\sigma}_t}{\partial t} + \langle \rho \rangle \tilde{\mathbf{u}} \cdot \nabla \tilde{\sigma}_t &= \nabla_{\parallel} \cdot (\langle \rho \rangle D_t \nabla_{\parallel} \tilde{\sigma}_t) \\ &+ c_0 \langle \rho \rangle \frac{-\widetilde{\mathbf{u}'' \mathbf{u}''} : \nabla \tilde{\mathbf{u}}}{k} \tilde{\sigma}_t + c_1 \langle \rho \rangle \frac{D_t (\nabla \tilde{G})^2}{\widetilde{G''^2}} \tilde{\sigma}_t \\ &- c_2 \langle \rho \rangle \frac{s_L^0 \tilde{\sigma}_t^2}{(\widetilde{G''^2})^{1/2}} - c_3 \langle \rho \rangle \frac{D \tilde{\sigma}_t^3}{\widetilde{G''^2}}. \end{aligned} \quad (4.46)$$

The left hand side represents local change and convection. The first term on the right hand side is the turbulent transport of $\tilde{\sigma}_t$ modelled by a gradient transport assumption. The second term models the production of flame surface area ratio due to velocity gradients of the mean flow, where the constant $c_0 = c_{\varepsilon 1-1} = 0.44$ stems from the modelled ε equation. The last three terms represent turbulent production, kinematic restoration, and scalar dissipation of the flame surface area ratio, respectively. The model constants are summarised in table 4.1.

Considering a steady planar flame, the transient and the convective term on the right hand side, as well as the turbulent transport term on the left hand side of equation (4.46) vanish. Neglecting the production term due to velocity gradients leads to an equilibrium turbulent production, kinematic restoration, and scalar dissipation of the flame surface area ratio. The balance of the three terms leads to a quadratic equation for $\tilde{\sigma}_t$

$$c_1 \frac{D_t (\nabla \tilde{G})^2}{\widetilde{G''^2}} - c_2 \frac{s_L^0 \tilde{\sigma}_t}{(\widetilde{G''^2})^{1/2}} - c_3 \frac{D \tilde{\sigma}_t^2}{\widetilde{G''^2}} u = 0. \quad (4.47)$$

Only the positive root of the previous equation has a physical meaning. The solution of eq. (4.47) however does not account for transient flame development effects. By introducing the ratio ℓ^* between the turbulent flame brush thickness $\ell_{f,t}$ and a turbulent length scale as a measure for the development status of the turbulent flame, in [32] a modified expression for $\tilde{\sigma}_t$ has been derived. As turbulent length scale, the *algebraic flame brush thickness* is employed, which can be derived by considering a steady state solution of equation (4.45). The final expression for $\tilde{\sigma}_t$ reads

$$\tilde{\sigma}_t = -\frac{b_3^2}{4b_1} \sqrt{\frac{3c_\mu c_s}{S c_t} \frac{\ell_{f,t}}{\ell_f} \ell^{*q}} + \sqrt{-\frac{b_3^4}{16b_1^2} \frac{3c_\mu c_s}{S c_t} \frac{\ell_{f,t}}{\ell_f} \ell^{*2q} + \frac{c_s b_3^2}{2s_L \ell_f} \ell_{f,t}^2 \frac{\varepsilon}{k}}, \quad (4.48)$$

| c_1 | c_2 | c_3 | b_1 | b_3 | c_s | c_μ | Sc_t |
|-------|-------|-------|-------|-------|-------|---------|--------|
| 4.63 | 1.01 | 4.63 | 2.0 | 1.0 | 2.0 | 0.09 | 0.7 |

Table 4.1: Model constants for the σ_t -equation [85] and the G -equation model [32].

where the constants are given in table 4.1.

4.5 LES combustion modelling

Technical combustion devices often require rapid mixing and short combustion times, yet must ensure proper flame stabilisation. These conflicting requirements commonly lead to devices characterised by very complicated flow patterns, such as swirling flows, breakdowns of large-scale vortical structures, and recirculation regions. The accuracy required for predictions, for example, of pollutants in such flows typically cannot be achieved using Reynolds-averaged Navier-Stokes (RANS) simulations. Starting the late 1990s, LES as a tool for predictive simulations of turbulent reactive flows has gained a significant interest.

The main reason why LES is thought to provide substantial advantages for modeling turbulent combustion is that the scalar mixing process is of paramount importance in chemical conversion [90]. Non-reactive and reactive system studies show that LES predicts the scalar mixing process and dissipation rates with considerably improved accuracy compared to RANS, especially in complex flows.

Different models have been proposed for LES of premixed turbulent combustion, most of which are variants of the flamelet concept (Colin *et al.* [22], Kim & Menon [52], Pitsch & Duchamp de Lageneste [91]). Other models that have been proposed include the thickened flame model (Colin *et al.* [22]) and the linear eddy model (Chakravarthy & Menon [17]). However, most of the combustion models for LES of turbulent combustion are similar to RANS models and are based on similar modelling assumption.

4.5.1 Regime diagram for LES

The regime diagram used to characterise turbulence/flame interactions in premixed turbulent combustion has already been discussed in section 4.2.1. The different regimes are presented in terms of v'/s_L and ℓ/ℓ_F , where v' and ℓ are the characteristic velocity fluctuation and length scale of the large turbulent scales, and l_F is the laminar flame thickness. All these parameters are physical quantities, independent of the turbulence and combustion models used. The different combustion regimes are distinguished by means of the turbulent Reynolds number Re_t , the Karlovitz number Ka , and the turbulent Damköhler number Da .

In LES, these numbers can be defined based on the characteristic sub-filter quantities

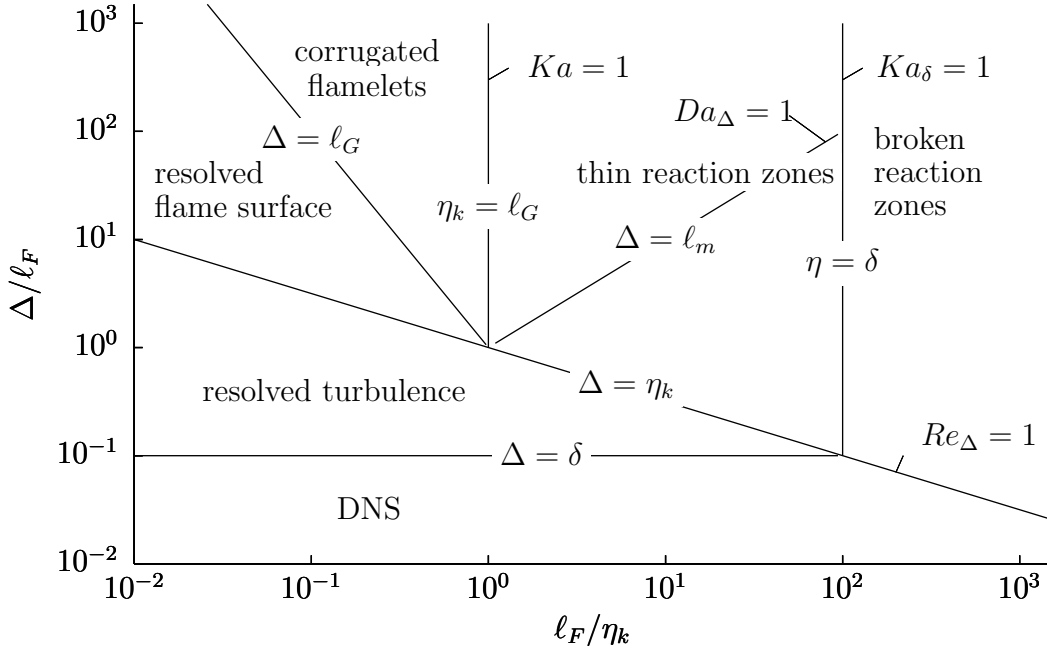


Figure 4.6: Regime diagramme for LES and DNS of premixed turbulent combustion according to Pitsch [89].

as

$$Re_{\Delta} = \frac{u'_{\Delta} \Delta}{s_L \ell_F}, \quad Da_{\Delta} = \frac{s_L \Delta}{u'_{\Delta} \ell_F}, \quad \text{and} \quad Ka = \frac{l_F^2}{\eta_K^2} = \left(\frac{u'_{\Delta} \ell_F}{s_L \Delta} \right)^{1/2}. \quad (4.49)$$

It is important to note that changes in the filter size result in changes of the sub-filter Reynolds and Damköhler numbers, while the Karlovitz number is independent of the filter width. This implies that changes in the filter width proceed at constant values of the Karlovitz number. An LES regime diagram for characterising sub-filter turbulence/flame interactions in premixed turbulent combustion was proposed by Pitsch & Duchamp de Lageneste [91], and recently extended by Pitsch [89]. This diagram is shown in Figure 4.6, which allows to identify the influence of the filter size while clearly distinguishing between changes in the turbulence/chemistry interaction and numerical effects. In contrast to the RANS regime diagrams, Δ/ℓ_F and the (square root of the) Karlovitz number Ka are used as the axes of the diagram, as the latter is independent of the filter size. Thus the effect of changes in filter size can easily be assessed at constant Ka number.

Analogue to the RANS regime diagram, three regimes with essentially different interactions of turbulence and chemistry can be identified: the corrugated flamelet regime, the thin reaction zones regime, and the broken reaction zones regime, which already have been discussed in section 4.2.1.

The effect of changing the LES filter width can be assessed by starting from any one

of these regimes at large Δ/ℓ_F . With decreasing filter width, the sub-filter Reynolds number, Re_Δ , eventually becomes smaller than one, which implies that the filter size is smaller than the Kolmogorov scale. Consequently no sub-filter modelling for the turbulence is required and the turbulent structures are fully resolved, which corresponds to a DNS of the flow. However, the entire flame including the reaction zone is only resolved if the filter width is smaller than the inner layer width, i.e. $\Delta < \delta$; in this case a flame DNS is performed.

In the corrugated flamelets regime, if the filter is decreased below the Gibson scale ℓ_G , which is the smallest scale of the sub-filter flame-front wrinkling, the flame-front wrinkling is completely resolved. In the corrugated flamelet regime, where the flame structure is laminar, the entire flame remains on the sub-filter scale, if Δ/ℓ_F is larger than one.

In the thin reaction zones regime, the preheat region is broadened by the turbulence. Peters [84] estimated the broadened flame thickness from the assumption that the timescale of the turbulent transport in the preheat zone has to be equal to the chemical timescale, which for laminar flames leads to the burning velocity scaling given in the beginning of this section. From this, the ratio of the broadened flame thickness ℓ_m and the filter size can be estimated as [89]

$$\frac{\ell_m}{\Delta} = \left(\frac{u' \ell_F}{s_L \Delta} \right)^{3/2} = Ka \frac{\ell_F}{\Delta} = Da_\Delta^{-3/2}.$$

Hence, the flame is entirely on the sub-filter scale as long as $Da_\Delta > 1$, and is partly re-solved otherwise. It is important to realise that the turbulence quantities, especially u'_Δ , and hence most of the non-dimensional numbers used to characterise the flame/turbulence interactions, are fluctuating quantities and can significantly change in space and time.

4.5.2 Thickened flame model

A simplistic approach based on the theories of laminar flames is the (artificially) thickened flame approach. The flame speed s_L and the flame thickness ℓ_f can be expressed as

$$s_L \sim \sqrt{D_0 B}, \quad \ell_f \sim \frac{D_0}{s_L} = \sqrt{\frac{D_0}{B}},$$

where B denotes the rate-coefficient and D_0 is the thermal diffusivity, see equations (4.3)–(4.5) and section 4.1.1. Increasing the thermal diffusivity D_0 by a constant factor α and decreasing the pre-exponential constant B by the same factor the flame thickness is increased while the (laminar) flame speed is unaffected. By adopting the factor α , the thickened flame with increased thickness of $\alpha \ell_f$ can be resolved on a given mesh. However, this manipulation leads to a change in the interaction between turbulence and chemistry as indicated by the Damköhler number Da , see equation (4.19) and 4.2.1,

which is decreased by the factor α . Thus the physics of flame propagation is severely modified from a transport-controlled combustion mode towards a chemically dominated progression [91] which does not reflect the underlying physical and chemical processes. In order to compensate these effects correction factors based on DNS, referred to as efficiency functions, have been developed [22]. A dynamic version for the determination of the multiplicative constant has been proposed in [18].

4.5.3 Progress variable approaches

Filtering of the transport equation for the progress variable c leads to a balance equation for the filtered progress variable \tilde{c} , which is given by [92]

$$\begin{aligned} \frac{\partial \bar{\rho} \tilde{c}}{\partial t} + \frac{\partial \bar{\rho}(\tilde{u}_i \tilde{c})}{\partial x_i} + \overbrace{\frac{\partial \bar{\rho}(\tilde{u}_i \tilde{c} - \tilde{u}_i \tilde{c})}{\partial x_i}}^{\text{sub-filter scale transport}} \\ = \underbrace{\frac{\partial}{\partial x_k} \left(\overline{\rho D_c \frac{\partial c}{\partial x_k}} \right)}_{\text{molecular diffusion}} + \underbrace{\bar{\dot{\omega}}_c}_{\text{filtered reaction rate}} = \overline{\rho s_d |\nabla c|}. \end{aligned} \quad (4.50)$$

The flame front displacement term $\overline{\rho s_d |\nabla c|}$ can be modelled as [11]

$$\overline{\rho s_d |\nabla c|} \approx \rho_u s_L \bar{\Sigma}.$$

Here $\bar{\Sigma}$ represents the sub-filter scale flame surface density. Denoting the ratio between the sub-filter scale flame surface and its projection into the flame propagation direction by Ξ , $\bar{\Sigma}$ can be approximated as

$$\bar{\Sigma} = \Xi |\nabla c|.$$

In order to close the equations, models of $\bar{\Sigma}$ and Ξ are required, most of which are formally identical to those developed in the RANS context. A detailed discussion of different modelling approaches are given in [99]. However, the modelling approaches employed to close equation (4.50) make extensive use of correction of efficiency functions whose form stems from *ad-hoc* assumption and whose coefficient have been tuned by means of DNS data.

4.5.4 Level-set formulation for LES

As discussed in section 4.4 and previously pointed out by Peters [85] and Oberlack [80], for the derivation of a G -equation describing the ensemble or time-averaged flame location, the traditional averaging techniques cannot be employed. As the G -field has physical significance only $G = G_0$, only the G_0 iso-surface may be of relevance during the averaging procedure, while the remaining G -field, which can be arbitrarily defined,

must not be employed. Instead, an averaging procedure based on the probability density function of finding $G = G_0$ has been proposed by Peters [85], and extended by Oberlack [80].

Similar, in LES the classical filtering approach and the filter-kernels employed for filtering the velocity and scalar fields cannot be used to obtain a filtered G -equation. Hence a filter kernel is required that only employs information from the instantaneously resolved flame surface. Pitsch [89] has developed an averaging technique which is based on a parametric representation of the flame surface given by

$$\mathbf{x}_f = \mathbf{x}_f(\mathbf{\Lambda}, t)$$

where $\mathbf{\Lambda} = (\lambda, \mu)$ are curvilinear coordinates along the flame surface. The essential step is the introduction of the spatial filter $\mathbf{H}(\mathbf{\Lambda} - \mathbf{\Lambda}', t)$, which moves along the G_0 iso-surface. This filter function differs substantially from those conventionally applied filter kernel for scalar quantities as the coordinates employed in the filter function are flame surface coordinates. The spatial filtering operation for the definition of the filtered flame front position can then be defined as

$$\bar{\mathbf{x}}_f(\mathbf{\Lambda}, t) = \int_F \mathbf{x}_f(\mathbf{\Lambda}', t) \mathbf{H}(\mathbf{\Lambda} - \mathbf{\Lambda}', t) d\mathbf{\Lambda}'. \quad (4.51)$$

which is sketched in figure 4.7 for the two dimensional case. The filtering operation (4.51) yields a corresponding filtered flame front position $\bar{\mathbf{x}}_f(\mathbf{\Lambda})$ for each point $\mathbf{x}_f(\mathbf{\Lambda})$ on the instantaneous flame front.

The application of the spatial filter \mathbf{H} leads to the transport equation for filtered flame front location¹ \tilde{G}_0 . This transport equation reads [88, 89, 91]

$$\bar{\rho} \frac{\partial \tilde{G}}{\partial t} + \bar{\rho} \tilde{\mathbf{u}} \cdot \nabla \tilde{G} + \nabla \cdot (\bar{\rho} \tilde{\mathbf{u}}' \tilde{G}') = (\rho s_L) \overline{|\nabla G|} - (\rho D) \overline{\kappa |\nabla G|}.$$

The line of arguments and modelling for the closure of the previous equation are similar to the ones employed by Peters [84, 85] in the context of statistical modelling. This can be attributed to the assumption that the flame is completely on the sub-filter scale. Accordingly the modelled equations exhibit a structural similarity to RANS context, see equation (4.44). Following [91] the \tilde{G} -equation reads

$$\bar{\rho} \frac{\partial \tilde{G}}{\partial t} + \bar{\rho} \tilde{\mathbf{u}} \cdot \nabla \tilde{G} = \bar{\rho} s_t |\nabla \tilde{G}| - \bar{\rho} D_t \tilde{\kappa} |\nabla \tilde{G}|. \quad (4.52)$$

$$\bar{\rho} s_t |\nabla \tilde{G}| = (\rho s_L) \bar{\sigma}_t \quad (4.53)$$

where s_t denotes the turbulent, sub-filter burning velocity and $\bar{\sigma}_t$ is the sub-filter flame surface area ratio analogous to the RANS definitions employed in section 4.4; additional details on closure and modelling assumptions are given in [88].

¹As mentioned in [89] \tilde{G} is not defined as the filtered instantaneous G -field but as a level set representation of the filtered flame front location.

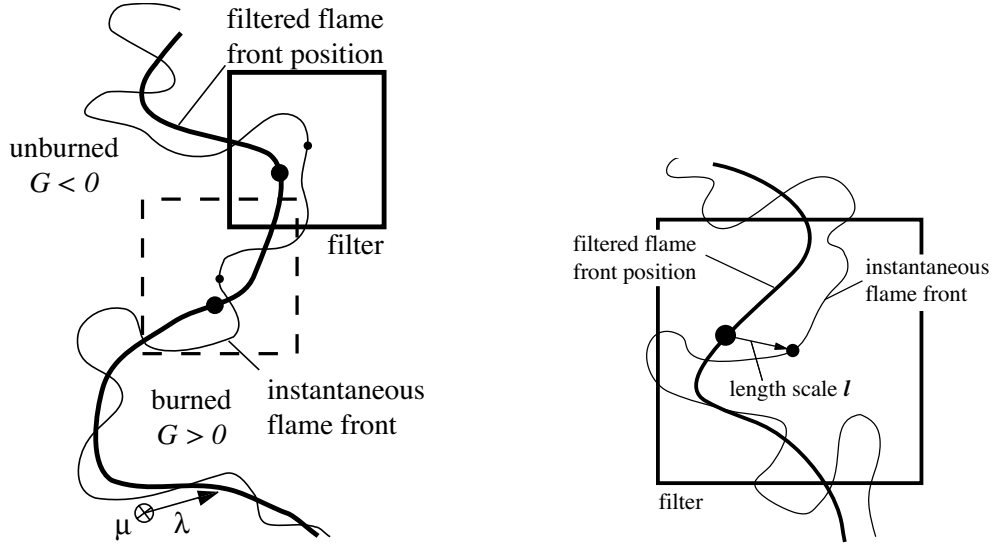


Figure 4.7: Instantaneous and filtered flame front position. The rectangle indicates the filter box, which is attached to the instantaneous front at the location indicated by the small circle. The large circle indicates the corresponding filtered flame front position. The dashed rectangle shows the filter at a different λ -position [89].

4.6 VLES/ G -equation coupling

The G -equation model has been formulated and discussed in the RANS and LES context in sections 4.4 and 4.5.4 respectively. Similar to the transport equations for the turbulent kinetic energy k and the turbulent sub-filter kinetic energy $k_r = q^2$, the structure of both the RANS and LES model equations are identical, see equations (4.44) and (4.52) respectively. This affinity motivates the coupling of the hybrid two level model, section 3.5.2, to the G -equation approach for the modelling of premixed turbulent combustion and renders the coupling straight forward. Moreover, a simple scaling analysis demonstrates that the model equations, formulated for the RANS approach, can be employed in the VLES context if the turbulent diffusivity, the integral turbulent kinetic energy, and the integral turbulent dissipation are replaced by the corresponding sub-filter quantities, i.e. turbulent sub-filter diffusivity, the sub-filter kinetic energy, and the sub-filter dissipation, respectively. In that case, the integral turbulent burning velocity needs to be understood as a sub-filter burning velocity and the variance as a the sub-filter variance.

Based on (4.45) and neglecting temporal and spatial derivatives, a steady-state algebraic solution for $\widetilde{G''^2}$ can easily be derived [32] as

$$\widetilde{G''^2} = \frac{2}{c_s} D_t (\nabla \widetilde{G})^2 \frac{k}{\varepsilon} \sim \ell_t^2,$$

where $D_t \sim k^2/\varepsilon$, $\ell_t \sim k^{3/2}/\varepsilon$ and the distance constrained $|\widetilde{G}| = 1$ has been used.

Replacing the RANS viscosity with the sub-filter scale viscosity given by $\nu_t = C_k \sqrt{k_r} \bar{\Delta}$ and correspondingly the sub-filter dissipation via $\varepsilon_r = C_\varepsilon \frac{k_r^{3/2}}{\bar{\Delta}}$, a similar estimation can be made for the LES mode of the hybrid model, which directly leads for the filtered variance to

$$\overline{G''^2} \sim \bar{\Delta}^2.$$

The identical result is obtained for the RANS approach in the limit $\ell_t \rightarrow \bar{\Delta}$.

5 Numerics

In order to describe the relevant spatial structures of a (turbulent) flow the spatial discretisation of the conservation equations is of fundamental importance. Considering unsteady phenomena, and here especially turbulent flows, the correct description of the evolution of the flow fields can only be achieved by appropriate temporal and spatial schemes. While for laminar flows the numerical dissipation due to the employed discretisation scheme has a limited influence onto the results, for turbulent flows the choice of numerical scheme has a significant impact on the quality, accuracy, and reliability of the numerical solution [15]. The influence of the numerics on the development of homogeneous isotropic turbulence is demonstrated in section 6.1 for both temporal and spatial discretisation schemes and resolution, i.e. time step size and grid spacing. Therefore to assess the results of the numerical simulation of a turbulent flow, knowledge of the underlying numerical schemes is of essential importance.

The present section discusses the fundamental principle for the transformation of the continuous differential equations governing the conservation of mass, momentum, and energy as presented in section 2.1 into a discrete formulation by means of the Finite Volume Method as employed by the AC-FLUX code. Starting point is the generalised form of the conservation equations, which is integrated over a finite time and finite volume representing a discrete time step and a computational cell respectively. The approximations of the obtained integrals require the values of the dependent variables at locations other than computational nodes (cell centres); these unknowns are formulated depending on *known* values at the cell centres. This results in a sparse linear equation system of form $\mathbf{Ax} = \mathbf{b}$ with \mathbf{x} representing the (eventually sought-after) cell-centre values.

The following discussion focuses on the derivation of the discrete formulation of the conservation equations and will not explicitly formulate the matrix coefficients but stop when the individual terms have been formulated in terms of cell centred variables. More details can be found in [35] as well as in classical text book [34, 81, 124].

The solution of the level-set equation is discussed in section 5.3.

5.1 Discretisation of the conservation equations

The starting point is the set of basic conservations equations (coupled pde's) introduced in Section 2.1. The basic derivation sequence is as follows. For each individual pde:

1. integrate the pde over a discrete time step and a control volume corresponding to a finite-volume cell; this gives rise to terms to be evaluated at the bounding surfaces of the control volume (cell faces);

2. introduce discrete approximations to derivatives and interpolation rules for evaluating quantities at locations other than their primary locations (e.g., for obtaining cell–face values from cell–centre values);
3. organise the terms in the discretised volume–integrated form of each individual pde into a form suitable for numerical computation.

Then for the coupled set of pde’s a strategy for advancing the coupled set of nonlinear pde’s over a computational time-step is required. Here, AC-FLUX uses an iterative segregated pressure–based approach discussed in section 5.2.

5.1.1 Development for a single pde

The conservation equation for a general scalar ϕ , or more exact, for the Favre-average of a general scalar $\tilde{\phi}$ can readily be deduced from the principal pde’s given in section 2.1; here ϕ represents velocity u_i , internal energy e , enthalpy h , mass fraction Y_α , turbulent kinetic energy k , or turbulent dissipation rate ε . The differential form of the general conservation equation is given below employing index notation, eq. (5.1a), as well as vector notation, eq. (5.1b).

$$\underbrace{\frac{\partial(\langle\rho\rangle\tilde{\phi})}{\partial t}}_{\text{local change}} + \underbrace{\frac{\partial(\langle\rho\rangle\tilde{u}_i\tilde{\phi})}{\partial x_i}}_{\text{convective term}} = \underbrace{\frac{\partial}{\partial x_i}\left(\Gamma_{\tilde{\phi}}\frac{\partial\tilde{\phi}}{\partial x_i}\right)}_{\text{diffusive term}} + \underbrace{S_{\tilde{\phi}}}_{\text{source term}} \quad (5.1a)$$

$$\frac{\partial(\langle\rho\rangle\tilde{\phi})}{\partial t} + \nabla \cdot (\langle\rho\rangle\tilde{\mathbf{u}}\tilde{\phi}) = \nabla \cdot (\Gamma_{\tilde{\phi}}\nabla^T\tilde{\phi}) + S_{\tilde{\phi}} \quad (5.1b)$$

Here $\Gamma_{\tilde{\phi}}$ is the diffusion coefficient associated with ϕ , and $S_{\tilde{\phi}}$ represents the remaining terms of the parent equations considered as ‘sources’; u_i represents the relative velocity between the fluid and the local coordinate velocity¹. For ease of notation a simplified notation is applied in the following omitting the Favre-averaging ($\tilde{\cdot}$) and mean value symbols ($\langle\cdot\rangle$) as well as the index of $\Gamma_{\tilde{\phi}}$.

In the Finite Volume framework these equations are integrated over a finite volume Ω (cell) with surface $\partial\Omega = A$ around some point P (cell centre) within Ω . Employing the Gauss theorem for transforming the volume integral into a surface integral leads to the following form:

$$\frac{\partial}{\partial t} \int_{\Omega} (\rho\phi) dV + \int_A (\rho\mathbf{u}\phi) d\mathbf{S} = \int_A (\Gamma \text{grad } \phi) d\mathbf{S} + \int_{\Omega} S_{\phi} dV. \quad (5.2)$$

¹For simplicity’s sake the local coordinate velocity will not be considered here.

The previous equations are valid for an arbitrary time varying volume $\Omega = V_P$ with surface $A = A_P$ around some point P in the field. Recall that \mathbf{u} thus denotes the relative velocity between the fluid and the (potentially moving) surface A_P . If the volume V_P represents the volume of a computational cell and A_P the corresponding overall surface of that cell where the surface of the cell consists of considerably plane cell faces with cell face area S_f ($f = 1, \dots, \text{number of cell faces}$), i.e. $A_P = \sum_f S_f$, then equation (5.2) becomes

$$\underbrace{\frac{\partial}{\partial t} \int_{V_P} (\rho\phi) dV}_{\text{temporal change}} + \underbrace{\sum_f \int_{S_f} (\rho\mathbf{u}\phi) d\mathbf{S}}_{:=\sum_f C_f \text{ (convective fluxes)}} = \underbrace{\sum_f \int_{S_f} (\Gamma \text{ grad } \phi) d\mathbf{S}}_{:=\sum_f D_f \text{ (diffusive fluxes)}} + \int_{V_P} S_\phi dV.$$

The first term on the left hand side describes the local change of $\rho\phi$ in the control volume. In a source free environment ($S_\phi = 0$), the change is due to the convective and diffusive flux across the surface of the control volume, denoted by C_f and D_f respectively. These fluxes need to be evaluated at the cell faces. The approximations of these terms, i.e. the temporal derivative and the fluxes C_f and D_f , are discussed in the following subsections.

Temporal discretisation To be faithful to the nature of time, essentially all methods commonly used advance in time in a step-by-step or “marching” method; here based on value of the dependent variable ϕ at some time t_n the value at the next time level $t_{n+1} = t_n + \Delta t$ is sought after, where Δt is a small time increment. These methods are similar to the ones used for solving initial value problems. In the context of commercial and industrial applicability, implicit time integration schemes² are usually employed. Restricting the discussion to *two-level methods*, involving the values of the unknown at two time steps, the most popular choices are backward or implicit Euler, and the Crank-Nicolson scheme. Characteristic for implicit schemes is the requirement of the value of $\phi(t)$ at some point other than $t = t_n$ at which the solution is known. Therefore these approaches lead to implicit systems which can only be solved iteratively.

The conservation equation for the general scalar ϕ can be cast into the form of a first order differential equation, i.e. as an initial value problem of the following form:

$$\frac{d\phi}{dt} = f(t, \phi(t)), \quad \phi(t_n) = \phi^n. \quad (5.3)$$

Here, f indicates the convective and diffusive transport as well as source terms; t_n indicates some initial point in time where $\phi(t_n)$ is known. Integration of equation (5.3) over the time interval $[t_n, t_{n+1}]$ leads to

$$\int_{t_n}^{t_{n+1}} \frac{d\phi}{dt} dt = \phi^{n+1} - \phi^n = \int_{t_n}^{t_{n+1}} f(t, \phi(t)) dt. \quad (5.4)$$

²The popularity of implicit scheme stems from the fact that they generally have superior stability properties and less restrictive constraints on the size of the maximal allowed step size.

This integration is *exact*, but the right side cannot be evaluated without knowledge of the solution, thus some approximation of the integral is necessary. If the integral on the right hand side of equation (5.4) is estimated via final point t_{n+1} the *implicit* or *backwards Euler* method (5.5) is obtained, which is of first order in time³.

$$\phi^{n+1} = \phi^n + f(t_{n+1}, \phi^{n+1})\Delta t \quad (5.5)$$

Using a straight line interpolation between the initial and final points for construction an approximation to the integral yields the trapezoid rule or Crank-Nicolson scheme, eq. (5.6).

$$\phi^{n+1} = \phi^n + \frac{1}{2} (f(t_n, \phi^n) + f(t_{n+1}, \phi^{n+1})\Delta t) \quad (5.6)$$

As all explicit scheme the semi-explicit Crank-Nicolson scheme is only conditionally stable, which means that the size of the time step is limited by geometrical and physical properties (CFL number⁴). On the other hand, the fully implicit scheme is unconditionally stable thus allowing (in principle) arbitrary step sizes. Although numerically more expensive the stability properties of the implicit Euler scheme makes it extremely attractive for the simulation of practical flows in complex geometries. The dependency of the explicit scheme on time step restriction due to CFL restrictions, i.e. indirectly due to the mesh spacing, lead to a significant increase in computational cost, especially when the mesh quality is low. On the other hand, when considering the case of LES, besides the numerical time restrictions, the time scale of the resolved turbulent structures limit the maximal time-step size. Therefore in the field of RANS, implicit time integration is usually favoured, while for LES (and DNS) explicit schemes are employed [15]. In section 6.1, the influence of the numerical scheme of the evolution of the flow field is demonstrated.

5.1.2 General form of the discretised equations

As discussed in the previous section, in AC-FLUX's finite-volume formulation, the governing pde's are integrated over a control volume that corresponds to a computational cell. Considering pure hexahedral meshes, each computational cell has six principal neighbours (one through each face). The linearised discretised equation for a cell-centred dependent variable ϕ then can be written in the following form that is consistent with the standard notations used in the literature:

$$A_{0,\phi}\phi_P - \sum_f A_{f,\phi}\phi_f = S_{u,\phi} + S_{p,\phi}\phi. \quad (5.7)$$

³The order of a numerical scheme is a measure of the error reduction when increasing the resolution; first order implies that when the time step is reduced by a factor of 2, the same is valid for the numerical error, while second order implies that the error is reduced by a factor of 4; note that this only refers to the error reduction, but not to the absolute values; thus a low order scheme can, for a given resolution, be more exact than a high order scheme.

⁴CFL-number: Courant-Friedrich-Levy number, ratio of the numerical time-step to the convective time scale: $CFL = |u|\Delta t/\Delta x$.

The diagonal coefficients $A_{0\phi}$, off-diagonal coefficients $A_{1\phi} \rightarrow A_{6\phi}$, and source term components $S_{u\phi}$ and $S_{p\phi}$ are independent of ϕ (the equations are linear). This structure accommodates cases where one or more cell faces lie on boundaries; in that case, the corresponding neighbour value ϕ_f is a boundary-face value rather than a cell-centre value. A conventional source-term linearisation has been employed, where the total source term S_ϕ is decomposed into two contributions:

$$S_\phi = S_{u\phi} + S_{p\phi}\phi, \quad (5.8)$$

where $S_{p\phi}$ is strictly *non-positive*. $S_{p\phi}$ then can be combined with the diagonal coefficient $A_{0\phi}$ to increase the robustness of the linear system solution procedure by increasing the diagonal dominance of the matrix:

$$A_{p\phi} \equiv A_{0\phi} - S_{p\phi}. \quad (5.9)$$

Other benefits of source-term linearisation are discussed by Patankar [81]. The general form of the linearised discretised equation is then:

$$A_{p\phi}\phi_p - \sum_{f=1}^6 A_{f\phi}\phi_f = S_{u\phi}. \quad (5.10)$$

The coefficient matrix is sparse (seven non-zero elements per row); it is symmetric in the case of the pressure correction equation and non-symmetric in general for the other equations. It is not necessarily diagonally dominant. In cases where a cell has more than six neighbour cells and/or faces (adaptive meshes, sliding interfaces) additional non-zero entries appear in the coefficient matrix; these are dealt with in a fully implicit manner in the linear equation solvers. Robust preconditioned conjugate gradient (for symmetric systems) or bi-conjugate gradient (for non-symmetric systems) iterative linear equation solvers are used to solve the resulting implicit sparse linear equation sets.

5.2 Computation of the pressure field

AC-FLUX employs an iteratively implicit pressure-based sequential (segregated) solution procedure to solve the coupled system of governing pde's presented in Section 2.1. *Sequential* or *segregated* means that the pde's are solved sequentially rather than simultaneously; coupling is achieved via an iterative updating procedure. The procedure accommodates incompressible and/or compressible flows and steady and/or transient flows. It is applicable for essentially arbitrary Mach numbers, although for Mach numbers much greater than unity the efficiency of the approach decreases significantly. AC-FLUX's pressure algorithm is patterned after SIMPLE (Semi-Implicit Method for Pressure-Linked Equations, [81]) and PISO (Pressure-Implicit Split Operator, [49]). PISO originally was conceived as a predictor-corrector method to be used with a fixed

number of passes through the equations on each time-step; however, a *pure* PISO method generally is neither sufficiently efficient nor sufficiently robust for the highly distorted computational meshes and complex three-dimensional time-dependent flows that characterise practical engineering applications. The algorithm used in AC-FLUX can be thought of as a modified PISO scheme where the numbers of outer and inner iterations both are variable; the algorithm reduces to a SIMPLE-like method in the case of a single outer loop (momentum predictor) and a single inner loop (pressure/velocity corrector) per time-step.

The following subsection 5.2.1 provides a general description of AC-FLUX's pressure algorithm; details can be found in [35].

5.2.1 Pressure/velocity coupling

The essential steps in the pressure/momentum/continuity coupling to advance the solution over one computational time-step are:

1. Momentum predictor – compute a new velocity field using the current pressure field; this velocity field does not satisfy continuity.
2. Pressure/velocity correctors – compute corrections to the pressure and velocity fields to enforce continuity.

The momentum predictor and pressure corrector each require the solution of a sparse implicit linear system that corresponds to a linearised discretised form of the governing pde; the velocity corrector is explicit. Equations for additional quantities (e.g., internal energy/enthalpy, species) may be included in each pressure/velocity corrector step to maintain tight coupling among the equations. At the end of the pressure/velocity corrections, equations requiring a lesser degree of coupling are solved (e.g., turbulence model equations). The process then is repeated as necessary, starting from the momentum predictor, to obtain a converged solution for the current time-step or global iteration.

Three levels of iteration thus are employed on each time-step (each global iteration for a steady solution algorithm): an *outer loop* or outer iteration, an *inner loop* or inner iteration, and iterations within the linear equation solvers. An outer iteration corresponds to a momentum predictor step and an inner iteration corresponds to a pressure/velocity corrector step. The basic sequence is displayed in Figure 5.1.

5.3 Solution of the G -model equations

The solution of the G -equation model is based on the Level Set method, a technique which can be used to describe the position of geometrical interfaces in space and their evolution in time. A thorough introduction into the field of Level Set methods and related topics can be found in [109]. In the present work, the implementation by Ewald [32]

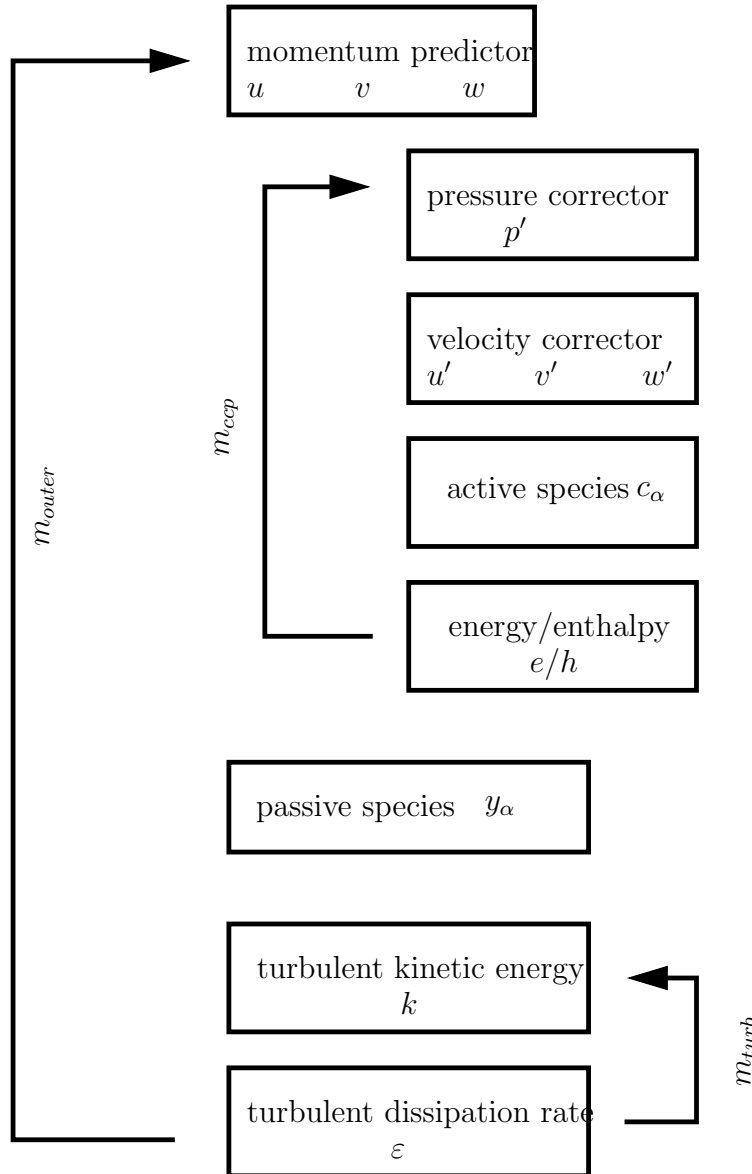


Figure 5.1: A schematic flowchart illustrating three levels of iteration. This flowchart corresponds to a compressible case (internal energy/enthalpy equation included in the inner iterations) using an energy/enthalpy predictor (versus explicit corrector) for each inner iteration (adopted from [35]).

has been employed and adopted in co-operation with the original author for the VLES model approach.

6 Application

6.1 Homogeneous isotropic turbulence

Homogeneous isotropic turbulence (HIT) represents one of the most important as well as fundamental turbulent flow configurations, especially from a theoretical point of view. Numerous theoretical, experimental and numerical studies, cf. [1, 54, 103, 123], have been performed in order to develop an improved understanding of turbulence and turbulent processes.

In this section this basic flow configuration is employed as a reference case for analysing and evaluating the numerical properties on the employed CFD code and to study the influence of numerical parameter and algorithms, necessary for the simulation of the processes of an internal combustion engine. Additionally the initialisation strategies for the generation of an approximate turbulent flow field as discussed in section 3.6 are evaluated and compared.

The structure of the present section is the following. In the first part (6.1.1) a critical comparison of initialisation strategies as discussed is made. The second part discusses the numerical properties of the employed CFD code, analysing the influence of numerical diffusivity, comparing the numerical to the viscous dissipation, i.e. appraise the spatial discretisation schemes; the finishing two sections contain a single time step study for assessing the quality and influence of temporal discretisation schemes, and finally the remapping/interpolation of the initial flow field onto meshes of different mesh resolutions is analysed.

6.1.1 Comparison of initialisation strategies

The discussion of the properties and behaviour of the Lorenz equations, eqs. (3.1)- (3.3), revealed the significance of the choice of initial condition for the subsequent solution. While in the context of RANS the specification of the integral turbulent kinetic energy \tilde{k} and the dissipation rate $\tilde{\epsilon}$ (or alternatively the integral length scale ℓ_t) is sufficient to characterise the turbulence of the flow field, for the large eddy simulation approach appropriate turbulent velocity fluctuations need to be imposed onto the mean field.

For the initialisation of homogeneous isotropic turbulence three different strategies have been discussed in section 3.6, namely (a) the Fourier transform based approach, (b) the initialisation based on a diffusion process (artificial turbulence), and (c) the approach based on truncated Fourier series (synthesised turbulence). In the following these approaches are evaluated with respect to and special focus on the general applicability.

The homogenous isotropic turbulence is initialised on a cubical domain. The edge length of the domain is $L = 32$ mm, thus the smallest resolvable wave length κ_{min} of the turbulent spectrum is given by $\kappa_{min} = 2\pi/L = 196.35m^{-1}$. On the other end of the

| | |
|-------------------------------------|--|
| pressure p | $1.013 \cdot 10^5$ Pa |
| temperature T | 350 K |
| spectrum type | von Kàrmàn-Pao spectrum |
| turbulent velocity scale u' | 15.0 m/s |
| most energetic length scale l_e | $10.0 \cdot 10^{-3}$ m |
| most dissipative length scale l_d | $1.05 \cdot 10^{-5}$ m |
| turbulent dissipation ε | $6.75 \cdot 10^5$ m ² /s ³ |
| density ρ | 1.881 kg/m ³ |
| dynamic viscosity μ | $1519.6 \cdot 10^{-6}$ kg/ms |
| (kinematic viscosity ν) | $(8.0787 \cdot 10^{-4}$ m ² /s) |

Table 6.1: Initial condition for the initialisation of homogeneous isotropic turbulence.

spectrum, the largest resolvable wave number κ_{max} is determined by the mesh spacing via $\kappa_{max} = 2\pi/\Delta x$ where Δx denotes the grid spacing. Three Cartesian equidistant meshes with increasing resolution are used leading to the mesh cut-off wave numbers of $\kappa_{max} = 3142$ 1/m, 6283 1/m, and 12566 1/m as given in the last column of table 6.2. This wave numbers correspond to the *Nyquist frequency* of the mesh, which can be regarded as the cut-off wave number of an implicit sharp spectral filter. Cyclic boundary conditions are used for each pair of opposite faces of the computational domain. The application of the inverse Fourier transformation approach leads to the requirement and is the motivation of the utilisation of Cartesian equidistant meshes.

The initialisation of the turbulent velocity field is based on the parameters as summarised in table 6.1; these settings are analogue to those employed in [113] and have been employed in the framework of the European project LESSCO2¹.

| | no of cells | cell size | mesh cut off |
|-----------------------|-------------------------------------|-----------|--------------|
| mesh 1 | $32^3 = 32\,768$ | 1.00 mm | 3142 1/m |
| mesh 2 | $64^3 = 262\,144$ | 0.50 mm | 6283 1/m |
| mesh 3 | $96^3 = 884\,736$ | 0.25 mm | 12566 1/m |
| geometrical dimension | 32 mm \times 32 mm \times 32 mm | | |

Table 6.2: Mesh parameter for the HIT studies.

¹These settings are inconsistent with respect to the Kolmogorov length scale (most dissipative scale) and turbulent dissipation; based on the values for the turbulent dissipation and kinematic viscosity given in table 6.1, a Kolmogorov length of $\eta = 1.672 \cdot 10^{-4}$ m²/s³ is obtained; the chosen values were taken in order to be able to compare the results with project partners during the LESSCO2 project; the impact of the incorrectness ought to lead to negligible differences.

Spatial inverse Fourier transform based initialisation. Following [12] the inverse Fourier transform based initialisation is based on a von Kàrmàn-Pao spectrum of the form

$$E(\kappa) = \frac{1.5u'^5}{\varepsilon} \frac{(\kappa/\kappa_e)^4}{[1 + (\kappa/\kappa_e)^2]^{17/6}} \exp[-1.5\alpha(\kappa/\kappa_\eta)^{4/3}] \quad (6.1)$$

with $\alpha = 1.5$. The initialised flow fields are afterwards analysed by means of Fourier transform yielding the spectra shown in figure 6.1; the prescribed model spectra of equation (6.1) is additionally given as reference.

The influence of the mesh onto the resolvable scales is clearly visible. The contributions to the turbulent spectrum beyond the mesh cut-off wave length κ_c are suppressed as the corresponding small scale structures cannot be represented on the employed meshes. The cut-off wave length κ_c of the coarsest mesh and, due to the bisection of the mesh width, $2\kappa_c$ of mesh 2 are indicated by vertical lines. Up to the corresponding mesh cut-off all spectra collapse. This indicates that the large scale structures corresponding to small wave numbers are represented equally well on all meshes. However, while for the large wave numbers the prescribed and initialised spectra coincide a slight deviation in the small wave number region is noticeable; the two regions are separated by the maximum of the spectra, i.e. referring to physical space the integral length scales.

The CPU requirements for the initialisation of the velocity fluctuation based in the inverse Fourier transformation is given in table 6.3. Due to the high efficiency of the implementation² the CPU time for the Fourier transformations is small compared to the remaining setup and analysis operations; for increasing mesh sizes the ratio of initialisation CPU time to total CPU is even strongly decreasing.

Diffusion process. While the inverse Fourier transform requires the usage of equidistant Cartesian grids the application of the diffusion process based approach, section 3.6.2, does in principle not pose any restriction onto the numerical mesh and the geometry. Briefly sketched, the general procedure is the following. The velocity field is initialised with uniformly distributed random numbers in the interval $[-0.5 \dots 0.5]$ (white noise). The diffusion process is realised by solving the momentum equations only omitting the pressure correction step of the PISO algorithm; as the AC-FLUX code employs a deferred convective correction approach [34, 35] the numerical treatment of the diffusive and convective term does not allow for decoupling of the two; however as continuity is not enforced via the pressure correction step there is no influence of convection onto the spectra [112]. The time step for the diffusion process has been $\Delta t = 10^{-6}s$. The fluid properties as specified in table 6.1 have been employed.

For the evaluation of the diffusion approach only the coarse mesh (32^3) was employed. As listed in table 6.3 the CPU requirements on a P4/3GHz machine has been approximately 24 h, but could be reduced by optimising the time step size towards large time-

²The employed algorithms is based on subroutines originally developed for the AVBP code at IFP and CERFACS [12].

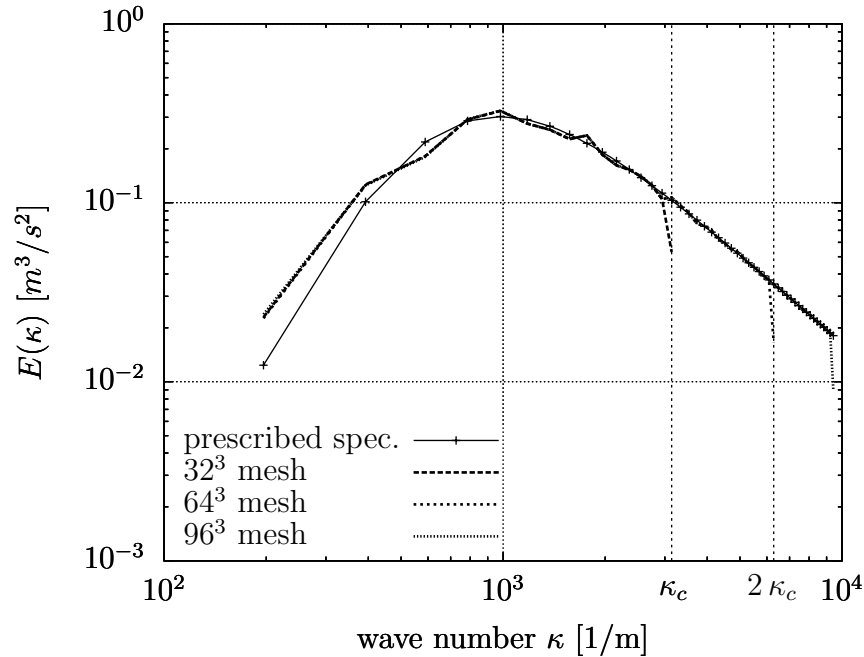


Figure 6.1: Comparison of initial spectra based on Fourier transform on different meshes; k_c refers to the mesh cut-off wave length of the coarsest grid; the mesh cut-off of the finest mesh is not shown.

steps. The temporal integration has been performed using both the standard implicit Euler and Crank-Nicolson scheme, while for the spatial discretisation for the diffusive term the standard second order central differencing scheme has been employed [35]. In order to achieve the same turbulent structure, as characterised by the integral length, the diffusion time t_{diff} for the process has been determined via equation (3.104) as $t_{\text{diff}} \approx 20$ ms

The development of the turbulent spectra is shown in figure 6.2 for both temporal discretisation schemes with the second order Crank-Nicolson scheme on the left and the implicit Euler scheme on the right hand side. The effect of the viscous dissipation on the the spectra is clearly visible. As postulated in section 3.6.2, energy is withdrawn from the small scales near the cut-off while the large(r) scales are rather much unaffected. This removal of kinetic energy leads to the desired deformation of the turbulent spectrum.

The influence of the temporal integration scheme is clearly visible in figure 6.2; for illustration purpose and as reference a line with the $-5/3$ -inclination of the Kolmogorov spectrum is given. The application of the implicit Euler scheme causes a too excessive dissipation of turbulent energy from the small scales in the large wave number region. Consequently a well defined shape cannot be established at the end of the diffusion process. On the other hand employing the Crank-Nicolson scheme a stable $-5/3$ region is established as well as a clearly distinguished peak in the spectrum around $\kappa = 1000 \text{ m}^{-1}$ corresponding to the integral length scale, cf. also figure 6.1, can be observed, thus the

shape of the obtained spectrum leads to a good approximation of the desired form.

Although the principal approach and the integration into the CFD solver is quite straightforward, the method required unexpectedly huge CPU times. This can partly be accounted to the usage of extremely small time steps which have nevertheless shown to be necessary for stability reasons. These stability problems have especially been encountered for wall bounded domains [106, 107].

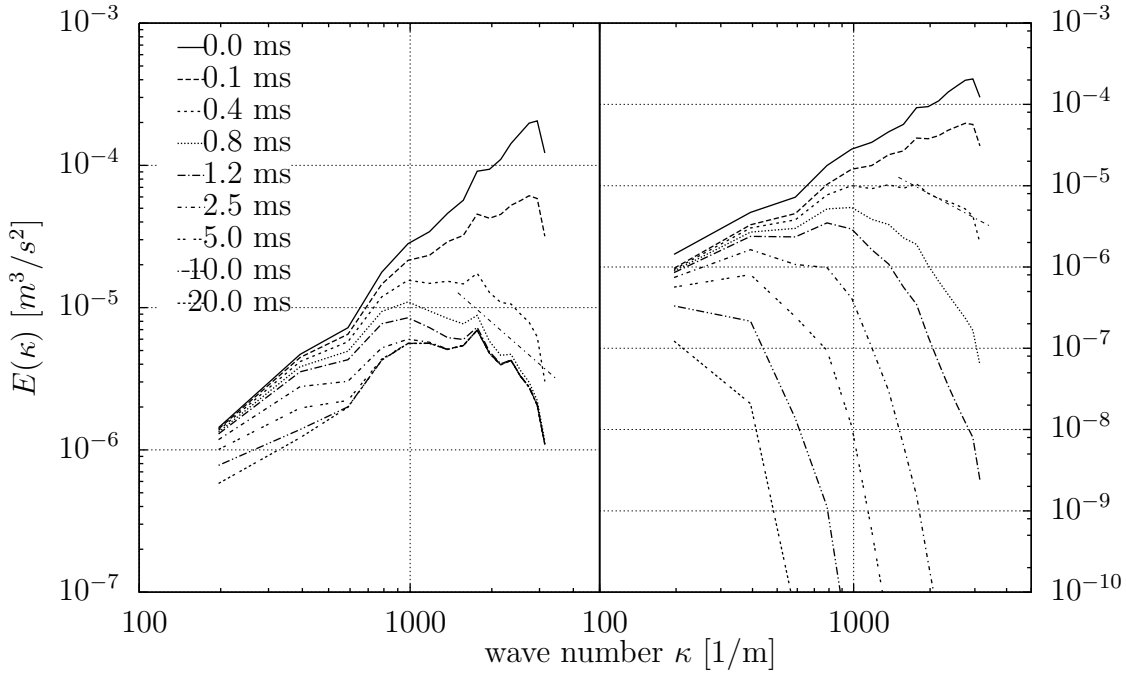


Figure 6.2: Time history of the spectrum of the diffusion process using different schemes for time integration; left: Crank-Nicolson; right: implicit Euler.

Truncated Fourier series. Based on the modified von Kàrmàn-Pao spectrum, equation (3.108), the initialisation of the turbulent velocity field has been performed based on the synthesized turbulence approach discussed in section 3.6.3. The parameters have been set in accordance to the characteristic quantities and fluid properties given in table 6.1.

The obtained spectra on the finest grid (mesh 3) of ten successive initialisations are shown in figure 6.3 with the prescribed analytical spectrum given for reference. The qualitative and quantitative agreement of the synthesised turbulent field with the reference is very good. In analogy to the inverse Fourier approach a pronounced mesh cut-off can be seen. The individual realisations show minor random fluctuations in the large wave number region which indicate the successful random initialisation of the flow field, i.e. the approach allows for the generation of multiple realisations of the turbulent velocity fluctuations based in the same basic spectrum. Similar to Fourier transform

approach the energy of the large scale structures in the small wave number region is slightly overestimated which demonstrated the connection between the two approaches, i.e. both algorithms are founded on same physical arguments.

The CPU requirements for the initialisation are given in table 6.3. Compared to the inverse Fourier transformation method the time is approximately one order of magnitude larger for all employed mesh resolutions. The increase due to the mesh refinement scales similar as for the Fourier case which is again an indication of the similarity between the two approaches.

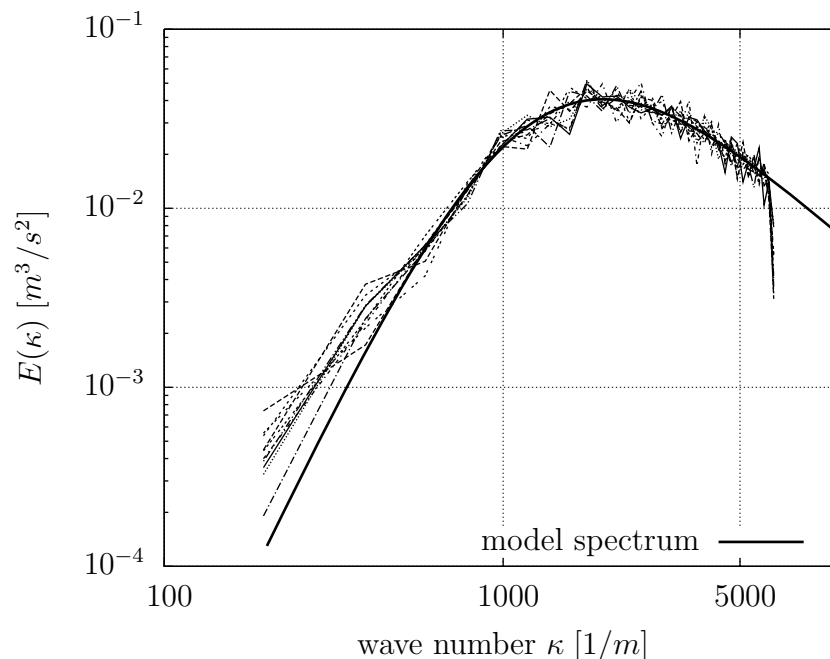


Figure 6.3: Synthesised turbulent spectra created of 10 successive initialisation; dashed line indicates analytical form of the model spectrum.

Appraisal. The inverse Fourier transform is the *de facto* standard approach for the initialisation of turbulent velocity field, cf. [113]. However the application of the method is restricted to simple geometries and meshes. Moreover, for efficiency considerations the transformation algorithm is based on Fast Fourier Transform algorithm (FFT), which imposes restrictions for the number of nodes in each spatial direction (2^n). Nonetheless the method has proved its usability for fundamental studies, for instance the decay of isotropic turbulence [113]. While the numerical cost in term of CPU time is comparatively low and the algorithm is fast, the complexity of the implementation is quite high.

The implementation and application of the diffusion approach is rather simple and

straightforward³. The extreme sensitivity with regard to the employed time integration scheme, leading to significant uncertainties in resulting shape of spectra, render the application of the method problematic. The CPU requirements have been unexpectedly high; a time step size optimisation has not been performed but the experienced instability of the method, especially for problems in wall bounded domains, indicates that small time steps are necessary. In contrast to the other approaches the diffusion approach requires after-treatment and post-processing (i.e. scaling) of the obtained velocity field in order to obtain the correct turbulent statistics.

The initialisation of a turbulent velocity field via the synthesized turbulence approach, i.e. via a truncated Fourier series, combines the positive elements of both approaches. The approach allows an excellent reproduction of the prescribed spectrum without any restrictions concerning geometry, node number, or mesh type. As shown in 6.3, the CPU requirements are moderate. The low complexity of the algorithm allows for a straightforward implementation.

| | | mesh 1 | mesh 2 | mesh 3 |
|------------------------|-------|-------------|--------|--------|
| Fourier transform | field | 0.6 | 8.9 | 42.5 |
| | total | 9.1 | 195.7 | 1442.6 |
| diffusion | | $\sim 24^h$ | – | – |
| synthesized turbulence | field | 111.5 | 892.3 | 3034.0 |
| | total | 123.2 | 1116.9 | 4633.1 |

Table 6.3: CPU requirements in seconds for the initialisation on a P4/3.2GHz Linux PC.

6.1.2 Numerical studies

Numerical diffusivity. In the context of RANS simulations the usage of upwind based schemes with a significant amount of numerical dissipation is usually favoured [15]. However, in case of LES care has to be taken that the influence of the numerical scheme, and here especially the numerical diffusivity, does not cover and hide the effect of the sub-filter model.

In the following the influence of numerical scheme on the velocity field is studied. When the viscosity is set to zero, the kinetic energy of the flow/system should ideally be conserved as the viscous dissipation is deactivated. Due to the energy cascade, the turbulent kinetic energy is shifted from the large scales and accumulated on the small scale of the spectrum which eventually leads to numerical instabilities and an explosion on enstrophy $\Omega^2 = \boldsymbol{\omega} \cdot \boldsymbol{\omega}$ [62], unless energy is removed from the small scale by the numerical scheme.

CFD codes for practical engineering application purposes generally use low order schemes (order 1 to 2) for both the temporal and spatial discretisation. Thus they

³This might also be the case when full source code is not available as in the case of commercial codes.

are inherently characterised by a significant amount of numerical diffusivity as well as being considerably dissipative. For general purpose usage these properties are favourable for stability reasons and therefore usually required⁴.

The influence of the temporal discretisation scheme on the resolved kinetic energy $u_i u_i$ for inviscid and viscid flow configurations is shown in figure 6.4 for the AC-FLUX code for two different temporal integration schemes. Additionally shown are results obtained by the commercial CFD solver *AVL Fire V8* [112] and the compressible CFD research code *AVBP* of CERFACS and Institut Français de Pétrole (IFP) obtained within the framework of the LESSCO2 project. All simulation employed identical settings considering the spatial and temporal resolution, i.e. the same mesh, mesh 1 in table 6.2 with 32^3 cells, and a time step Δt of $1.4 \cdot 10^{-6}$ s.

The two engine simulation codes, AC-FLUX and Fire, both use central differences for the convective terms, while the results of the AVBP code were obtained either employing a Lax-Wendroff (LW) scheme or a Taylor-Galerkin third order low-dissipation scheme (TTGC). Both engine codes exhibit a similar behaviour with the AC-FLUX code being slightly favourably less dissipative. Due to the numerical background and field of application (LES, DNS) the compressible solver AVBP shows an extremely low level of numerical dissipation⁵; furthermore AVBP employs an explicit time discretisation scheme.

The history of the kinetic energy with the inclusion of the viscous dissipation, i.e. employing a finite viscosity, is additionally shown in figure 6.4. The difference between the two temporal integration schemes for the viscous case is small, with the Crank-Nicolson scheme showing a slightly better performance than the implicit Euler integration. Compared to the effects of the viscous dissipation the numerical dissipation is sufficiently small to be neglected.

Enforcement of continuity - single PISO. The algorithms for creating the initial homogeneous isotropic turbulent velocity field do not necessarily satisfy the continuity equation due to numerical inaccuracies and grid cut-off effects, or inherently due to the employed algorithm as in case of the diffusion process. In order to obtain a divergence free velocity field a single time step has been performed using the PISO algorithm, cf. 5.2.1. While the initial field is characterised by the desired prescribed spectrum, the question arises how the spectrum changes due to enforcement of continuity.

The characteristic turbulent time scales can be determined based on the parameters given in table 6.1, namely the Kolmogorov time scale $\tau_k = (\nu/\varepsilon)^{1/2}$ with $\tau_k = 3.46 \cdot 10^{-5}$ s, and for the large scale motion the corresponding integral time scale $\tau_t = \ell_t/u'$ becomes $\tau_t = 6.67 \cdot 10^{-4}$ s. In order to keep disturbances to the initialised spectrum on a minimal level, the simulation time step should be smaller than the characteristic time scales, i.e.

⁴In an industrial context, results with a well known tendency (= too diffusive) are better than none

⁵This observation is not surprising, as the AVBP code and employed numerical schemes have been extensively tuned to achieve a low level of numerical diffusivity and dissipation.

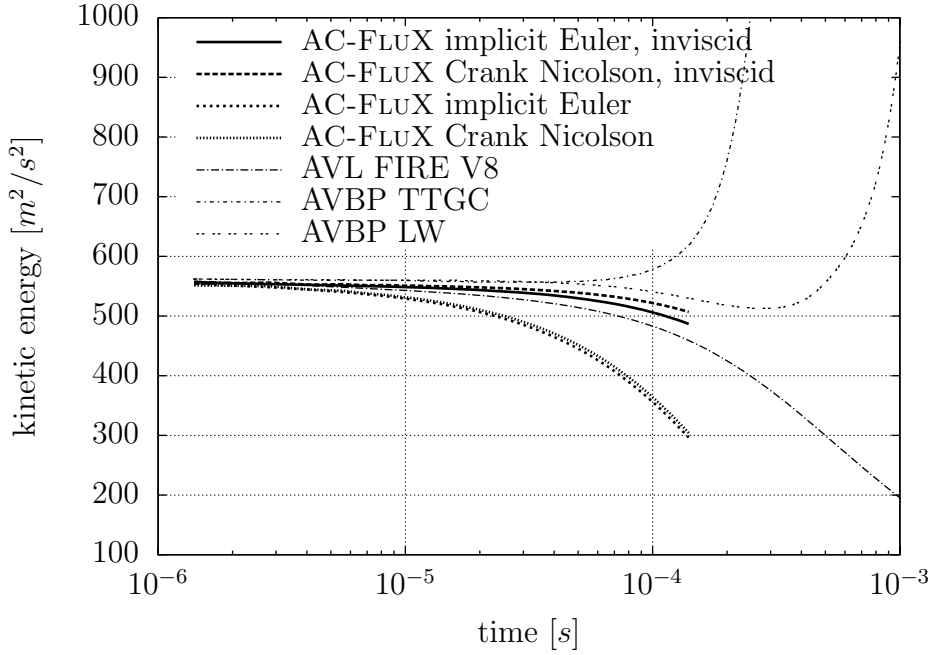


Figure 6.4: Time history of the resolved kinetic energy for several spatial and temporal schemes as well as CFD solver.

the Kolmogorov time scale τ_k .

In figures 6.5 and 6.6 the energy spectra obtained after advancing the solution a single time step Δt on the 32^3 mesh are shown for a viscid and an inviscid case respectively. The time integration scheme employed in both cases is the Crank-Nicolson scheme; to improve readability the curves have been smoothed and a semi-logarithmic plot has been used. Clearly, for time steps smaller than the Kolmogorov time scale τ_k the spectrum does not change significantly. Small changes occur near the mesh cut off which indicates that parts of the small scale structures are damped during the pressure correction process of the PISO algorithm. However, as these scales are of the order of the mesh size and cannot be correctly represented on the given mesh, their removal is desirable from a physical point-of-view.

An increase of the time step size beyond the Kolmogorov time scale to values of the order of the integral time scale τ_t reveals different behaviour. In that case the spectrum differs from its initial value and a significant amount of energy is removed from the large scales. In the inviscid case an accumulation of energy at the smallest scale can be observed cause by the lack of viscous dissipation. These effects are not visible when the chosen time step is sufficiently small. Employing the implicit time integration approach similar effects are visible, although the difference between the viscid and inviscid cases are much smaller due to the increase in numerical dissipation inherent to the numerical scheme as discussed above.

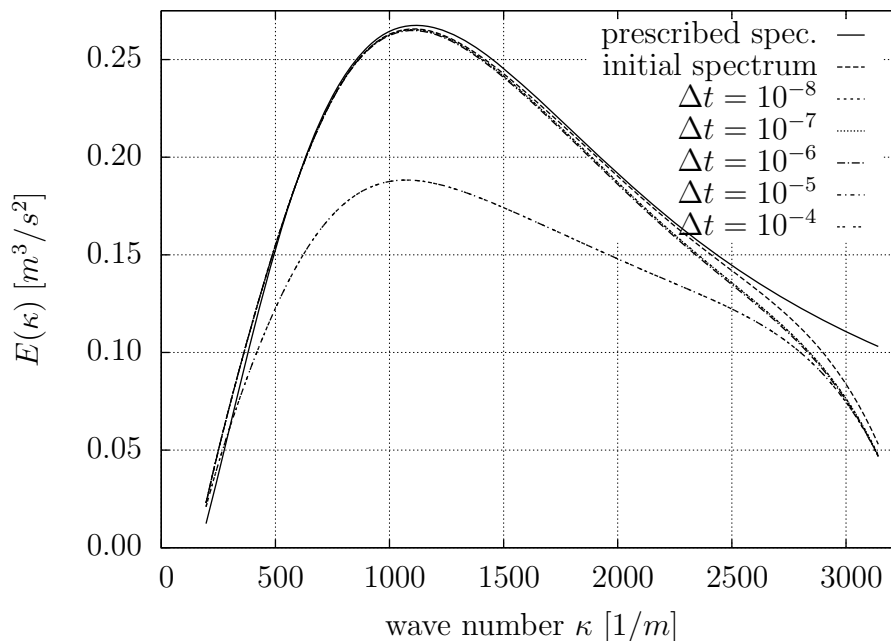


Figure 6.5: Influence of time step on spectrum after performing a single PISO step; for time steps smaller the Kolomogrov time scale τ_k the spectra collapse.

Remapping - Inter- and extrapolation. Due to moving geometries the computational mesh undergoes deformation by stretching, compression and shear which can lead to a significant number of deformed cells. For engine simulations, the valve motion or the piston movement during the compression and expansion phase are representative situations. Once the mesh quality falls below a certain level, the flow field has to be mapped (interpolated) onto another grid with a possible change in mesh topology. For RANS based simulations the largest structures are of the size of the integral length scale ℓ_t which is usually sufficiently resolved on the employed meshes. Furthermore all quantities are *per se* resolution independent, thus a change of the mesh and correspondingly the grid spacing does not lead to any issues apart from numerical questions regarding mass and energy conservation.

Due to the tight coupling of the grid spacing with the filter width in LES on the other hand, a change of the mesh resolution influences the resolved and resolvable turbulent scales. An interpolation from a coarse to a fine mesh, which is typical for the remapping after TDC⁶ during the expansion phase of an engine cycle, the problem of additional resolution in wave number space arises; scales which could not be resolved on the coarse mesh due to the grid cut-off can now be represented. The other way round, if the mesh is coarsened part of the turbulent spectrum cannot be resolved anymore and the energy

⁶Top Dead Centre.

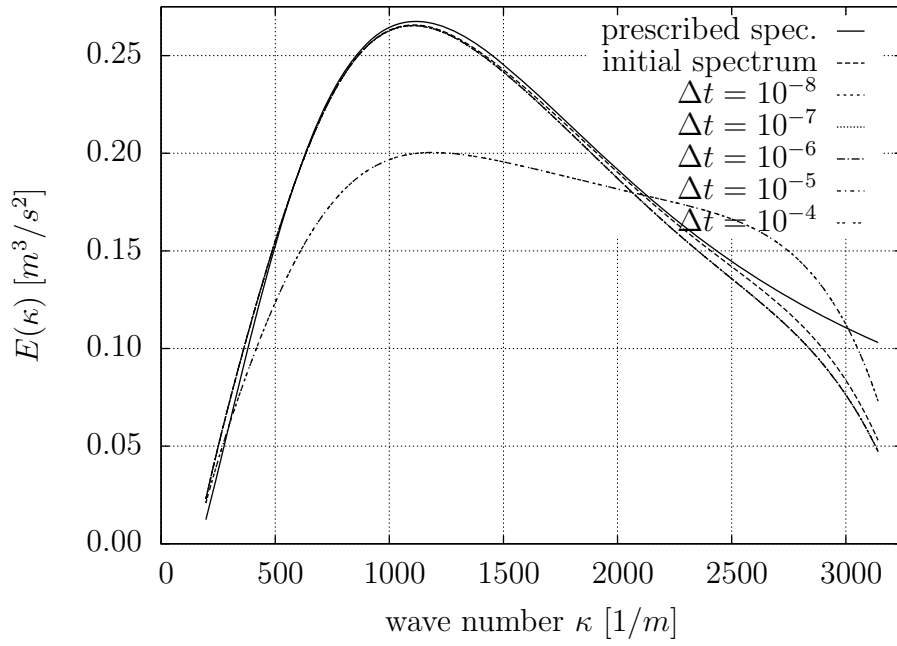


Figure 6.6: Influence of time step on spectrum after performing a single PISO step (inviscid)

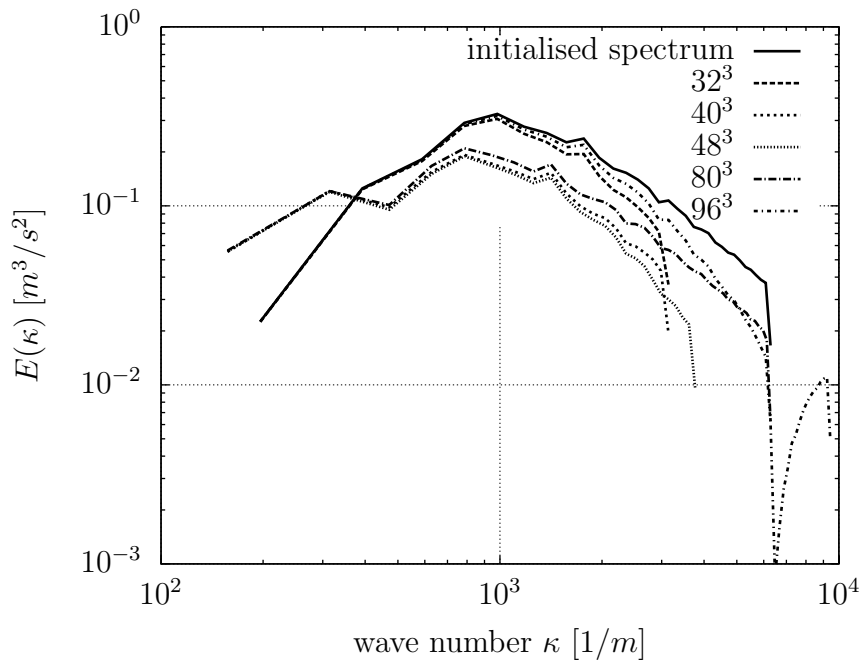


Figure 6.7: Effects of the conservative remapping algorithm onto the turbulent spectrum for fine (64^3) to coarse mesh mapping.

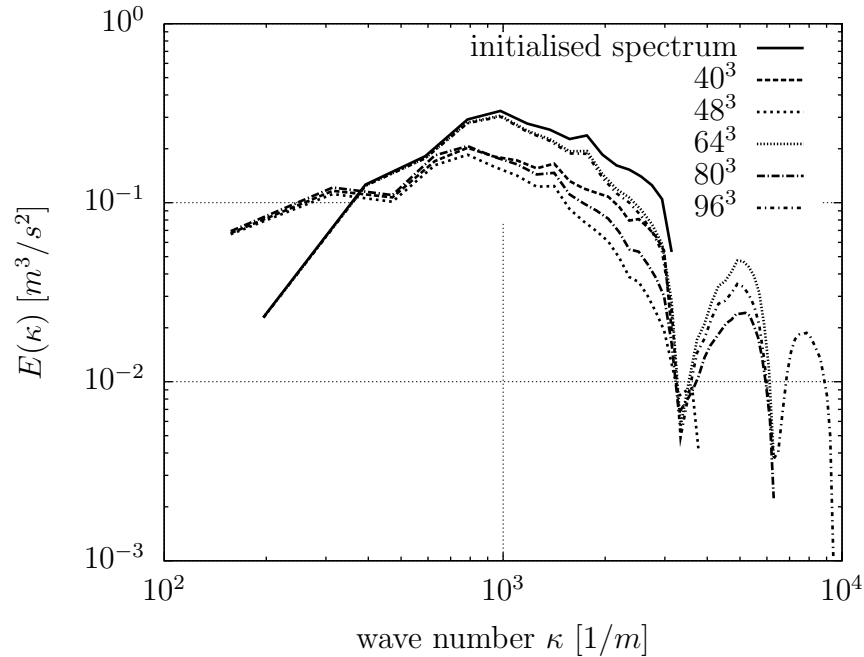


Figure 6.8: Effects of the conservative remapping algorithm onto the turbulent spectrum for coarse (32^3) to fine mesh mapping.

of the unresolved structures must be moved towards the resolved scales.

In order to investigate the impact of the remapping process of the turbulent velocity field and the turbulent spectrum respectively, again the model spectrum, equation (6.1), is initialised on two cubical meshes with 32^3 and 64^3 cells, and mapped onto meshes with resolutions of 32^3 , 40^3 , 48^3 , 64^3 , 80^3 , and 96^3 cells.

The effects for both grid coarsening and grid refinement onto the energy spectrum are depicted in figures 6.7 and 6.8. For the case of grid coarsening a slight shift of energy towards the small wave numbers, i.e. larger scales, on expense of the larger wave numbers can be observed while the general shape of the spectrum remains sufficiently unchanged.

The situation is different for the case of grid refinement. Here the scales beyond the grid cut-off of the coarse mesh are *suddenly* resolved, although not physically correctly initialised. The impact on the turbulent spectrum can be observed in figure 6.8. Similar to the fine-coarse grid mapping a slight shift of energy to the large scales and smaller wave numbers occurs. However due to lack of information about the structure and energy content of the small scales on the coarse grid, there is a *hole* in the energy spectrum. This gap is filled by energy taken from large scales and added to small, leading to the creation of *bumps* beyond the grid cut-off of the original mesh. Local minima of these artificial bumps are positioned at integer multiple of mesh cut-off, i.e. $n \kappa_c$, with maxima in between at approximately $\frac{n+1}{2} \kappa_c$; this aliasing effect is well known from spectral codes.

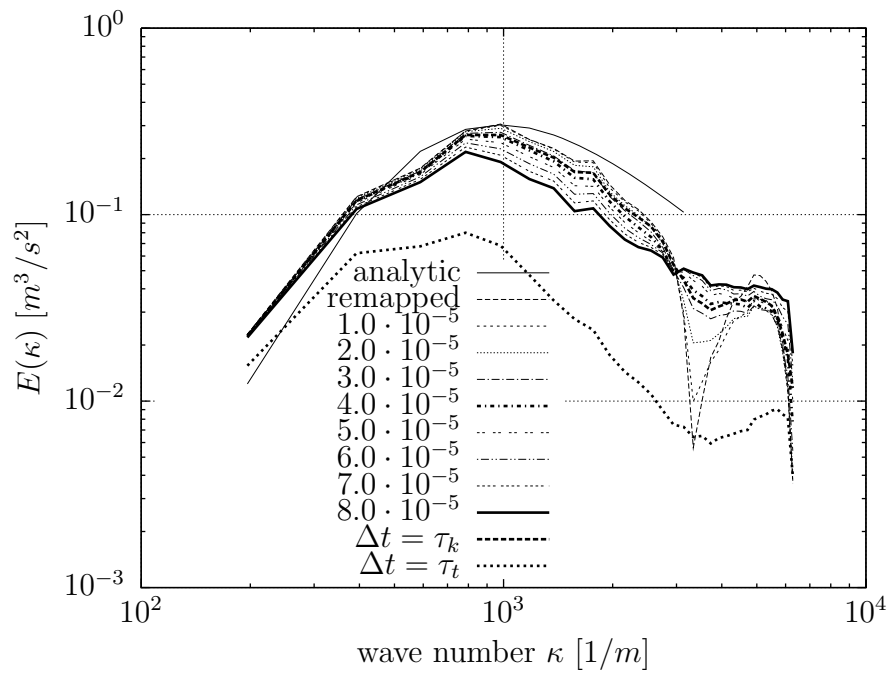


Figure 6.9: Time history of the turbulent spectrum after a coarse to fine mesh remapping $32^3 \rightarrow 64^3$ for a simulation of the order of magnitude of the Kolmogorov time scale τ_k .

After a time of approximately the Kolmogorov time scale τ_k the bumps and gaps are filled and a smooth spectrum is obtained, see figure 6.9; note that this time step size is unrealistic for real application where much larger time steps are used; therefore it can be assumed that within a single time step of a numerical simulation the remapped spectra is sufficiently smoothed.

6.2 Square piston engine

The flow in spark-ignition combustion engines is characterised by a tumbling motion, i.e. a large scale vortex whose axis is perpendicular to the cylinder axis. The tumbling motion is generated during the intake phase. During the compression a complex vortex breakdown occurs resulting in the generation of a significant turbulence level. The significance of this type of flow and the tumble motion in the context of IC-engines is increasing, especially considering direct injection spark ignition engines (DISI). An additional major issue for DISI engines is the problem of cycle-to-cycle variations of cyclic variability, which is thought to be related to the turbulent break-down to the tumble motion.

A simplified, quasi bi-dimensional model flow of the tumble compression has been experimentally studied by *Marc et al* [71]. Although strongly simplified, the geometry employed is representative of automotive cases in terms of tumble behaviour, volumetric ratio and tumbling number [73]. Additionally the major practical obstacles of real engine geometries are nicely removed, namely valve motion and geometrical complexity, while still capturing the main characteristics of real engine simulation problems and physics.

The experimental setup consists of a square compression chamber with large optical access. A square piston is animated with a sinusoidal motion. The intake system consists of a plenum chamber at ambient pressure, is a flat channel which is connected to the lower side of the compression chamber, and a guillotine device for closing the intake channel in phase with the piston motion. Thus it is possible to realise four stroke like cycle phases with intake, compression, expansion and exhaust. During the intake phase, the intake jet flow is deflected by the moving piston and generates the tumbling vortex.

The compression engine has a square $100 \times 100 \text{ mm}^2$ piston and is equipped with a flat head. The distance between the piston and the cylinder head at the end of the intake stroke is 100 mm. The piston is driven at 206 rpm, which leads to a maximum piston velocity of 1 m/s . PIV and LDV⁷ measurements of the velocity fields in the symmetry plane of the device have been performed.

6.2.1 Flow characterisation

The creation, establishment, and collapse of the tumble motion during the intake and compression phase in the symmetry plane of the compression chamber shown in fig-

⁷Particle Image Velocimetry, Laser Doppler Velocimetry

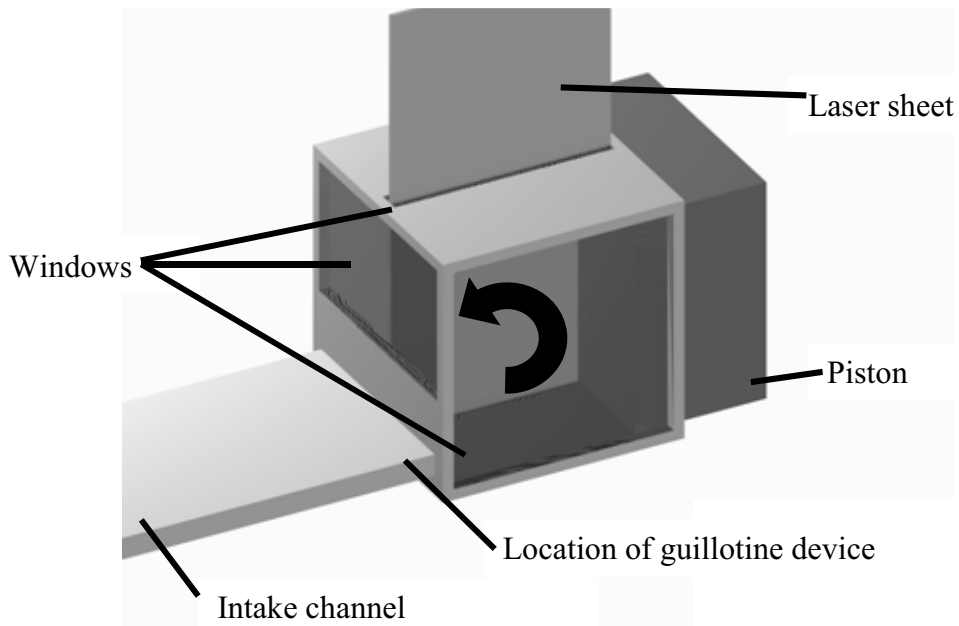


Figure 6.10: Sketch of the compression chamber [73].

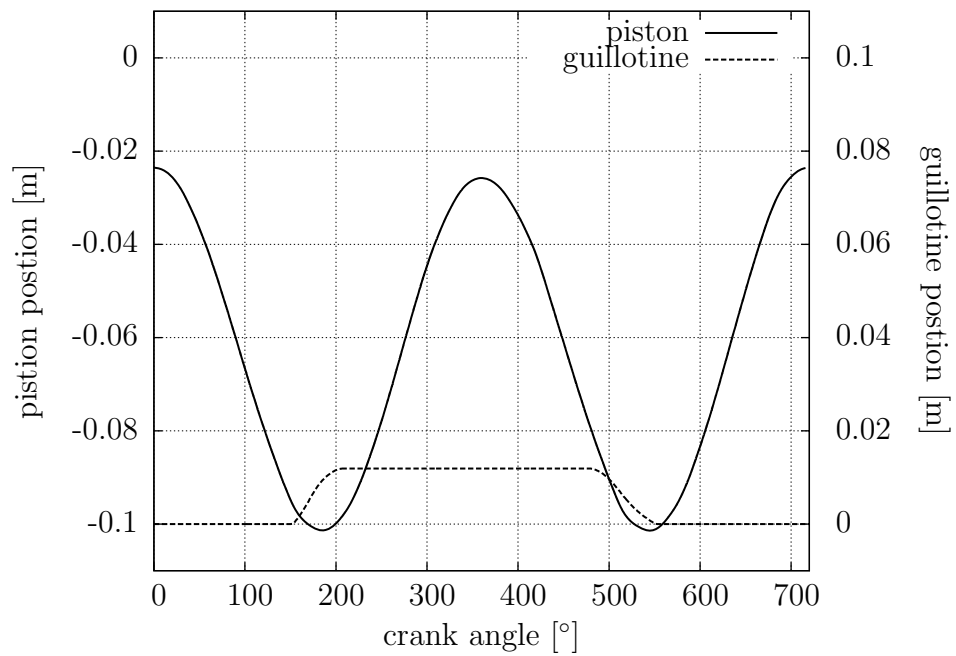


Figure 6.11: Piston and guillotine motion.

ure 6.12. During the intake stroke the tumble is created and stabilised by the incoming air jet. During most of the compression phase the large scale vortex motion is rather stable, but finally breaks down before TDC.

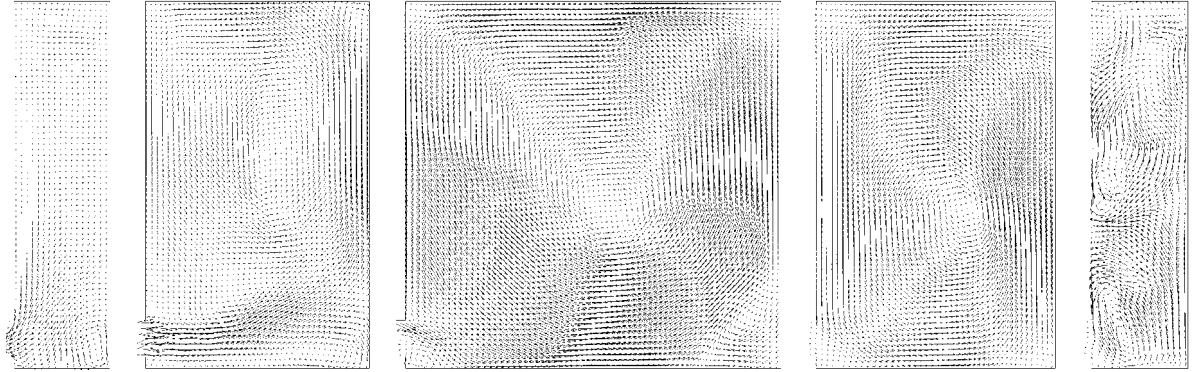


Figure 6.12: Instantaneous velocity field of the VLES in the symmetry plane of the compression chamber during intake and compression stroke at 0° , 90° , 180° , 270° , and 360° CA after TDC.

Figure 6.13 shows the instantaneous and ensemble-averaged velocity field during the intake stroke at 90° CA aTDC, i.e. during the creation of the tumbling motion. Significant cycle-to-cycle variations concerning the position of the vortex in horizontal and vertical direction are visible. Likewise the structure of the recirculation bubble at the end of the intake jet varies from cycle to cycle, and the instantaneous flow differs considerably from the averaged pattern. The flow is therefore characterised as being highly transient and strongly influenced by turbulence.

6.2.2 Results

The cycle-to-cycle variations of the flow in the simulation and the experiment are analysed in the median plane, i.e. in the principal symmetry plane of the geometry. Additionally the 1D profiles of the velocity and integral turbulent kinetic energy are considered in the centre of the median plane, analogue to the analysis performed in [79, 113]. The mesh employed in the current consists of approximately 210 000 cells.

Instantaneous profiles. Profiles of the instantaneous spanwise and axial velocity as well as the (integral) turbulent kinetic energy for the RANS and the VLES calculation during the intake stroke at 90° CA for multiple cycles are presented in figure 6.14 and 6.15 respectively.

An interesting phenomenon can be observed in figure 6.14 for the RANS simulation, where 2–3 cycles are required until a quasi steady-state is reached. Once that stable state is reached, the profiles of the following cycles collapse. A significant deviation

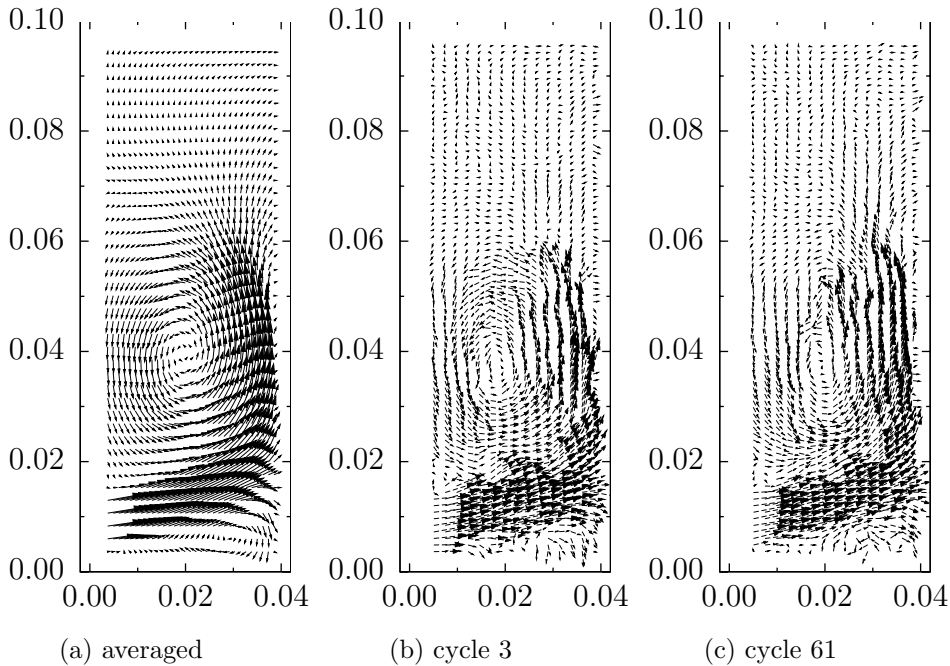


Figure 6.13: Experimental instantaneous (centre, right) and ensemble-averaged (left) velocity field during the intake stroke at 90° CA aTDC.

from that stable state is visible only for initial cycle, afterwards only minor changes are detectable. The initial variations are most prominent for the axial velocity and the turbulent kinetic energy, while the profiles of the spanwise velocity change only moderately. The direct implication of this observation concerns the simulation of intake flows for IC engines, which are performed in order to describe the fuel mixing process in GDI engines prior to ignition and combustion. A correct description of the flow structures requires the simulation of multiple cycles which includes the complete intake flow, compression, combustion, expansion and exhaust phase of the cycle; additionally the complete engine geometry including (part of) the intake and exhaust ducts must be modelled to accomplish this task with a reasonable level physical mapping.

Figure 6.15 presents the analogue analysis to figure 6.14 for the VLES case, but for 6 consecutive cycles instead of 4. Significant cycle to cycle variations are visible. The variability is most clearly visible for the axial velocity and turbulent kinetic energy, less distinct for the spanwise velocity component. This is in principal agreement with the observation in the RANS case, where the initial solution of these quantities differed most from the final stable state. A stable or quasi-steady state is not reached, but each individual cycle differs significantly from the previous and a convergence cannot be observed. The predicted flow is however not chaotic but these fluctuations happen around a stable mean profile, most prominent in case of the spanwise velocity, see figure 6.15b.

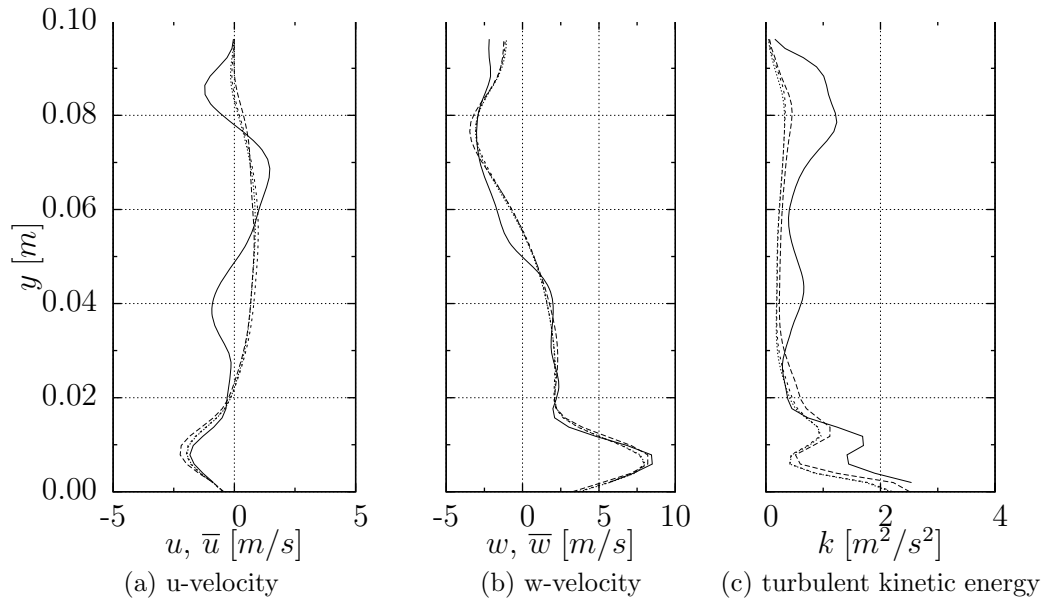


Figure 6.14: Instantaneous spanwise and axial velocity, and turbulent kinetic energy on the centre line of the symmetry plane at $90^\circ CA$ for the first four cycles of the RANS simulation.

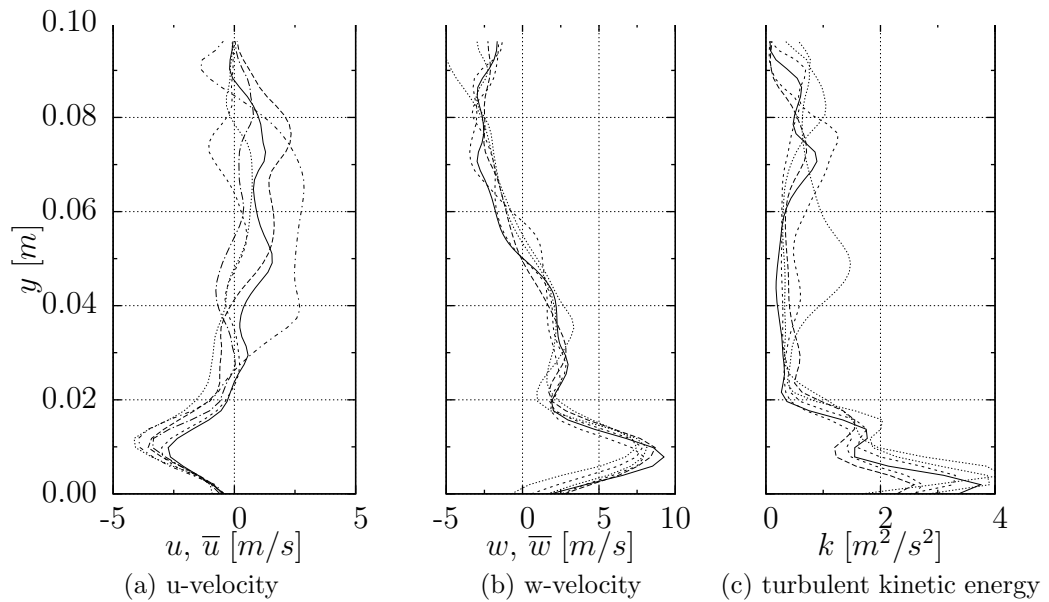


Figure 6.15: Instantaneous spanwise and axial velocity, and turbulent kinetic energy on the centre line of the symmetry plane at $90^\circ CA$ for the first 6 cycles of the VLES simulation.

Ensemble averaged velocities. In figures 6.16 and 6.17, the ensemble averaged spanwise and axial velocities at three different crank angle positions during intake and compression stroke are shown. The neglect of blow-by effects leads to a shift of the vortex centre. Correspondingly the simulation results for RANS as well as VLES are expected to deviate from the experimental reference values. Additionally values directly at the boundaries $y = 0$ and $0.1m$ are influenced and disturbed by post-processing artifacts and not fully reliable. The following discussion therefore focuses on a qualitative comparison of the simulation and the experiments.

At 90° CA aTDC, i.e. during the intake stroke, the profiles of the RANS and the VLES calculations are similar. The agreement with the experiment in the lower part of the compression chamber, say $y < 0.02m$, i.e. in the region of the jet entering the chamber from the intake channel, is fairly well in case of the axial velocity, while the spanwise velocity is over-predicted for the VLES but sufficient for the RANS simulation. In the middle and upper part of the compression chamber a poor agreement has to be noted during the early intake phase. During the intake phase the flow is dominated by the intake jet. However, a coarse mesh has been employed in the intake channel, thus the inflow conditions are dominated by the RANS model. The inflow velocity profile is therefore smooth and any turbulent fluctuation must be generated in the shear layer.

During the compression phase at -90° CA bTDC both models show a different behaviour. Due to the dissipativeness of the $k-\varepsilon$ model the spanwise velocity has almost vanished in the RANS calculation, and correspondingly already during the compression the model predicts a very early break down of the the tumble motion. The VLES approach on the other hand shows a better performance by qualitative reproducing the experimental shape and still featuring a significant velocity level; the deviations from the experimental reference can be attributed the discrepancies in the intake phase. The difference between RANS and VLES calculation concerning axial velocity are not as pronounced with VLES results showing a slightly better agreement. The interpretation the results are difficult due to post-processing effects which are visible at the upper and lower wall, where the velocity has to approach a value of zero (no-slip walls); the cause for the magnitude of the error is not clear.

At TDC the RANS simulation predicts almost zero values for both axial and spanwise velocities, while VLES and experiment both still show that the large scale vortex structures partially still remain. Again the VLES approach leads to a good qualitative agreement with the experiment.

The results can potentially be improved via two measures, which are expected to have an impact mainly onto the VLES results: (1) considering blow-by effects and (2) improving the intake channel mesh, which has been characterised by a very coarse resolution for the present simulations.

Influence of initial turbulent conditions The influence of the turbulent initial conditions onto the flow field and vortex structure are shown in figures 6.18– 6.19 for different

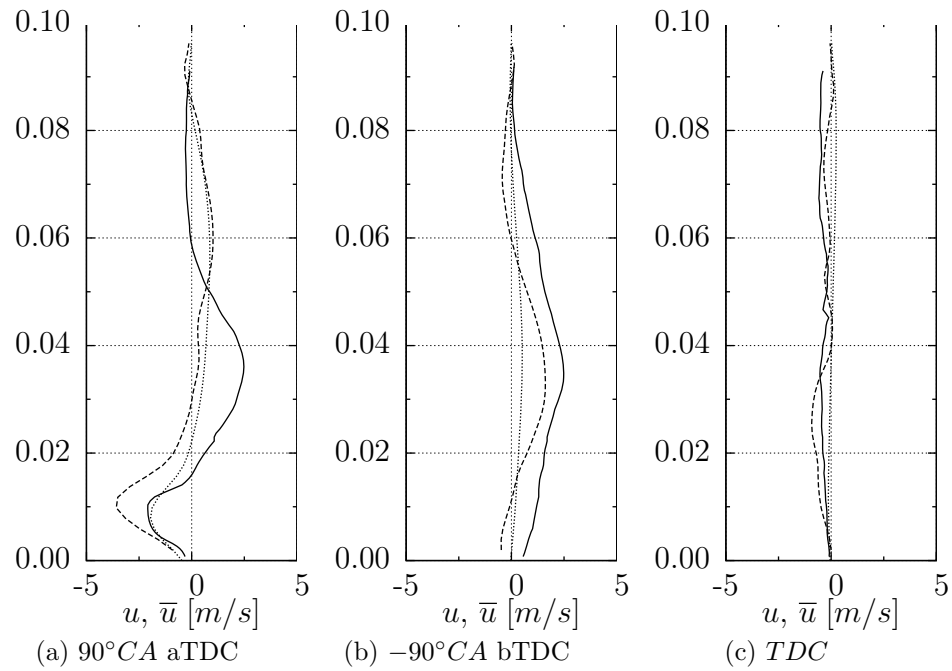


Figure 6.16: ensemble averaged spanwise velocity at $90^\circ CA$ aTDC, $-90^\circ CA$ bTDC, and TDC; experiment (solid), VLES (dashed), and RANS (dotted).

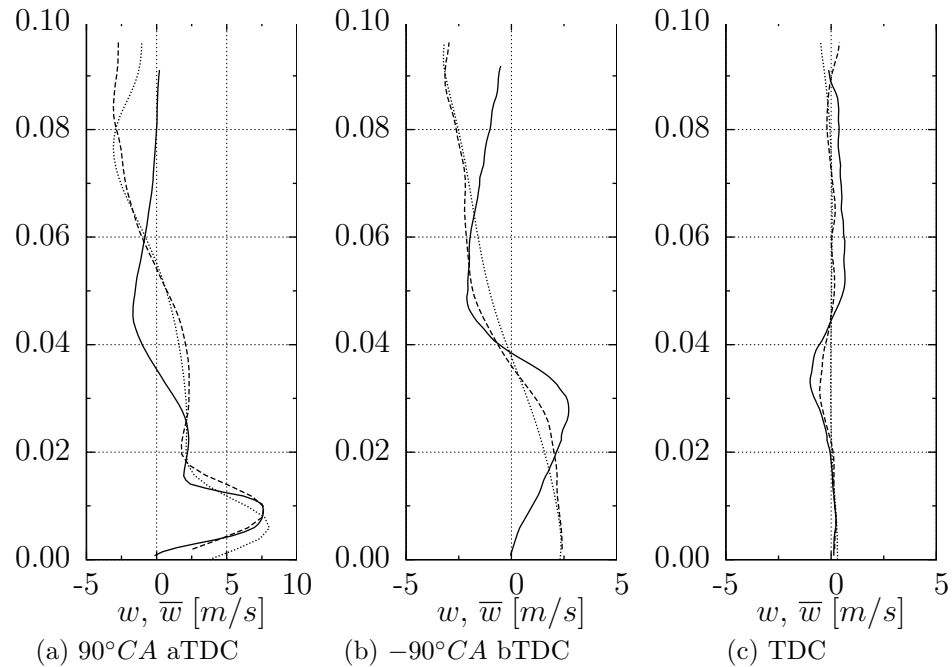


Figure 6.17: ensemble averaged axial velocity at $90^\circ CA$ aTDC, $-90^\circ CA$ bTDC, and TDC; experiment (solid), VLES (dashed), and RANS (dotted).

crank angles during intake, compression, and expansion phase. Two different initialisation strategies for the velocity fields have been employed: on the left hand side a resting field with zero velocity has been used, while on the right hand side turbulent fluctuations based on the synthesised turbulence approach, cf. section 3.6.3, have been imposed.

At the beginning of the intake cycle -270° CA bTDC hardly any difference between the flow pattern of the two initialisation strategies is visible. This behaviour is to be expected since (1) the mean profiles for both cases are identical (resting flow), and (2) the flow structure is dominated by intake jet flow. However, while the large scale motions are identical, the recirculation zones at the end of the intake jet (bottom right) show already slight differences in strength and size. At the end of the intake stroke the vortex centres of the large scale structures are mildly shifted, with the synthesised turbulence based solution being higher in the spanwise direction. The small offset becomes more and more pronounced during the compression phase, resulting in significant differences in the flow pattern at TDC. During the expansion phase, these changes in the overall flow pattern are still visible until the opening of the guillotine device in the outlet phase.

These results indicate the sensitivity of turbulent flows toward initial and inflow conditions, as discussed in section 3.1 for the case of the Lorenz model equations and in section 3.6 for the inflow boundary conditions for the simulation of a plane jet; in the present case however the complexity of the geometry is considerably higher. But also considering the additional complexity, small disturbances in initial conditions lead to significant different flow structure pattern. These findings support the assumption that turbulence and turbulence effects are one of the major sources for cyclic variability and cycle-to-cycle variations in gasoline engines. The impact of these initially small difference is immense, eventually leading to engine knock and misfires.

6.3 Multi-cycle engine simulations

The phenomenon of cyclic variability represent one of the major challenges of modern SI-engine design. A RANS-based modelling approach is ansatz-inherently not capable of covering these effects describing only a statistical average process. On the other hand, for practical flows in IC engines, the application of LES leads to unacceptable demands on mesh resolution and size, time step size and correspondingly memory requirements and CPU time. As demonstrated in the previous section the two-level modelling VLES approach allows for effectively characterising the flow in reciprocating model engine. In order to access the potential of the hybrid modelling approach, the VLES model is applied to the simulation of a four valve SI model engine with flat piston design depicted in figure 6.20; table 6.4 summarises the essential specifications of the engine set-up. The chosen operation point has been chosen arbitrarily as experimental reference data have not been available, but can be considered as being typical for part load conditions; however in the present investigation the focus lies on the feasibility of the description of cycle-to-cycle variations by means of the VLES approach, thus the actual conditions are

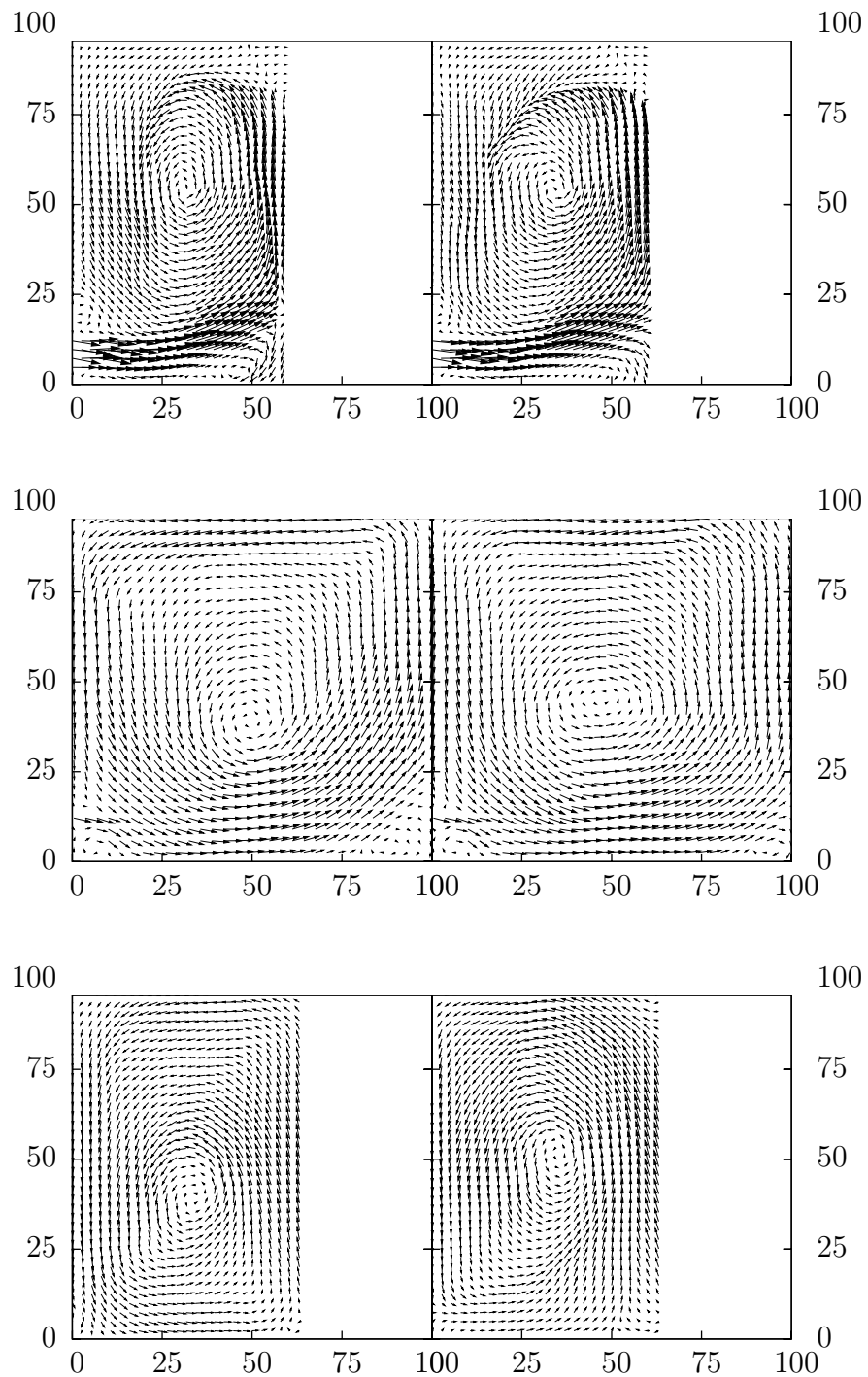


Figure 6.18: Qualitative comparison of the velocity field in the compression chamber at crank angles of -270° , -180° , and -90° CA bTDC (top to bottom); left: zero velocity, right: synthesised turbulence.

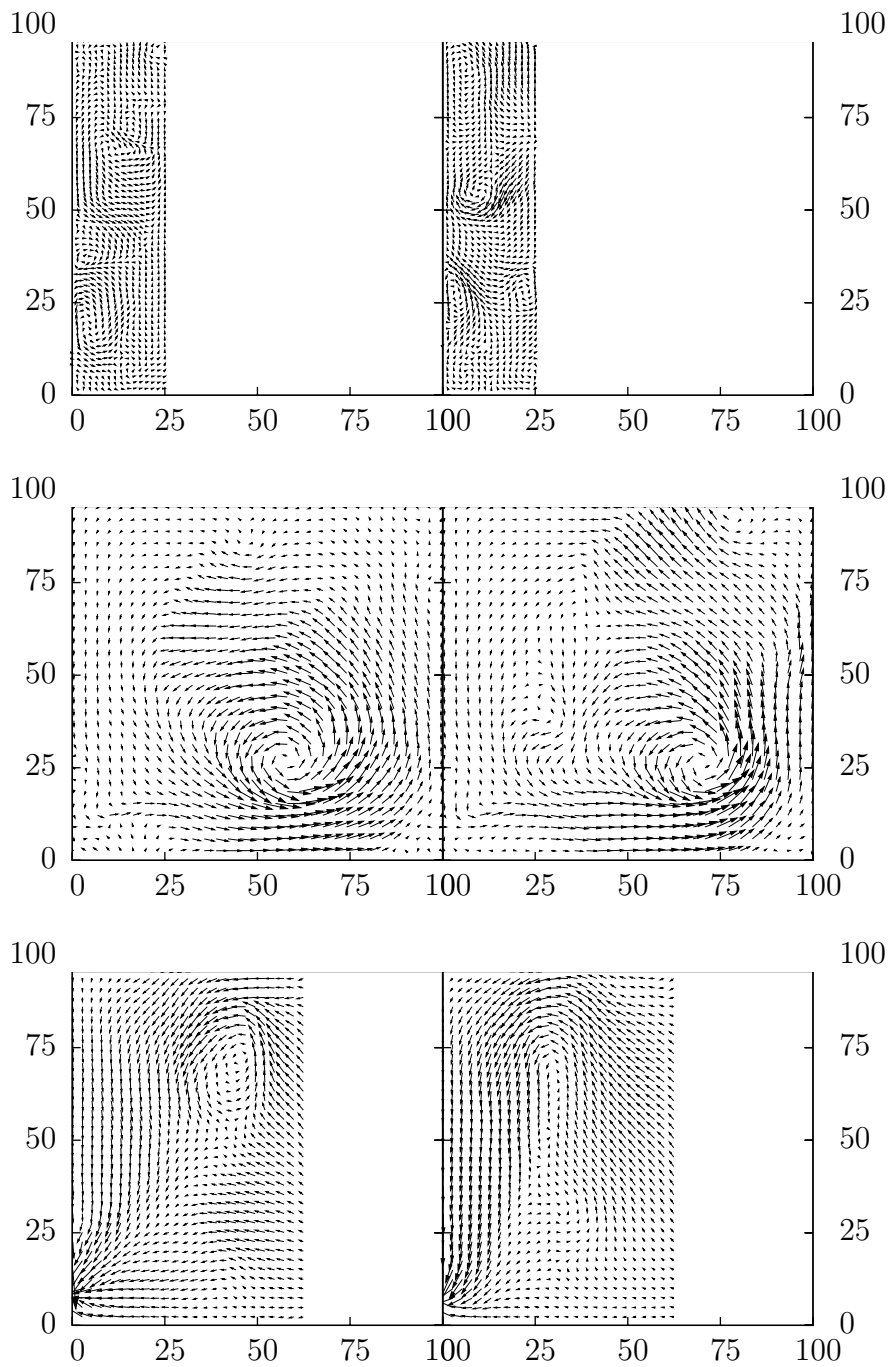


Figure 6.19: Qualitative comparison of the velocity field in the compression chamber at crank angles of $0^\circ, 180^\circ, 270^\circ$ CA aTDC (top to bottom); left: zero velocity, right: synthesised turbulence.

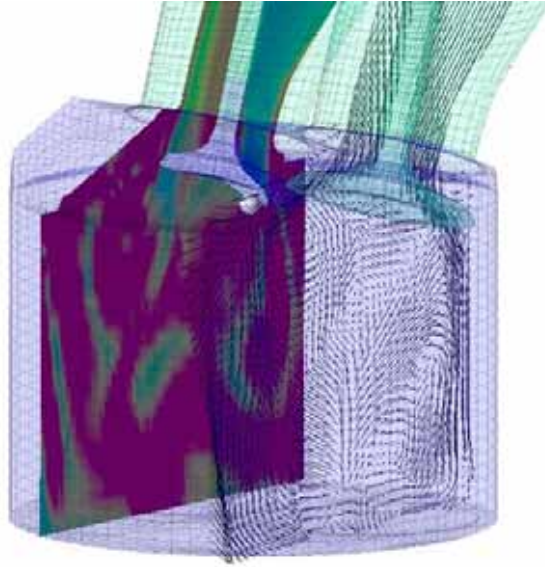


Figure 6.20: Model four valve SI engine during intake flow; on the cutplane velocity vectors and the amplitude of the vorticity; the bullet in the cylinder-head indicate the monitoring position used later on.

not of particular importance. For the simulation of multiple complete 720° cycles three different meshes of low-to-moderate size of approximately 150 000 cells are employed. The simulation intervals of the individual meshes are given in table 6.4. The resolution of the meshes is even for standard RANS simulation at the lower edge of current standards. However the mesh resolution allows already to cover a considerable part of the turbulent spectrum, and the effects of the VLES approach will become more prominent with increasing mesh size and improved resolution. As the focus of the study is placed on a fundamental level, a number of simplifications have been employed in order to reduce the numerical cost and the mesh generation complexity. During the course of the simulation only the relevant geometrical elements have been considered, i.e. for example during the compression stroke only the piston volume, neglecting the intake and exhausts ports. While the intake valves and the valve motion are completely modelled, a simplified model of the exhaust valves has been employed as the error introduced here can be considered as being of lower order. After each topology switch, the solution is interpolated onto the new mesh and the newly appearing volumes are re-initialised with constant values. Additionally constant pressure boundary conditions have been applied at the in- and outlet.

The ratio between the filter width $\bar{\Delta}$ and the integral length scale ℓ_t during the late intake phase and the compression stroke is depicted in figure 6.21. Additionally the position of $\bar{\Delta}/\ell_t$ is shown, i.e. the line separating the RANS and LES regimes; the peaks near the piston surface of the isoline can be attributed to postprocessing effects. Similar

| | |
|----------------------|--------------|
| stroke | 86 mm |
| bore | 92 mm |
| engine speed | 2000 rpm |
| intake valve closure | 580° |
| | 370° – 580° |
| simulation intervals | 580° – 890° |
| | 890° – 1090° |

Table 6.4: Engine characteristics.

to zonal hybrid models the near-wall regions are modelled employing the RANS mode while the core region of the piston the LES mode prevails, although this is not inevitably the case. In the region of high shear beyond the valve curtains, during the intake phase, i.e. at larger valve lifts which are not depicted here, the turbulent length scale becomes too small to be resolvable on the employed mesh. In these jet-like regions the model automatically uses the RANS mode of the model, accounting for the insufficient mesh resolution. The major part of the cylinder volume lies within the range $\bar{\Delta}/\ell_t < 1$, which denotes the LES mode of the model. Although a rather coarse mesh is used in the present study, the cell sizes are sufficiently small to resolve the turbulent spectrum beyond the integral length scale. While during the intake flow a significant part of the simulation volume employs the RANS mode, the compression phase is dominated by the LES sub-model. Extrapolating the results by considering the subsequent events of fuel injection, ignition and combustion, the modelling and description of these processes is decisively influenced by the improved representation of the turbulent flow field, thus allowing to investigate flow phenomena which are not describable on a pure RANS base.

These findings are supported by the transient analysis of the turbulent kinetic energy and the axial velocity in the spark plug region. The history of the turbulent kinetic energy and the axial velocity near the spark plug (the bullet in figure 6.20) are shown in figure 6.22 for ten full cycles employing the hybrid VLES model. The first three cycles of the simulation reveal significant variations of the flow pattern. After this initial transitional phase stochastic variations of the flow field around an average value can be detected in the following cycles indicating the cycle-to-cycle variability phenomenon. The largest variations in the profiles can be detected during the compression stroke around -100° to -50° before top dead centre, i.e. during the essential phase for the air-fuel mixing process.

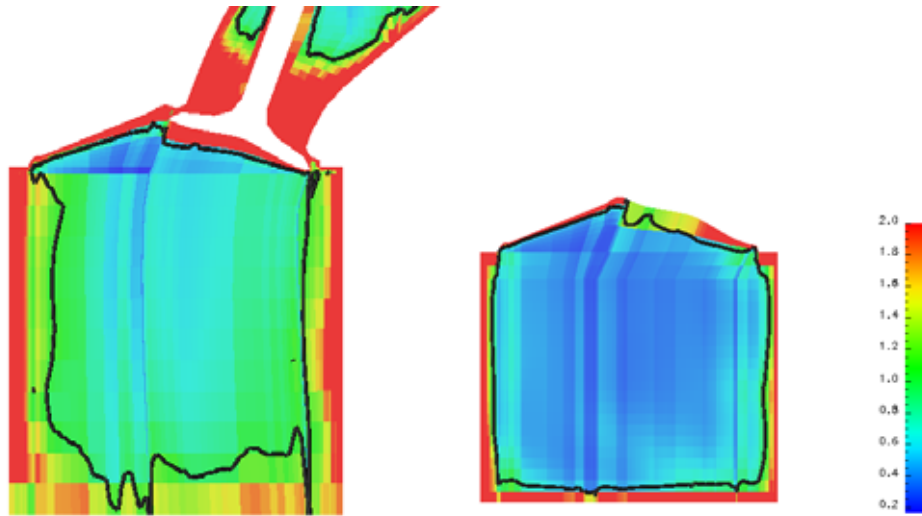


Figure 6.21: Length scale ratio during intake and compression stroke; thick line corresponds equal sizes of the filter width and the integral length scale, i.e. $\bar{\Delta}/\ell_t = 1$, with $\ell_t = C_\mu k^2/\varepsilon$.

6.4 Cylindrical disk

In the present section the two-level VLES/ G -equation model is evaluated on basis of experiments in a cylindrical vessel carried out by *Hamamoto et al.* [41, 42]. The setup has been extensively analyzed numerically in the context of RANS G -equation approach by Ewald [32]. A homogeneous stoichiometric propane-air mixture is subjected to an axisymmetric swirling flow, in which by variation of the ignition timing during the swirl decay the effect of different swirl intensities are studied. Similar to the previous section the focus of the present investigation lies on the feasibility of the two-level approach to describe the essential features of the combustion process, which are not realisable on basis of RANS modelling approach. The experimental setup is documented in various publications [41–45, 50] and [32]. Figure 6.23 gives a schematic representation of the apparatus employed during the experimental studies. The combustion chamber is a cylindrical vessel, with a diameter of $d = 125$ mm and a width of $h = 35$ mm. A swirling fuel-air mixture is produced by charging the mixture tangentially through a swirl valve. After removal of the valve the mixture is centrally ignited; different swirl intensities can be realised by shifting the ignition time after intake valve closure.

The initialisation of the flow field follows the setup developed and employed by [32], including parametrisation of the ignition model; table 6.5 summarizes the initial conditions for the flow field. An ignition time of 10 ms after swirl valve closure has been chosen for the following analysis.

The original computational mesh, consisting of approximately 60 000 computational cells, has been locally refined around the flame front in the course of the simulation

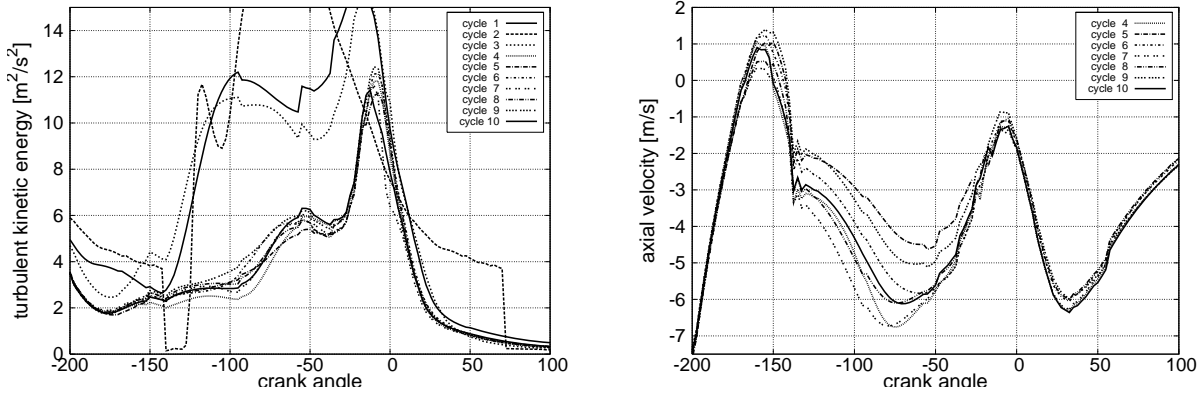


Figure 6.22: History of the turbulent kinetic energy (left) and the axial velocity (right) over multiple cycles indicating cycle-to-cycle variation of the in-cylinder flow structures.

| | |
|----------------------|--|
| p | 243 kPa |
| T | 335 K |
| ω | $\frac{5.05 \text{ m/s}}{r} \tanh \frac{r}{0.013 \text{ m}}, \quad r = \sqrt{x^2 + y^2}$ |
| $\tilde{\mathbf{u}}$ | $\omega(\mathbf{e}_z \times \mathbf{x}), \quad \mathbf{e}_z = (0, 0, 1)^T$ |
| k | $5.0 \text{ m}^2/\text{s}^2$ |
| ℓ_m | $\min(8 \cdot 10^{-3} \text{ m}, \kappa y_{\text{wall}}), \quad \kappa = 0.419$ |
| ε | $c_\mu^{3/4} \frac{k^{3/2}}{\ell_m}$ |
| ϕ | 1.0 |
| \tilde{G} | $\ll 0 \text{ m}$ |
| \tilde{G}''^2 | 0 m^2 |

Table 6.5: Initial condition for the mean quantities of the cylindrical test case [32].

via an adaptive mesh refinement algorithm. Similar to the model engine simulations, the base mesh resolution is rather coarse. This approach, although successfully applied in the RANS context, is not easily applicable within the framework of the two-scale modelling approach due to the employed coupling of the filter width with the local mesh spacing. Instead a slightly smoothed mesh consisting of approximately 120 000 cells is employed.

Pre-ignition, cold flow results. The initialisation of the flow field is based on the previously discussed settings from [32]. To account for turbulent effects in the VLES mode, additionally synthesised velocity fluctuations have been superimposed on the (smooth) RANS field according to the approach of section 3.6.3. After a decay time of 10 ms, i.e. at time of ignition, the resulting velocity fields on a vertical cut through the geometry are

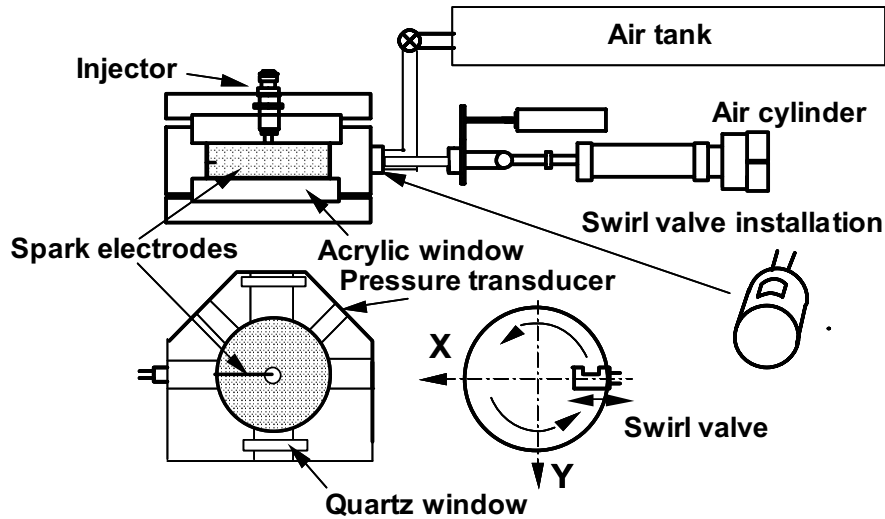


Figure 6.23: Schematic diagramme of the experimental apparatus [50].

depicted in 6.24 for the case of the two VLES runs with independent turbulent initialisations. Figure 6.25 shows the velocity field for two VLES simulations employing varying filter factors⁸ of $\beta = 3.0$ (top) and 10.0 (centre), and for the standard RANS approach (bottom). For all cases the identical numerical set-up has been employed. Although the RANS simulation also used the same initial turbulent velocity field as the VLES run with $\beta = 3.0$ ⁹, the model yields a smooth field without any significant fluctuations remaining from the turbulent initialisation. This implies that due to its dissipativeness the model damps all fluctuations. On the other hand, the fields obtained employing VLES approach exhibit a significant level of turbulence at time of ignition, and large scale structures remain despite the rather long decay time. Additionally, the turbulent initialisation approach yields locally distinct flow fields at time of ignition, while the mean structure remains equal. However, as can deduced from the depiction, only qualitatively large scale structures are resolved. This can be attributed to the coarse mesh whose resolution does not allow to resolve finer turbulent structures, as well as additionally an implicit filtering of the field caused by the low order numerical schemes and algorithms of the employed code.

The spatial distribution of the integral turbulent kinetic energy k for a VLES and a RANS based simulation at start of ignition on two cut planes, a vertical and a horizontal, is visualised in figure 6.26; in both pictures the same colour scale has been employ for colourizing the cutplanes. Although the flow field, and the turbulent production (and dissipation terms) are significantly different due to the underlying modelling approaches

⁸For the definition of the filter factor see (3.79).

⁹Actually this approach is physically not reasonable, even contradicting the modelling approach, but has been chosen for obtaining consistent initial conditions for all simulation runs.

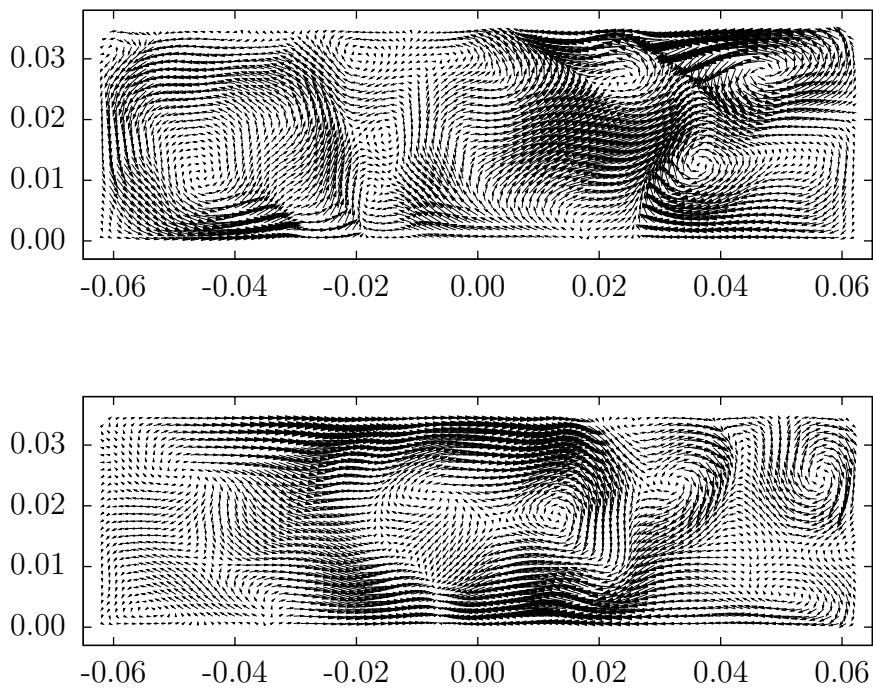


Figure 6.24: VLES velocity field on a vertical cut through the combustion chamber at time of ignition ($t = 10$ ms) of two distinct initialisations ($\beta = 3$) based on the synthesized turbulence approach.

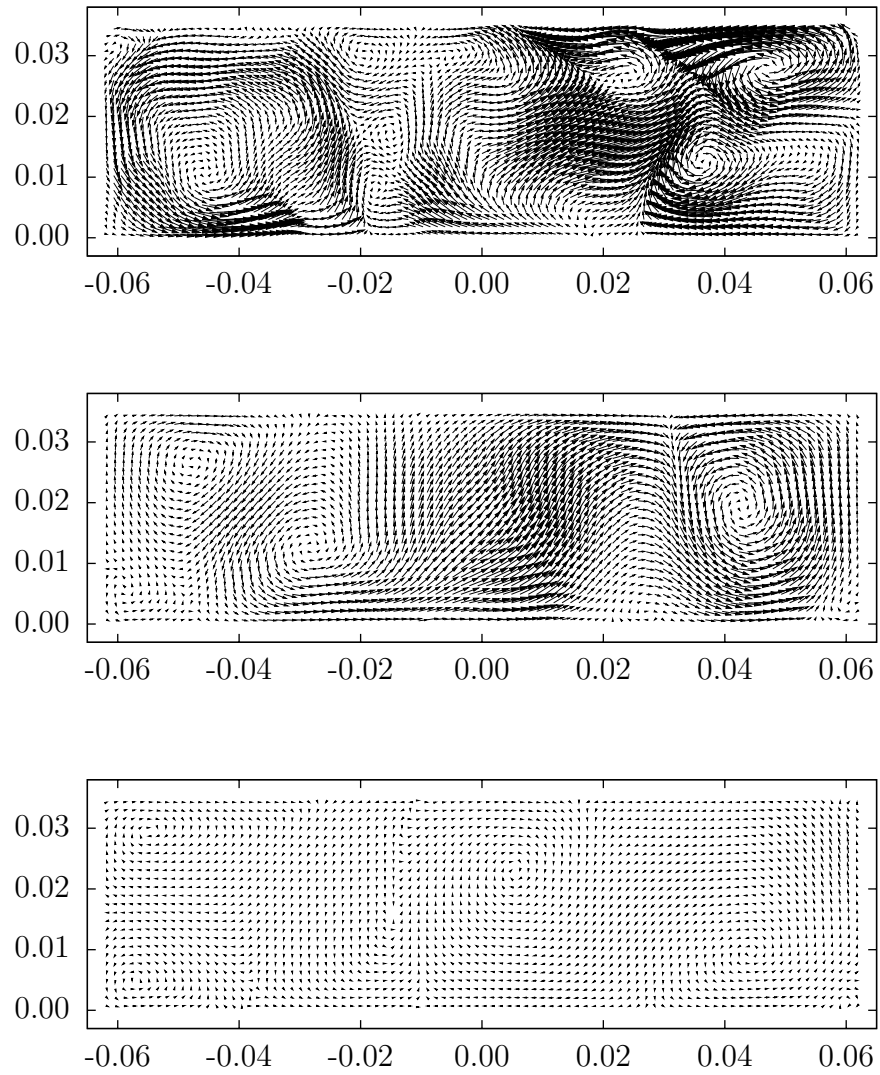


Figure 6.25: Velocity field on a vertical cut through the combustion chamber at time of ignition ($t = 10$ ms); top and centre: VLES ($\beta = 3.0$ and 10.0 , respectively), bottom: RANS (initialisation based on VLES setup with $\beta = 3.0$).

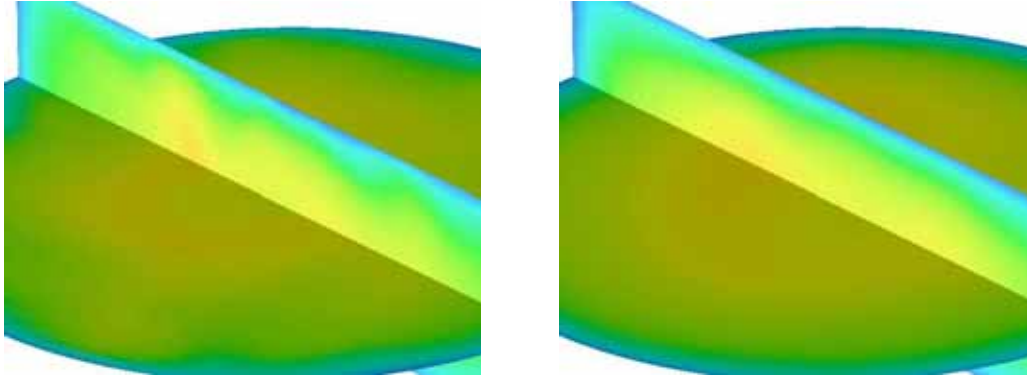


Figure 6.26: Integral turbulent kinetic energy k on two cuts through the combustion chamber at time of ignition ($t = 10$ ms); the same colour map is employed for both cases; left: VLES ($\beta = 3.0$), right: RANS (initialisation based on VLES setup with $\beta = 3.0$)

as shown in figure 6.25, the distribution and magnitude of the integral turbulent kinetic energy is consistent between the two cases and agrees well.

Combustion results. After the ignition, the initial flame growth and development occurs on the scales well below the resolution of the mesh. Here the G -equation based ignition model [32] has been used to describe the inception phase. As discussed in [32] curvature effects play an essential role in the development of the flame kernel, possibly yielding flame kernel quenching. This indicates that the ignition phase and the early stages of the flame expansion have a significant influence on the later flame propagation and flame development. While the original ignition model has been used in the present study, a novel and enhanced version is currently being developed [24].

Figure 6.27 depicts flame front at $t = 4$ ms after start of ignition for two successive turbulent initialisation. The flame deformation due to resolved large scale structures of the underlying turbulent flow field is clearly visible, i.e. different turbulent initialisations yield differing flame shapes. However the increase of flame surface area due to turbulent wrinkling effects is severely underestimated, thus the flame propagation resembles those of a RANS-base turbulent modelling approach. The main cause can be attribute to the low order numerics of the level set solver, which are essentially upwind based in the employed implementation. This leads to an underestimation of the flame wrinkling and thus the surface production. Correspondingly the flame surface is significantly underresolved which cannot be compensated by an increase of the turbulent burning velocity (as in the RANS case). As discussed in section 4.2.2 the product $\bar{s}_t \bar{A}_t$ is inertial scale invariant. However as the resolved flame surface \bar{A}_t is too small, the mass burning rate \dot{m}_B is significantly underpredicted.

The aforementioned observation is not only valid for the phase of the free flame propaga-

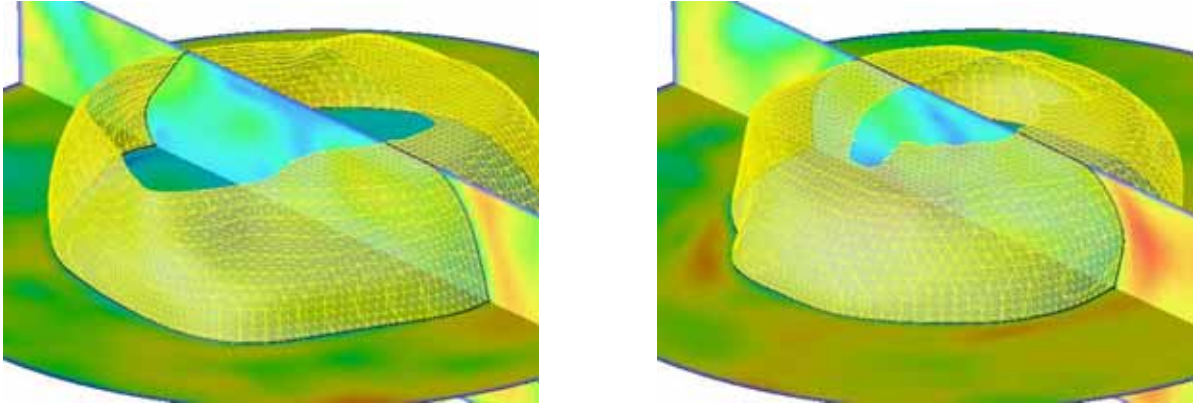


Figure 6.27: Deformed flames at $t = 4$ ms after start of ignition for two distinct turbulent initialisations as defined via the $G = G_0$ iso-surface; additionally shown are two orthogonal cutplanes through the centre of the geometry coloured by the local velocity magnitude.

tion. The ignition model has not been adopted to VLES modelling principles. The initial flame expansion and transition from ignition model to 3D flame propagation decisively influences the following combustion process and cannot be compensated or corrected in the later phase. Therefore a comparison to experimental references is presently omitted, and the focus is laid on the feasibility of the coupling approach.

Aggressive mesh refinement In order to validate the principle approach of coupling the two-level VLES model with the G -equation, an aggressive local mesh refinement is applied. Here the mesh around flame surface $G = G_0$ is locally adopted by splitting the original cells up to a refinement level of 3; the refinement level indicates the number of newly introduced cells. By this mesh adaptation the discretisation error and the corresponding related numerical diffusivity of the low order discretisation scheme can be reduced. The set-up of local refinement algorithm has been used in agreement with the RANS setup employed in [32], thus being able to unambiguously identify the effects of the two-level model onto the flame structure.

The mesh refinement is restricted locally to the region around the flame surface $G = G_0$. A special treatment for sub-filter kinetic energy has not been implemented but is required due to the coupling of the filter width and the mesh spacing: in case of mesh refinement a part of the sub-filter kinetic energy has to be transferred as (resolved) turbulent fluctuation into the flow field, and vice versa in the case of mesh coarsening. The former could be realised similar to the employed turbulent initialisation approach via *interface forcing*, i.e. by the addition of additional turbulent velocity fluctuations in region of increase mesh resolution, cf. for instance [26]. Consequently the results obtained via the (aggressive) mesh refinement approach cannot be expected to be physical, but should be interpreted as a demonstration of the dependency of the flame shape and

flame wrinkling on the mesh resolution and numerics.

The development of the flame after ignition is depicted in figure 6.28. Initially, due to the employed ignition model, a spherical flame is formed. In the following the turbulent flow fields leads to a wrinkling and folding of flame front. This wrinkling continues until the flame reaches the upper and lower walls. Afterwards the front slowly becomes smoother, however a significant level of convolution remains.

The observed behaviour differs significantly from those in the RANS context. Employing a pure RANS modelling approach leads a smooth, almost spherical flame propagation, which is slightly deformed due to geometrical constriction by the upper and lower wall. As a statistical average flame is considered, this behaviour is reasonable. The VLES approach however allows for incorporating transient and local turbulent effects, influencing the flame propagation.

In order to overcome the discussed numerical challenges, there is the necessity for improving level set solver from a numerical point of view. Here the refined Level Set Approach developed by M. Herrmann, cf. for instance [48], seems the most promising approach. In this approach the Level Set solver is completely decoupled from the Finite Volume code and solves the flame propagation on an independent (Cartesian) mesh employing both higher order numerical methods as well as a significantly higher mesh resolution; the results are then exchanged via inter- and extrapolation between the grids.

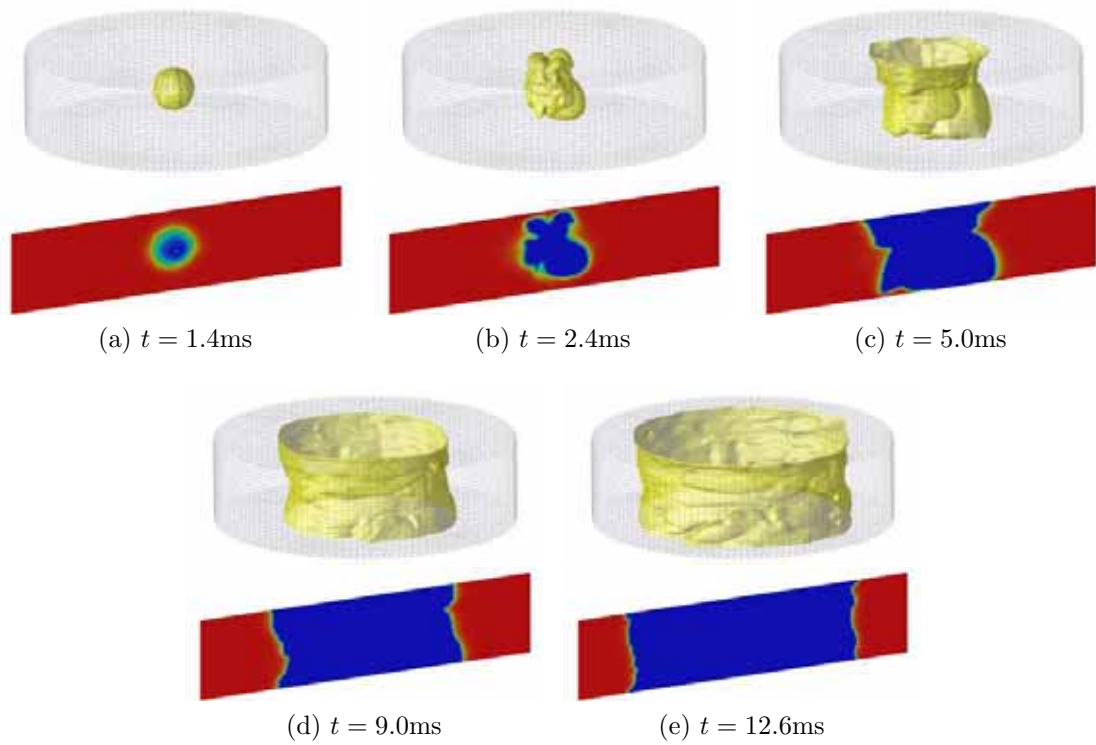


Figure 6.28: The flame front ($G = G_0$) and the probability I_{unb} at different times after ignition.

7 Summary and conclusion

Cyclic variability represents one of the key issues and challenges for the optimisation of combustion process in DISI-engines. In the present work a two-level VLES model, based on a hybrid RANS-LES modelling approach, has been developed. The model has demonstrated its capability to capture cycle-to-cycle variation which cannot be modelled by statistical RANS-based turbulence models. The feasibility of coupling the two-level model to the G -equation combustion has been analysed and successfully demonstrated.

In the context of RANS simulations the influence of the numerical dissipation of the applied algorithm is usually negligible due to the high level of the turbulent viscosity¹. In the industrial application, additionally low order numerical schemes for both spatial and temporal discretisation are commonly employed for stability reasons. Considering LES and VLES however, the only part of the turbulent spectrum is modelled and the turbulent structures are partially resolved. Thus the turbulent eddy viscosity is significantly smaller. In order to be able resolve smaller temporal and spatial structures, higher order schemes are required. Central schemes of at least second order have been demonstrated to be desirable as these introduce a minimum amount of numerical dissipation and dispersion [15,20,113]. It has been demonstrated that this proposition is not only valid in the context of spatial but also of temporal discretisation.

The evolution of a turbulent flow field is strongly influenced by the initial turbulent conditions. While standard techniques based on the application of FFTs for transforming a desired spectrum from spectral to physical space have been developed for academic studies, these classical approaches cannot be directly applied to complex engineering geometries. An alternative, novel approach base on truncated Fourier series has been demonstrated to be suitable for generating turbulent fluctuations on arbitrary geometries. This method has been shown to be numerically efficient, stable, and to yield the desired turbulent spectrum with a sufficiently high accuracy.

The simulation of complex moving geometries, as in IC engines, requires the interpolation of the solution onto a different meshes in the course of the simulation. It has been shown that this interpolation sufficiently conserves the original turbulent spectrum. In the case of extrapolation onto a mesh with a higher resolution, aliasing effects arise. This effect is caused by a lack of information on the smallest wave lengths, which are resolved on the fine grid, but are missing on the coarse mesh. However it has been demonstrated that after a time step of the order of the Kolmogorov time scale the spectra has been automatically adopted and regenerated itself, and has been sufficient smoothed. These numerical studies demonstrated that the numerical schemes and methods implemented in the engine simulation code are suitable for (V)LES type simulations.

¹Strictly speaking, this refers to models based on the Boussinesq approximation only, which represent the majority of commonly applied models

The two-scale hybrid RANS-LES model has been applied to the simulation of two distinct model engines. The first engine represents a rapid compression machine (RCM) with a square piston geometry, and the second is a model four valve SI engine with a flat piston design. For the RCM detailed measurements of the flow field are available. The results of the two scale model agree well with the measurements and show a significant improvement in comparison to the standard RANS approach. The results of multi-cycle simulations of the 4-valve SI engine demonstrated the capability of the two scale model to capture the effects of cycle-to-cycle variation, even though a low resolution mesh has been employed in the calculations.

Finally the two-scale model has been coupled to the G -equation model for simulation the ignition and combustion process in a cylindrical constant volume vessel. The feasibility of the concept has been successfully demonstrated. The numerical methods implemented in the level set solver have been too diffusive to yield physically sound results as the turbulence–flame interaction, i.e. flame wrinkling and convolution, needs to be improved.

However the influence of the turbulent initialisation on the flame propagation and flame deformation has been successfully demonstrated. Employing aggressive mesh refinement around the flame front, and thus reducing the influence of the low order schemes of the level set solver by minimising the discretisation error, visualises the potential of the combined VLES/ G -equation approach in the context of premixed combustion modelling.

Bibliography

- [1] Advisory Group for Aerospace Research and Development. AGARD test cases for the validation of large-eddy simulations of turbulent flows. AGARD Advisory Report 345, April 1998.
- [2] H. I. Andersson. Introduction to turbulence modelling. Lecture notes, Division of Applied Mechanics, Department of Physics and Mathematics, Norwegian Institute of Technology, Trondheim, October 1988.
- [3] R. Arlitt. *Analysis of Weakly Compressible Turbulence Using Symmetry Methods and Direct Numerical Simulation*. PhD thesis, Instiut für Technische Mechanik, RWTH Aachen, 2005.
- [4] C. Bailly and D. Juve.
- [5] C. Bailly, P. Lafon, and S. M. Candel.
- [6] J. Bardina, J. H. Ferziger, and W. C. Reynolds. Improved subgrid-scale models for large-eddy simulation. *AIAA Paper*, 80:1357, 1980.
- [7] P. Batten, U. Goldberg, and S. Chakravarthy. LNS – an approach towards embedded LES. *AIAA Paper 2002-0427*, 2002.
- [8] P. Batten, U. Goldberg, and S. Chakravarthy. Interfacing statistical turbulence closures with large-eddy simulation. *AIAA Journal*, 42(3):485–492, 2004.
- [9] W. Bechara, C. Bailly, P. Lafon, and S. M. Candel.
- [10] M. Billson. *Computational Techniques for Turbulence Generated Noise*. PhD thesis, Chalmers University of Technology, Göteborg, 1998.
- [11] M. Boger. *Modelisation de sous-maille pour la simulation aux grandesechelles de la combustion turbulente premelangee*. PhD thesis, Ecole Centrale Paris, France, 2000.
- [12] H. Boughanem. *Évaluation des termes de transport et de dissipation de surface de flamme par simulation numérique directe de la combustion turbulente*. PhD thesis, Université de Rouen, Institute Français du Petrole, 1998.
- [13] J. Boussinesq. Essai sur la théorie des eaux courantes. *Mem. Acad. Sci. Inst. Fr*, 23(1):252–260, 1877.

-
- [14] K. Bray, P. Libby, and J.B.Moss. Flamelet crossing frequencies and mean reaction rates in premixed combustion. *Comb. Sci. Tech.*, 41:143–172, 1984.
- [15] M. Breuer. *Direkte Numerische Simulation und Large-Eddy Simulation turbulenter Strömungen auf Hochleistungsrechnern*. Habilitationsschrift, Friedrich-Alexander-Universität Erlangen-Nürnberg, 2001.
- [16] C. Canuto, M. Hussaini, A. Quarteroni, and T. Zang. *Spectral Methods in Fluid Mechanics*, 1987.
- [17] V. Chakravarthy and S. Menon. Large-eddy simulation of turbulent premixed flames in the flamelet regime. *Combust. Sci. Technol.*, 162:175–222, 2001.
- [18] F. Charlette, C. Meneveau, and D. Veynante. A power-law flame wrinkling model for LES of premixed turbulent combustion. Part II: Dynamic formulation. *Combustion and Flame*, 131(1-2):181–197, 2002.
- [19] J.-P. Chollet and M. Lesieur. Parameterization of small scales of three-dimensional isotropic turbulence utilizing spectral closures. *Journal of the Atmospheric Sciences*, 38(12):2747–2757, December 1981.
- [20] F. K. Chow and P. Moin. A further study of numerical errors in large-eddy simulations. *Journal of Computational Physics*, 184(2):366/380, 2003.
- [21] P. Clavin. Dynamic behaviour of premixed flame fronts in laminar and turbulent. *Prog. Energ. Comb. Sci.*, 11:1–59, 1985.
- [22] O. Colin, F. Ducros, D. Veynante, and T. Poinso. A thickened flame model for large eddy simulations of turbulent premixed combustion. *Physics of Fluids*, 12(7):1843–1863, 2000.
- [23] T. Craft, B. Launder, and K. Suga. Prediction of turbulent transitional phenomena with a nonlinear eddy-viscosity model. *International Journal of Heat and Fluid Flow*, 18(1):15–28, 1997.
- [24] R. Dahms. private communication. Institute for Combustion Technology, RWTH Aachen, 2008.
- [25] L. Davidson. Hybrid LES-RANS: Inlet boundary conditions. In B. Skallerud and H. Andersson, editors, *3rd National Conference on Computational Mechanics – MekIT '05*, pages 7–22, Trondheim, Norway, 11-12 May 2005.
- [26] L. Davidson and M. Billson. Hybrid LES-RANS using synthesized turbulent fluctuations for forcing in the interface region. *International Journal of Heat and Fluid Flow*, 27(6):1028–1042, 2006.

- [27] L. Davidson and S. Dahlström. Hybrid LES-RANS: An approach to make LES applicable at high Reynolds number. *International Journal of Computational Fluid Dynamics*, 19(6):415–427, 2005.
- [28] L. Davidson and S. Dahlström. *Hybrid LES-RANS: Computation of the Flow Around a Three-Dimensional Hill*, pages 319–328. Number 6 in Engineering Turbulence Modelling and Measurements. Elsevier, 2005.
- [29] F. Ducros, P. Comte, and M. Lesieur. Large-eddy simulation of transition to turbulence in a boundary layer developing spatially over a flat plate. *Journal of Fluid Mechanics*, 326:1–36, 1996.
- [30] P. Durbin. A Reynolds stress model for near-wall turbulence. *Journal of Fluid Mechanics*, 249:465–498, 1993.
- [31] S. El Tahry. k - ϵ -equation for compressible reciprocating engine flows. *AIAA Journal of Energy*, 7(4):345–353, 1983.
- [32] J. Ewald. *A Level Set Based Flamelet Model for the Prediction of Combustion in Homogenous Charge and Direct Injection Spark Ignition Engine*. PhD thesis, Institut für Technische Verbrennung, RWTH Aachen, 2006.
- [33] A. Favre. Statistical equations of turbulent gases. *Problems of Hydrodynamics and Continuum Mechanics*, pages 231–266, 1969.
- [34] J. Ferziger and M. Perić. *Computational Methods for Fluid Dynamics*. Springer, 2nd edition edition, 1999.
- [35] F. Freikamp and D. Haworth. *GMTEC/ACFLUX Developers Manual*. Advanced Combustion GmbH, Aachen.
- [36] W. Gardiner. *Combustion Chemistry*. Springer Verlag, 1984.
- [37] M. Germano, U. Piomelli, P. Moin, and W. Cabot. A dynamic subgrid-scale eddy viscosity model. *Phys. Fluids*, 29:2323–2324, 1991.
- [38] B. J. Geurts. Inverse modeling for large-eddy simulation. *Physics of Fluids*, 9:3585–3587, 1997.
- [39] B. J. Geurts. *Elements of direct and large-eddy simulation*. Edwards, 2004.
- [40] S. Ghosal and P. Moin. The Basic Equations for the Large Eddy Simulation of Turbulent Flows in Complex Geometry. *Journal of Computational Physics*, 118(1):24–37, 1995.

-
- [41] Y. Hamamoto, M. Izumi, and E. Tomita. The effect of swirl on the combustion of a homogeneous mixture in a closed vessel, 1st report, swirl and its turbulence characteristics in a combustion chamber (*in Japanese*). *Proc. of JSME*, 53(488):1395–1402, 1986.
- [42] Y. Hamamoto, M. Izumi, and E. Tomita. The effect of swirl on the combustion of a homogeneous mixture in a closed vessel, 2nd report, burning velocity and burning zone thickness of turbulent flames (*in Japanese*). *Proc. of JSME*, 53(489):1627–1634, 1986.
- [43] Y. Hamamoto, M. Izumi, and E. Tomita. The effect of swirl on the combustion of a homogeneous mixture in a closed vessel. *JSME International Journal Series II*, 31(1):140–149, 1988.
- [44] Y. Hamamoto, M. Izumi, and E. Tomita. Turbulent premixed flames in a closed vessel studied through analysis of flame photographs. *JSME International Journal Series II*, 32(3):443–448, 1989.
- [45] Y. Hamamoto, M. Izumi, and E. Tomita. Effects of swirl and air-fuel ratio on premixed combustion in a closed vessel. *JSME International Journal Series II*, 33(2):370–376, 1990.
- [46] K. Hanjalic, M. Hadziabdic, L. Temmerman, and M. Leschziner. Merging les and rans strategies: Zonal or seamless coupling? In *Direct and Large-Eddy Simulation*, volume 5 of *ERCOTAC Series*., pages 451–464, 2005.
- [47] M. Herrmann. *Numerical Simulation of Premixed Turbulent Combustion Based on a Level Set Flamelet Model*. Dissertation, RWTH Aachen University, 2001.
- [48] M. Herrmann. Refined level set grid method for tracking interfaces. Annual Research Briefs. *Center for Turbulence Research, Stanford Univ./NASA Ames, Stanford, California*, pages 3–14, 2005.
- [49] R. I. Issa. Solution of the implicitly discretised fluid flow equations by operator splitting. *J. Comput. Phys.*, 62:40–65, 1986.
- [50] N. Kawahara, E. Tomita, S. Yoshiyama, A. Nishiyama, and Y. Hamamoto. Effects of swirl turbulent flow field and inhomogeneous concentration field on combustion of fuel-air mixture in a constant volume vessel. *5th Intl. Symp. COMODIA 2001*, pages 219–225, 2001.
- [51] A. Kempf, M. Klein, and J. Jannicka. Efficient generation of initial- and inflow-conditions for transient turbulent flows in arbitrary geometries. *Flow, Turbulence and Combustion*, 74(1):67–84, 2005.

-
- [52] W. Kim and S. Menon. Numerical modeling of turbulent premixed flames in the thin-reaction-zones regime. *Combust. Sci. Technol.*, 160:119–150, 2000.
- [53] M. Klein, A. Sadiki, and J. Janicka. A digital filter based generation of inflow data for spatially developing direct numerical or large eddy simulations. *Journal of Computational Physics*, 186(2):652–665, 2003.
- [54] A. Kolmogorov. Dissipation of energy in the locally isotropic turbulence. *Comptes Rendus (Doklady) de l'Académie des Sciences de l'URSS*, XXXII(1):16–18, 1941.
- [55] A. Kolmogorov. The local structure of isotropic turbulence in an incompressible viscous fluid. *Dokl. Akad. Nauk. SSSR*, 30:301–305, 1941.
- [56] A. Kolmogorov. Equations of turbulent motion in an incompressible fluid. *Izvestia Academy of Science, USSR; Physics*, 6(1-2):56–58, 1942.
- [57] R. Kraichnan. Diffusion by a random velocity field. *J. Comp. Physics*, 13(1):22–31, 1970.
- [58] B. E. Launder and D. B. Spalding. *Mathematical models of Turbulence*. Academic Press, London, 1972.
- [59] B. E. Launder and D. B. Spalding. The numerical computation of turbulent flows. *Computer Methods in Applied Mechanics and Engineering*, 3:269–289, 1974.
- [60] S. Lee, S. Lele, and P. Moin. Simulation fo spatially evolving compressible turbulence and application of taylor hyposis. *Physics of Fluids A*, 4:1521–1530, 1992.
- [61] A. Leonard. Energy cascade in large eddy simulations of turbulent fluid flows. *Adv. in Geophys.*, A 18:237–248, 1974.
- [62] M. Lesieur. *Turbulence in fluids*. Kluwer, 2000.
- [63] M. Lesieur and O. Métails. New trends in large-eddy simulations of turbulence. *Annu. Rev. Fluid. Mech.*, 28:45–82, 1996.
- [64] B. Lewerich. Implementierung eines nichtlinearen $k-\varepsilon$ turbulenzmodelles in gmetec. Master's thesis, Institut für Technische Mechanik, RWTH Aachen, 2004.
- [65] D. Lilly. The representation of small-scale turbulence in numerical simulations. In H. H. Goldstine, editor, *Proc. of the IBM Scientific Computing Symposium on Environmental Sciences*, IBM Forum No. 320–1951, pages 195–210, 1967.
- [66] E. Lorenz. Deterministic non-perodic flow. *J. Atmos. Sci.*, 20:130–141, 1963.

-
- [67] S. Lück, C. Renner, J. Peinke, and R. Friedrich. The Markov-Einstein coherence length - a new meaning for the Taylor length in turbulence. *Phys. Lett. A*, 359:335–339, 2006.
- [68] T. Lund, X. Wu, and D. Squires. Generation of turbulent inflow data for spatially-developing boundary layer simulations. *J. Comp. Physics*, 140:233–256, 1998.
- [69] J. Magnien. *Simulation des grandes échelles (SGE) d'écoulements de fluides quasi incompressibles*. PhD thesis, Université de Paris 11, Orsay, 2001.
- [70] F. Marble and J. Broadwell. The Coherent Flame Model for Turbulent Chemical Reactions. Technical report, DTIC Research Report ADA036768, 1977.
- [71] D. Marc, J. Borée, R. Bazile, and G. Charnay. PIV and LDV measurements of tumbling vortex flow in a model square section motored engine. *SAE 972834*, 1997.
- [72] M. Matalon and B. Matkovsky. Flames at gasdynamic discontinuities. *Journal of Fluid Mechanics*, 124:239–259, 1982.
- [73] S. Maurel, J. Borée, and R. Bazile. Experimental database on a compresse vortex. Technical report, Groupe Ecoulement et Combustion, Institut de Mécanique des Fluides de Toulouse, 2001.
- [74] S. Menon. Subgrid combustion modeling for LES of single and two-phase reacting flows. In R. Friedrich and W. Rodi, editors, *Advances in LES of Complex Flows*, Proceedings of the Euromech Colloquium 412, 2000.
- [75] S. Menon and W.-W. Kim. High reynolds number flow simulations using the localized dynamic subgrid-scale model. *AIAA-1996-425*, 34th Aerospace Sciences Meeting and Exhibit, Reno/NV, 1996.
- [76] F. Menter. Zonal two-equation k - ω turbulence models for aerodynamic flows. *AIAA Paper 1993-2906*, 1993.
- [77] F. R. Menter. Two-equation eddy-viscosity turbulence models for engineering applications. *AIAA Journal*, 32(8):1598–1605, August 1994.
- [78] P. Moin, K. Squires, W. Cabot, and S. Lee. A dynamic subgrid-scale model for compressible turbulence and scalar transport. *Physics of Fluids A: Fluid Dynamics*, 3:2746, 1991.
- [79] V. Moureau, I. Barton, C. Angelberger, and T. Poinot. Towards Large Eddy Simulation in Internal-Combustion Engines: simulation of a compressed tumble flow. *SAE transactions*, 113(3):1315–1324, 2004.

-
- [80] M. Oberlack, H. Wenzel, and N. Peters. On symmetries, invariant solutions and averaging of the G -equation for premixed combustion. *Comb. Theory Modelling*, 5(4):1–20, 2001.
- [81] S. V. Patankar. *Numerical Heat Transfer and Fluid Flow*. McGraw Hill, 1980.
- [82] N. Peters. Numerical and asymptotic analysis of systematically reduced reaction schemes for hydrocarbon flames. In R. Glowinski, B. Larrouturou, and R. Temam, editors, *Numerical Simulation of Combustion Phenomena, Lecture Notes in Physics*, volume 241, pages 90–109. Springer Verlag, 1985.
- [83] N. Peters. *Fifteen Lectures on Laminar and Turbulent Combustion*. Ercoftac Summer School, September 14–28 1992. Institut für Technische Mechanik, RWTH Aachen, 1992.
- [84] N. Peters. The turbulent burning velocity for large scale and small scale turbulence. *J. Fluid Mech.*, 384:107–132, 1999.
- [85] N. Peters. *Turbulent Combustion*. Cambridge University Press, 2000.
- [86] N. Peters. Technische Verbrennung. Lecture notes, 2005.
- [87] N. Peters and F. Williams. The asymptotic structure of stoichiometric methane-air flames. *Combustion and Flame*, 68:185–207, 1987.
- [88] H. Pitsch. A G -equation formulation for large-eddy simulation of premixed turbulent combustion. In *CTR Annual Research Briefs*, pages 3–14. Stanford University, 2002.
- [89] H. Pitsch. A consistent level set formulation for large-eddy simulation of premixed turbulent combustion. *Combustion and Flame*, 143(4):587–598, 2005.
- [90] H. Pitsch. Large-eddy simulation of turbulent combustion. *Ann. Rev. Fluid Mech.*, (38):453–483, 2006.
- [91] H. Pitsch and L. D. de Lageneste. Large-eddy simulation of premixed turbulent combustion using a level-set approach. *Proc. Combust. Inst.*, 29:2001–8, 2002.
- [92] T. Poinsot and D. Veynante. *Theoretical and Numerical Combustion*. Edwards, 2001.
- [93] S. Pope. A more general effective-viscosity hypothesis. *Journal of Fluid Mechanics*, 72(02):331–340, 1975.
- [94] S. B. Pope. *Turbulent Flows*. Cambridge University Press, 2000.
- [95] L. Prandtl. Über die ausgebildete Turbulenz. *ZAMM*, 5:136–139, 1925.

-
- [96] L. Prandtl. Über ein neues Formelsystem für die ausgebildete Turbulenz. *Nach. Akad. Wiss. Göttingen, Math-Phys. Kl.*, pages 6–19, 1945.
- [97] O. Reynolds. III. An experimental investigation of the circumstance which determine whether the motion of water shall be direct or sinuous, and of the law of resistance in parallel channels. *Phil. Trans. R. Soc. London*, 174:935, 1883.
- [98] O. Reynolds. IV. On the dynamical theory of the incompressible viscous fluids and the determination of the criterion. *Phil. Trans. R. Soc. London*, 186:123–164, 1895.
- [99] S. Richard. *Simulation aux grande échelle de la combustion dans les moteurs à allumage commandé*. PhD thesis, Institut Français du Pétrole, 2005.
- [100] L. Richardson. Weather Prediction by Numerical Process. *Proc. Roy. Soc. (London) A1*, 10:709, 1922.
- [101] J. Rotta. Über eine Methode zur Berechnung turbulenter Scherströmungen. *Aerodynamische Versuchsanstalt*, Rep. 69 A 14, 1968.
- [102] J. C. Rotta. Statistische Theorie nichthomogener Turbulenz. *Zeitschrift für Physik*, 129:547–572, 1951.
- [103] J. C. Rotta. *Turbulente Strömungen*. Teubner, 1972.
- [104] S. Saddoughi and S. Veeravalli. Local isotropy in turbulent boundary layers at high Reynolds numbers. *Journal of Fluid Mechanics*, 268(333-372), 1994.
- [105] P. Sagaut. *Large Eddy Simulation for Incompressible Flows - An introduction*. Springer, 2005.
- [106] L.-U. Schrader. private communication. Institut für Technische Verbrennung, 2005.
- [107] L.-U. Schrader. Validation of a two-scale vles turbulence model employing artificially generated initial and boundary condition. Master's thesis, Institut für Technische Mechanik, RWTH Aachen, 2004.
- [108] U. Schumann. Subgrid scale model for finite difference simulations of turbulent flows in plane channels and annuli. *Journal of Computational Physics*, 18:376–404, Aug. 1975.
- [109] J. Sethian. *Level Set Methods: Evolving Interfaces in Geometry, Fluid Mechanics, Computer Vision, and Materials Science*. Cambridge University Press Cambridge, MA, 1996.

-
- [110] R. Skoda. *Numerische Simulation abgelöster und transitionaler Strömungen in Turbomaschinen*. VDI-Verlag, 2003.
- [111] J. Smagorinsky. General circulation experiments with the primitive equations: I. the basic equations. *Mon. Weather. Rev.*, 91(99-164), 1963.
- [112] V. Sohm. private communication. BMW Group, Munich, 2005.
- [113] V. Sohm. *Hybrid RANS/LES Simulation to Predict Cyclic Variations in IC-Engines*. PhD thesis, Institut für Technische Verbrennung, RWTH Aachen, 2007.
- [114] P. Spalart and S. Allmaras. A One-Equation Turbulence Model for Aerodynamic Flows, AIAA Paper 92-0439. *30th AIAA Aerospace Sciences Meeting, Reno, USA*, 1992.
- [115] P. R. Spalart, W.-H. Jou, M. Strelets, and R. Allmaras. Comments on the feasibility of LES for Wings, and on a Hybrid RANS/LES approach. In C. Liu and Z. Liu, editors, *Advances in DNS/LES*, 1st AFOSR Int. Conf. on DNS/LES, Ruston, LA, pages 137–148. Greyden Press, Columbus, OH., 1997.
- [116] D. B. Spalding. Mixing and chemical reaction in steady confined turbulent flames. In *13th Symp. (Int.) on Combustion*, pages 649–657. The Combustion Institute, Pittsburgh, 1971.
- [117] D. B. Spalding. Developmement of the eddy-break-up model of turbulent combustion. In *16th Symp. (Int.) on Combustion*, pages 1657–1663. The Combustion Institute, Pittsburgh, 1976.
- [118] C. G. Speziale. Turbulence modeling for time-dependent rans and vles: A review. *AIAA Journal*, 36(3):173–184, 1996.
- [119] C. G. Speziale. A combined large eddy simulation and time-dependent rans capability of high-speed compressible flows. *Journal of Scientific Computing*, 13(3):253–274, 1998.
- [120] S. Stolz and N. A. Adams. An approximate deconvolution procedure for large-eddy simulation. *Physics of Fluids*, 11(7):1699–1701, July 1999.
- [121] M. Strelets. Detached eddy simulation of massively separated flows. *AIAA Paper 2001-0879*, 2001.
- [122] G. Taylor. The spectrum of turbulence. *Proc. R. Soc. London Ser. A 164*, pages 476–490, 1938.
- [123] H. Tennekes and J. Lumley. *A First Course in Tubulence*. MIT Press, Cambridge, MA, 1972.

-
- [124] H. Versteeg and W. Malalasekera. *An Introduction to Computational Fluid Dynamics: The Finite Volume Method*. Prentice Hall, 1995.
- [125] L. Wang and N. Peters. The length scale distribution function of the distance between extremal points in passive scalar turbulence. *J. Fluid Mech.*, accepted for publication, 2006.
- [126] H. Wenzel. *Direkte numerische Simulation der Ausbreitung einer Flammenfront in einem homogenen Turbulenzfeld*. Dissertation, RWTH Aachen University, 2000.
- [127] D. C. Wilcox. *Turbulence Modeling for CFD*. DCW Industries, 2nd edition edition, 1998.
- [128] W. Willems. *Numerische Simulation turbulenter Scherströmungen mit einem Zwei-Skalen Turbulenzmodell*. PhD thesis, Institut für Technische Mechanik, RWTH Aachen, 1996.
- [129] F. A. Williams. Turbulent combustion. In J. Buckmaster, editor, *The Mathematics of Combustion*, pages 97–131. SIAM, Philadelphia, 1985.
- [130] V. Yakhot and S. A. Orszag. Renormalization group analysis of turbulence i. basic theory. *J. Sci. Comput.*, 1(1):3–51, 1986.
- [131] A. Yoshizawa and K. Horiuti. A statistically-derived subgrid-scale kinetic energy model for the large-eddy simulation of turbulent flows. *Journ. Phys. Soc. Japan*, 54(8):2834–2839, 1985.
- [132] J. B. Zeldowitsch and D. A. Frank-Kamenetzki. A theory of thermal propagation of flame. *Acta Physicochimica URSS*, 9(2):341–350, 1938.

Lebenslauf

Persönliche Daten

| | |
|---------------|-----------------|
| Name | Frank Freikamp |
| Geburtsdatum | 12. August 1973 |
| Geburtsort | Dinslaken |
| Familienstand | verheiratet |
| Nationalität | deutsch |

Schulbildung

| | |
|-----------|---|
| 1980–1984 | Gemeinschaftgrundschule Hagenschule, Dinslaken |
| 1984–1993 | Otto-Hahn-Gymnasium, Dinslaken; Abschluss: Abitur |

Studium

| | |
|-----------------|---|
| 10/1994–05/2000 | Grund- und Hauptstudium Maschinenbau an der RWTH Aachen, Fachrichtung Grundlagen des Maschinenbaus; Abschluss: Diplom |
| 1998–1999 | ERASMUS Stipendiat an der NTNU Trondheim, Norwegen |

Beruflicher Werdegang

| | |
|-----------|--|
| 2000–2006 | Wissenschaftlicher Angestellter am Institut für Technische Verbrennung der RWTH Aachen |
| seit 2006 | Robert Bosch GmbH, Forschung und Voraentwicklung |

